Doctoral Dissertation

A Study of Autonomous Navigation System of Unmanned Surface & Underwater Vehicle

Advisor

Professor Kim, Joon-Young

August, 2019

Graduate School of Ocean Science and Technology

Korea Maritime and Ocean University

Department of Convergence Study on the Ocean Science and Technology

Hong, Sung-Min

We certify that we have read this dissertation and that, in our opinion. It is satisfactory in scope and quality as a dissertation for the degree of doctor of philosophy in Ship and Offshore Plant, submitted by Hong, Sung-Min

DISSERTATION COMMITTEE

Chairperson : Professor Choi, Hyeung-Sik

Department of Mechanical Engineering, Korea Maritime and Ocean University

_____

Supervisor : Professor Kim, Joon-Young

Department of Ocean Advanced Materials Convergence Engineering, Korea Maritime and Ocean University

_____

Reviewer : Professor Sur, Joo no

Department of Mechanical Engineering, Korea Maritime and Ocean University

_____

Reviewer : Professor Lee Sung-Wook

Department of Naval Architecture and Marine Engineering, Korea Maritime and Ocean University

_____

Reviewer : Professor Cho, Yong-Seong

Department of Electronics Engineering, Kyungnam College of Information & Technology

_____

July, 2019

Graduate School of Ocean Science and Technology

Korea Maritime and Ocean University

CONTENTS

List of Tables

List of Figures

A Study of Autonomous Navigation System of Unmanned Surface & Underwater Vehicle

Hong, Sung Min

Department of Convergence Study on the Ocean Science and Technology

Ocean Science and Technology School of Korea Maritime and Ocean University

Abstract

In this study, we developed a combined unmanned ocean vehicle for real-time marine exploration and designed a guidance law and controller for autonomous navigation of the platform. The developed unmanned ocean vehicle is a combination of unmanned surface vehicle, underwater vehicle and underwater cable to overcome disadvantages such as position accumulation error, limit of battery capacity, and inability to secure real-time data of existing unmanned underwater vehicle.

The combined unmanned ocean vehicle, Global Positioning System(GPS) and Ultra Short Base Line(USBL) sensors mounted on unmanned surface vehicle, unmanned underwater vehicle can be used to know the location of current exploration area and power supply for a long time on unmanned submarine using high capacity battery. It is also possible to check the terrain information of the exploration area, the status of unmanned underwater vehicle, and camera information in real-time using underwater cable. However, such combined unmanned ocean vehicle, in which the surface and underwater vehicles are

connected by underwater cables, will encounter disturbances such as current, waves, and other disturbances due to dynamic movement of underwater cables.

In this study, equations are derived for the motion of a combined unmanned ocean vehicle. Simulation was carried out using the developed equations of motion and the motion of the combined unmanned ocean vehicle was confirmed. Movement of the unmanned underwater vehicle was also observed according to disturbance generated in the underwater cable.

In addition, autonomous navigation system required to perform a given task was studied, The unmanned surface vehicle follows a given way-point through the Pure-Pursuit method which is a geometric path-following method. The unmanned underwater vehicle is geometrically defined by the relative position and the relative orientation angle of each platform so that it can maintain a certain distance and direction angle.

Combined unmanned ocean vehicle was designed to take lead-follower control from defined geometric definition. Therefore, anti-windup PID controller and backstepping controller based on disturbance robust Lyapunov function were designed in this study. Dynamics simulation was performed to verify the designed induction law and the performance of the controller.

Finally, to verify the proposed algorithm, we constructed a rubber boat hull and a torpedo type unmanned underwater vehicle and constructed a hardware system for autonomous navigation of the platform. We investigated the performance of a combined unmanned ocean vehicle and controller by performing field tests and performed tests for sensors mounted on the platform.

KEY WORDS : Unmanned Surface Vehicle, Unmanned Underwater Vehicle, Underwater Cable, Leader-Follower Control, Dynamic Simulation, Field Test

1. Introduction

1.1. Background

Among various studies related to marine development, marine exploration is a basic physical exploration that is needed for various purposes such as resource and energy development and management, navigation safety, and military operation. With the development of science and technology along with the necessity, studies using unmanned robot technology in an underwater environment that replaces existing ships or humans are actively being carried out.

Marine exploration is being used directly for engineering purposes such as marine civil engineering and offshore plant installations throughout marine development phases, ranging from the initial exploration stage of resource development to the production of equipment, the change of terrain in the production process, or the change of submarine lipids due to internal fluid reduction[1]. If information of the undersea topography or depth of water is not accurate, it may cause damage such as stranding of ship, damage of underwater optical cable, and damage of offshore structure. In addition, researches and equipment development for a deep tow survey system are being carried out for precise exploration of seabed topography[2].

In Korea, coastal lines are complicated. Coastal fishing nets, farms, and so on

cannot be used for large-scale exploration. Therefore, marine exploration using small vessels is being carried out. However, if the ship is stranded in a fishing net or a farm, it may cause not only human injury, but also environmental pollution. Therefore, it is necessary to develop an unmanned platform capable of operating in a complex and narrow coastal area.

Thus, the objective of this study was to develop a control algorithm for platform operation and develop a combined unmanned ocean vehicle that could improve the accuracy of submarine geomorphological exploration.

1.2. Research Trend

It is difficult to explain all methods and types of equipment because marine geological exploration method and platform use different equipment and methods according to the purpose. Therefore, research trends will be focused on ocean exploration platform related to this study.

In the case of marine geophysical exploration techniques for the purpose of resource development, most of them are operated by large-scale marine probes and marine exploration equipment in the deep sea. In addition, as the depth of exploration water deepens, the accuracy of the acquired information is lowered. To solve this problem, explorations are carried out using underwater human bodies or an unmanned underwater vehicle. Unmanned platforms have been developed to perform ocean surveys on behalf of human beings in accordance with the development of technology. They are being used for various purposes. A combined unmanned ocean vehicle is a platform in which unmanned surface vehicle is combined with unmanned underwater vehicle. Such an unmanned platform can be operated in a small watershed. It can work on behalf of

humans in a dangerous environment. Most platforms listed in Table 1-1 use Remotely Operate Vehicles (ROVs) for the purpose of operation, and marine structure inspection in specific sea areas or ocean exploration using underwater towed platform instead of ship role. The motion of a system in which heterogeneous platforms are interlocked is a multibody dynamics system where a plurality of objects move together. Thus, the behavior of one element can affect, the behavior of other elements. It is difficult to analyze and control the motion of the entire system. Therefore, various studies are being carried out for motion analysis of related systems[3][4].

SEA-KIT provides unmanned and autonomous solutions to the maritime industry to perform a variety of missions. However, SEA-KIT does not have a separate underwater cable between the unmanned surface vehicle and unmanned underwater vehicle, although it follows a given route and transmits information through underwater communication at close range. The amount of information that can be transmitted through the underwater communication is currently limited. Studies are being conducted to solve position error problem of underwater navigation of unmanned underwater vehicle.

Table 1-1 Combined Unmanned Ocean Vehicle

Platform	Specification
 RSV Sea Observer	■ MARINE TECH co. ■ L × W × H [m] : 4.2 × 2.1 × 1.7 ■ Draft [m] : 0.5 ■ Thruster : 2 electric engines ■ Remote Operating Range [m] : 5000(Max) ■ Navigation sensors : Gyrocompass, DGPS, Autopilot, Camera
 AVS 2.5	■ Sea Robotics co. ■ L × W × H [m] : 2.5 × 1 × 0.15 ■ Draft [m] : 0.15 ■ Thruster : 2 BLDC electric thrusters ■ Remote Operating Range [m] : 6200(Max) ■ Navigation sensors : GPS, Compass
 Inspector USV with H300V	■ Inspector USV ■ ECA group ■ L × W [m] : 9 × 2.95 ■ Mass [kg] : 4300kg ■ Thruster : 2 diesel waterjets ■ H300V ■ L × W × H [m] : 0.84 × 0.53 × 0.6 ■ Weight in air : 70kg ■ Thruster : Horizontal(4 vectored thrusters) Vertical(1thruster)

CAT-Surveyor

- Subsea Tech
- L × W [m] : 3 × 1.6
- Weight in air : 270kg
- Max. speed : 5knots
- Thrusters :
  2 outboard brushless electrical motors
- Batteries : 2 Li-ion (12h autonomy)

HERON

- CleartPath ROBOTICS
- L × W [m] : 1.35 × 0.98
- Communication : Wireless 2.4GHz
- Weight [kg] : 28
- Navigation sensors : GPS, IMU, Lidar

Spartan

Halcyon

CUSV

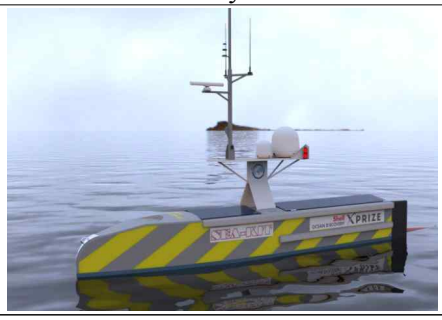

SEA-KIT

1.3. Objective of Research

Marine exploration using existing research and development equipment described in Section 1.2 has the same limitations as shown in Table 1-2.

Table 1-2 Limitations of marine exploration equipment

Ship	■ A lot of operation cost ■ Error of terrain information due to water depth, ■ Difficulty in exploration at the coast or port.
Towed platform	■ Difference in motion depending on the speed of the mother ship ■ Difficult to grasp the location of the area to be explored accurately
USV	■ Errors in terrain information due to water depth
ROV	■ Mother Ship is needed ■ Narrow range of search
AUV	■ Difficult to transmit real time information ■ Navigation Error ■ Battery Limit

Therefore, this study intends to develop a new type of combined unmanned ocean vehicle and an autonomous navigation system to overcome limitations of previously developed marine exploration equipment.

The combined unmanned ocean vehicle to be introduced in this paper can transmit real-time underwater exploration information. It uses USBL of unmanned surface vehicle to reduce accumulated error of the position of existing unmanned underwater vehicle. Previously, there was no separate propeller for an

underwater towed platform. However, in this study, the propeller was installed to increase the degree of freedom (DOF). In addition, the unmanned underwater vehicle can control water depth by using winch included in the launch and recovery system, thereby reducing error of the topographical information according to water depth. In addition, a leader-follower control is applied to the autonomous navigation of the developed combined unmanned ocean vehicle. Leader-Follower control includes a guidance law's and a controller to follow the way-point of the unmanned surface vehicle and unmanned underwater vehicle.

Before performance evaluation of the platform and control system, dynamics modeling was carried out. Influence of the underwater cable on the unmanned underwater vehicle was analyzed and the validity of the applied control algorithm was verified. Finally, we verified the performance of the platform motion and control algorithm developed through real field experiments.

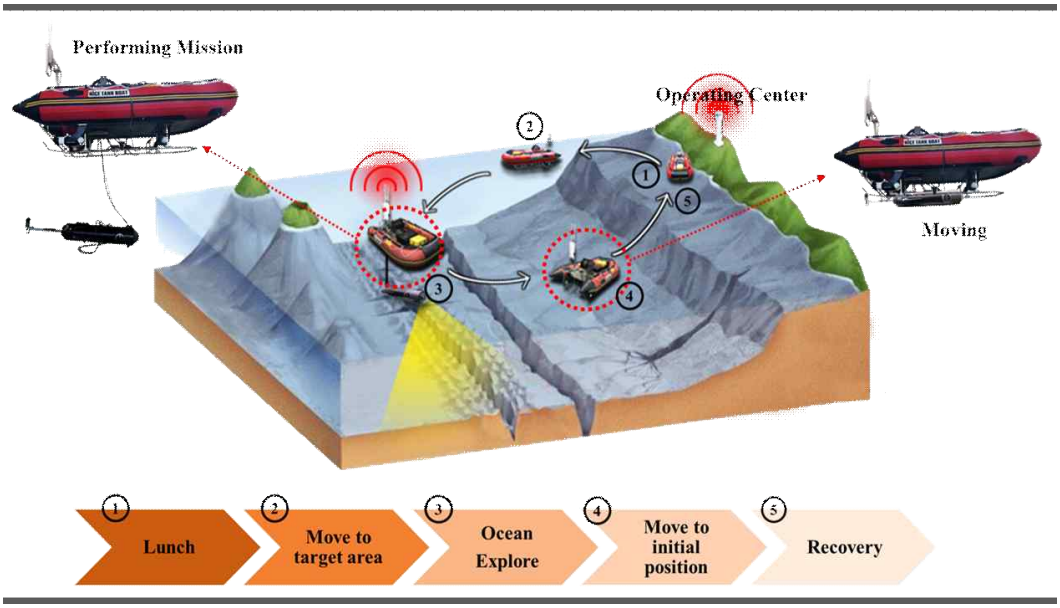

Fig. 1-1 Operational concept of combined unmanned ocean vehicle

1.4. Organization of the thesis

This paper is organized as follows.

CHAPTER 2. MODELING OF DYNAMICS OF COMBINED UNMANNED OCEAN VEHICLE

The combined unmanned ocean vehicle developed in this study is composed of unmanned surface vehicles, unmanned underwater vehicles, and underwater cable. Equations of motion for each component are derived and disturbance due to wind and tidal loads acting on the platform is explained in this chapter.

CHAPTER 3. DESIGN OF GUIDANCE AND CONTROL LAW

Guidance and control law for performing Leader-Follower control and for tracking a waypoint of a combined unmanned ocean vehicle will be described in this chapter.

CHAPTER 4. DYNAMIC SIMULATION

We verified the validity of induced equations of motion and induction/control algorithms through various simulations in this chapter.

CHAPTER 5. CONFIGURATION OF HARDWARE SYSTEM

Hardware configuration, control system, and operating system of the combined unmanned ocean vehicle developed in this study are described in this chapter.

CHAPTER 6. SENSOR PERFORMANCE AND FIELD TEST OF COMBINED UNMANNED OCEAN VEHICLE

The validity of the basic performance verification experiment and that of the proposed induction/control law of the sensor mounted on the combined unmanned ocean vehicle are verified through actual field tests and results are described in this chapter.

CHAPTER 7. CONCLUSION

Main results and future plans of this study are described in this chapter.

APPENDIX

Characteristics of system matrices used in this study and important theories mentioned in the paper are summarized.

2. Modeling of Dynamics of Combined Unmanned Ocean Vehicle

It is necessary to derive kinetic equations to understand the dynamic behavior of the platform to be developed before the actual sea area test. It is also important to confirm the performance of the controller and the path following algorithm to be designed later. In this chapter, the combined unmanned ocean vehicle is divided into an unmanned surface vehicle, an unmanned underwater vehicle, and an underwater cable. Motion equations are derived for each platform. Finally, we describe equations of motion considering motion correlation between each platform.

The force and moment acting on the speed, position, attitude, and platform of the unmanned surface vehicle (USV) and the unmanned underwater vehicle (UUV) are defined as shown in Table 2-1 below. USV performing the role of the leader and UUV were used to derive equations of motion.

Table 2-1 The notaion of SNAME for USV&UUV

Degree of Freedom		**Force & Moments**	**Linear & Angular Velocities**	**Positions & Euler Angles**
Translational motion	Surge	X	u	x
	Sway	Y	v	y
	Heave	Z	w	z
Rotational motion	Roll	K	p	ϕ
	Pitch	M	q	θ
	Yaw	N	r	ψ

2.1 Dynamic Modeling of Unmanned Surface Vehicle

2.1.1 Preliminary Modeling of Unmanned Surface Vehicle

Many studies have derived equations of motion of unmanned surface vehicles (USVs). For example, Fossen has conducted a study on ship motion and developed a "maneuvering" model that depicts a 6-DOF nonlinear model and a ship's motion on a horizontal plane. The motion model of the ship described by Fossen is based on a combination of physical principles and empirical observations. It can be classified into longitudinal velocity (Surge) and steering (Yaw) models [5][6][7].

Abkowitz 's model is developed by combining third-order Taylor series expansion of hydrodynamic forces and moments for linear motion with rigid plane equations. Abkowitz also used several simplification assumptions to limit the number of model parameters[5] :

- Includes only primary acceleration port.
- The ship is symmetrical.
- Ignore combined velocity and acceleration.

Norrbin's model derived a planar rigid body equation with empirical representations of hydrodynamic forces and moments based on traction tank experiments. It included modeling of rudder angles as well as propulsion modeling not found in Abkowitz's model. Blanke simplified Norrbin’s model to

explain equations of motion. Nomoto's ship steering model was developed for Displacement Vessels (Fn < 0.4). However, it could also be applied to semi-displacement Vessel (0.4 ~ 0.5 < Fn < 1.0 ~ 1.2) and Planing Vessel (Fn > 1.0 ~ 1.2) [5].

In this paper, a kinetic model is developed based on Fossen's notation and kinetic equations. In addition, hydrodynamics force coefficient used in the dynamics model was used for the USV with specifications similar to those of USV developed in previous studies [5][8].

2.1.2 Dynamics of Unmanned Surface Vehicle(USV)

The USV developed in this study was a commercial rubber boat equipped with two thrusters on the stern section to enable straightening and turning motion. A detailed description of the USV hardware is provided in Chapter 5. Fig 2-1 shows target USV and Table 2-2 shows specifications.

Fig. 2-1 Unmanned Surface Vehicle (USV)

Table 2-2 Specification of USV

Parameter	Value
Length (m)	3
Beam (m)	1.82
Length between perpendiculars (m)	2.5
Weight (kg)	200

Earth-fixed coordinate system and body-fixed coordinate system as reference coordinate systems are defined as shown in Fig. 2-2 to derive horizontal (X-Y) motion equation of the USV. In the fixed coordinate system of the ship, the direction of the yaw line is positive and the starboard direction is the positive y-axis. Right-hand rule is used to determine the z-axis direction.

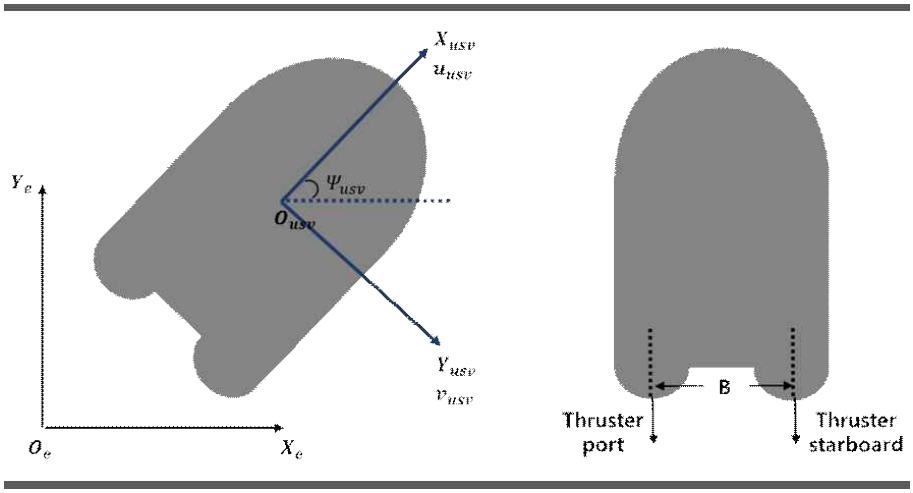

Fig 2-2 Coordinate System of USV

Linear velocity and angular velocity $\nu_l = [u_l, v_l, r_l]^T$ of the USV expressed in the body-fixed coordinate system can be represented by the position, and attitude vector $\eta_l = [x_l, y_l, \psi_l]^T$ in the earth fixed coordinate system through kinematics. It can be with the following equation (2.1).

$$\dot{x}_l = u_l \cos\psi_l - v_l \sin\psi_l \tag{2.1}$$

$$\dot{y}_l = u_l \sin\psi_l + v_l \cos\psi_l$$

$$\dot{\psi}_l = r_l$$

Assuming that USV has neutral buoyancy and the origin of the hull fixed coordinate system is located at the center of mass, the equation of motion in the body-fixed coordinate system can be expressed with the following equation (2.2).

$$M_l \dot{\nu}_l + C_l(\nu_l)\nu_l + D_l(\nu_l)\nu_l = \tau_l \tag{2.2}$$

In equation (2.2), M_l is the inertia matrix of the USV, including the added mass, $C_l(\nu_l)$ is the matrix containing components of Coriolis force and Centrifugal force, and $D_l(\nu_l)$ is the damping matrix. The right side shows force and moment caused by an external force such as wind load and current load or thrust force.

Assuming that the inertia matrix is a constant and that the diagonal matrix and the damping matrix element can ignore the first order higher-order term, the

equation of motion can be simplified, as shown in Equation 2.3 below.

$$
\begin{aligned}
&m_{11}\dot{u}_l - m_{22}v_l r_l + d_{11}u_l = X_l \\
&m_{22}\dot{v}_l + m_{11}u_l r_l + d_{22}u_l = Y_l \\
&m_{33}\dot{r}_l + (m_{22} - m_{11})u_l v_l + d_{33}r_l = N_l
\end{aligned}
\tag{2.3}
$$

2.1.2.1 Control force and moment by thrusters of USV

Thrusters used in this study are thrusters of MINN KOTA, not omnidirectional propeller. As shown in Fig. 1-4, the control force and the control moment can be defined by the following equation (2.4) considering the arrangement of the thrust.

$$
\begin{bmatrix} X_{thrust} \\ 0 \\ N_{thrust} \end{bmatrix} = \begin{bmatrix} T_{port} + T_{stbd} \\ 0 \\ (T_{port} - T_{stbd})B/2 \end{bmatrix}
\tag{2.4}
$$

In order to apply thrust of actual thrusters to the simulation, forward and reverse thrust tests of thrusters mounted on the USV were performed. Thrust test was carried out at the Marine Robotics Center of the R & D Institute. As, shown in Fig. 2-3 below, a tension meter was mounted on the head and the stern on the USV. At this time, the input value was changed by changing digital signal of 12-bit resolution to the analog value which was the control signal and by changing the value to be applied to the propeller from 0.05 to 4.68V.

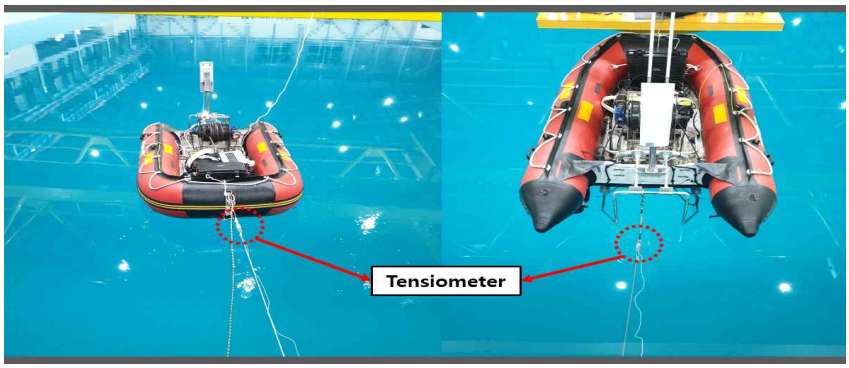

Fig. 2-3 Measurement force of USV thruster

Fig 2-4 shows results of the thrust measurement experiment. The dead zone of the propeller was about 1.6 ~ 3.2V. The thrust force is nonlinear but can be used by linearizing the relationship between thrust force and input voltage. The maximum forward thrust was 29.12kgf, and the maximum reverse thrust was ⁻ 13.83kgf.

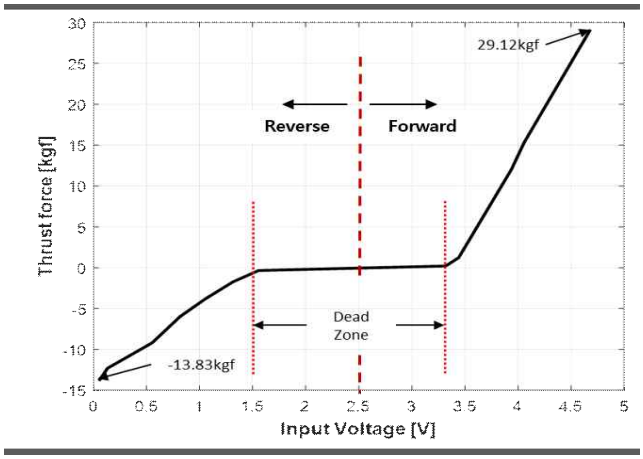

Fig 2-4 Curve of Thrust force

The relationship between input voltage and thrust can be expressed by the

following equation (2.5).

$$T_l = -0.4968 \times V^5 + 5.7702 \times V^4 - 21.755 \times V^3 + 29.0135 \times V^2 - 3.3987 \times V - 13.081 \quad (2.5)$$

2.1.2.2 Ocean Environment - Wind Model

Disturbances acting on a USV include wave load, current load, and wind load. Such disturbances can cause drift motion of the USV. These disturbances need to be taken into consideration to more accurately describe motion. In this study, drift force due to the wave load in the same sea condition was not considered considering that influences of wind and current load were dominant.

First, the force and moment due to wind load can be obtained by using the relative velocity and the relative angle of the wind force for the USV. The relative velocity of the wind acting on the unmanned watercourse can be summarized with equation (2.6).

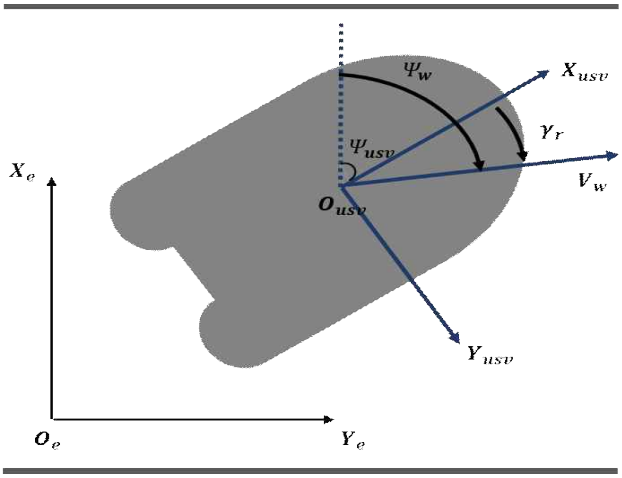

Fig. 2-5 Definition of wind speed and direction

$$
\begin{aligned}
V_R &= \sqrt{u_R^2 + v_R^2} \\
\gamma_R &= \tan^{-1}(v_R/u_R) \\
u_R &= V_w \cos(\gamma_R) - u_l \\
v_R &= V_w \sin(\gamma_R) - v_l
\end{aligned}
\tag{2.6}
$$

In equation (2.6), $(u_R\ ,\ v_R)$ represents relative velocity of the wind with respect to X and Y-axis directions, V_R represents total velocity of the relative velocity, and ψ_R represents angle of relative velocity of the wind. This can be used to calculate the force and moment due to wind loads on each axis. In this study, the magnitude of the force and moment acting on the unmanned watercraft was calculated using the Fossen wind load model. The following equation (2.7) shows force and moment due to wind load.

$$
\begin{aligned}
X_{wind} &= \frac{1}{2} C_X(\gamma_R) \rho_w V_R^2 A_T \\
Y_{wind} &= \frac{1}{2} C_Y(\gamma_R) \rho_w V_R^2 A_L \\
N_{wind} &= \frac{1}{2} C_N(\gamma_R) \rho_w V_R^2 A_L L
\end{aligned}
\tag{2.7}
$$

Where C_X , C_Y , and C_N are wind load coefficients, and ρ_w is air density. A_T , A_L and L refer to the frontal projected area, the lateral projected area, and the horizontal length from the front end of the USV to the end of the aft end, respectively.

In general, the wind load factor is measured by a wind tunnel test. In this study, wind load test was not performed. Wind load factor approximation is

used by referring to results of Fossen's research.

$$C_X(\psi_R) = -c_x \cos(\psi_R) \tag{2.8}$$

$$C_Y(\psi_R) = c_y \sin(\psi_R)$$

$$C_N(\psi_R) = c_z \sin(2\psi_R)$$

$$c_x \in (0.5, 0.9)\ ,\ c_y \in (0.7, 0.95)\ ,\ c_z \in (0.05, 0.2) \tag{2.9}$$

Frontal projected area, lateral projected area, and hull length included in Eq. (2.7) are calculated by measuring the actual system. Their values are shown in the Table 2-3.

Table 2-3 Parameters for wind load calculation

Parameter	Value
$L_{OA}\ (m)$	3
$L_{PP}\ (m)$	2.5
$A_T\ (m^2)$	0.87
$A_L\ (m^2)$	1.44

In this study, wind intensity required to calculate wind load was determined using the following Table 2-4. Table 2-4 summarizes the range of wind speed according to Beaufort number and the value of sea state corresponding to each case based on the sea state table of the Pierson-Moskowitz spectrum.

Table 2-4 Beaufort number and corresponding wind speed

Beaufort Number	Description	Wind Speed	Representative value	Sea State
0	Calm	0 ~ 0.3	0.0	0
1	Light air	0.3 ~ 1.6	0.9	0
2	Light breeze	1.6 ~ 3.4	2.5	1
3	Gentle breeze	3.4 ~ 5.4	4.4	2
4	Moderate breeze	5.5 ~ 7.9	6.7	3
5	Fresh breeze	8.0 ~ 10.0	9.0	4
6	String breeze	10.8 ~ 13.8	12.3	5
7	Moderate gale	13.9 ~ 17.1	15.50	6
8	Fresh gale	17.2 ~ 20.7	18.95	7
9	Strong gale	20.8 ~ 24.4	22.60	7
10	Storm	24.5 ~ 28.4	26.45	8
11	Viloent storm	28.5 ~ 32.6	30.55	90

2.1.2.3 Ocean Environment – Ocean Current Model

Due to a variety of factors such as wind, wave or ocean temperature difference, tidal currents, and so on, very sophisticated forms of algae can occur in irregular shapes, complicating the model's precision mathematically to account for effects of current. Therefore, it is common to model current in marine environment using the first Gauss-Markov process [5].

In this study, current was considered as an irrotational fluid in the X-Y plane. In general, the equation of motion of USV considering the influence of algae is to replace the relative velocity of current and USV with existing equation of motion instead of directly applying force and moment applied to the hull by algae to direct kinetic equation. That is, the fluid force acting on the USV by the fluid is dependent on the relative velocity on the fluid and the USV.

The following equation (2.10) represents algebraic component in the earth's fixed coordinate system, taking into account the average flow velocity and direction of the flow of two-dimensional current.

$$\begin{aligned} u_c^E &= V_c \cos\beta \\ v_c^E &= V_c \sin\beta \end{aligned} \tag{2.10}$$

In this paper, it is possible to assume that ϕ , θ are 0 since the model of the tidal current is considered in the horizontal plane. If velocity and direction of the current are defined, as shown in Fig. 2-6, the current on the earth fixed coordinate system can be represented by the USV body-fixed coordinate system

through the coordinate transformation which can be expressed by the following equation (2.11). Finally, the current for each axis in the body-fixed coordinate system can be obtained from euations. (2.10) and (1.11) as (2.12).

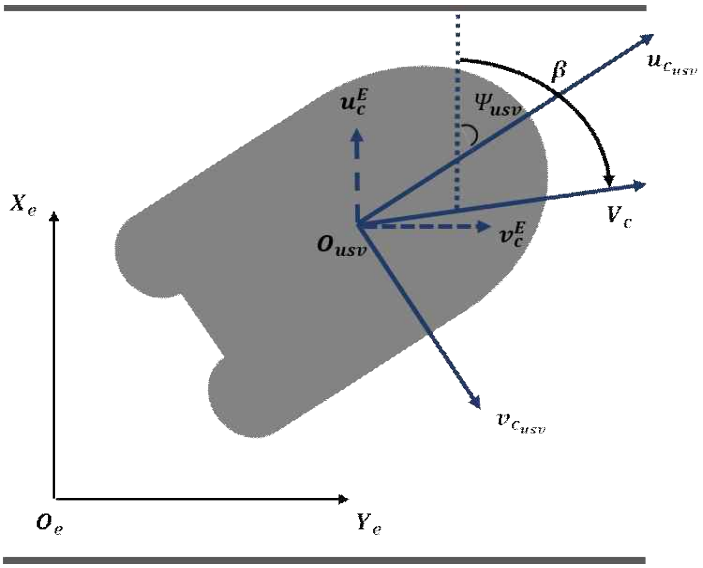

Fig 2-6 Define velocity V_c and direction β of current

$$\begin{bmatrix} u_{c_l} \\ v_{c_l} \end{bmatrix} = \begin{bmatrix} \cos\psi_l & \sin\psi_l \\ -\sin\psi_l & \cos\psi_l \end{bmatrix} \begin{bmatrix} u_c^E \\ v_c^E \end{bmatrix} \tag{2.11}$$

$$u_{c_l} = V_c \cos(\beta - \psi_l) \tag{2.12}$$

$$v_{c_l} = V_c \sin(\beta - \psi_l)$$

2.1.2.4 Open-Loop Simulations

A simple open-loop simulation such as linear motion and pivot motion was performed to confirm the 3-DOF equation of motion with effective thrust, wind load, and current considered as external force. Simulation results show that the motion of the USV is affected by the environmental load and the non - operating load.

Simulation results showed that the motion of the USV was affected by the environmental load and the non-operating load.

The simulation was constructed using Matlab & Simulink. The Runge-Kutta method was used for numerical analysis. The graph below shows results for each simulation.

Simulation No.1 Straight Motion

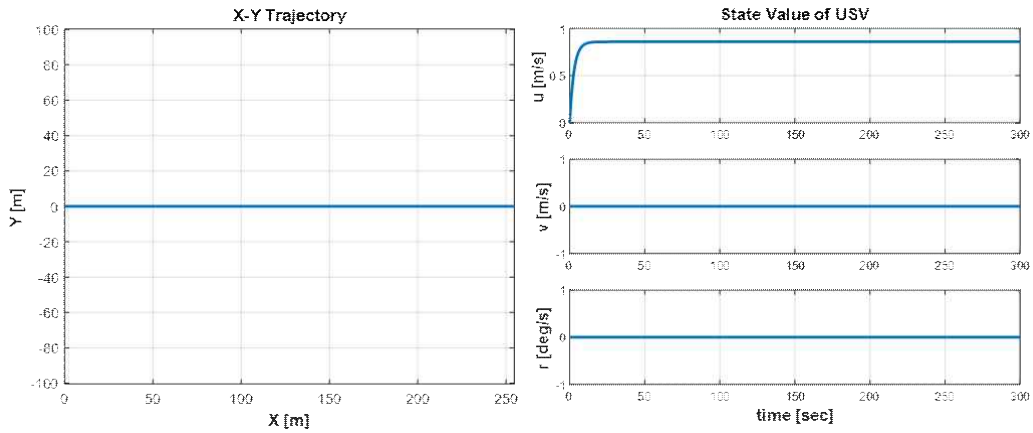

Fig 2-7 Simulation Result of USV straight motion

Simulation No.2 Turning Motion

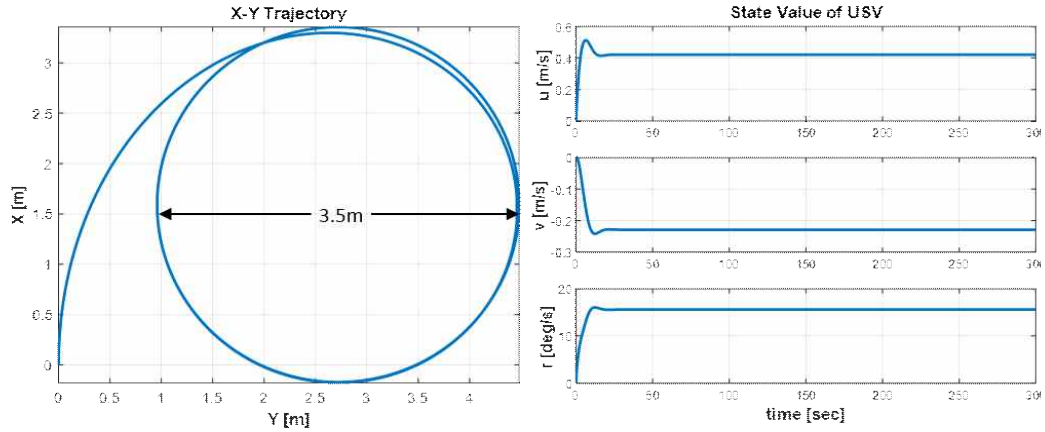

Fig. 2-8 Simulation result of USV turning motion

Simulation No.3 Turning Motion with wind load

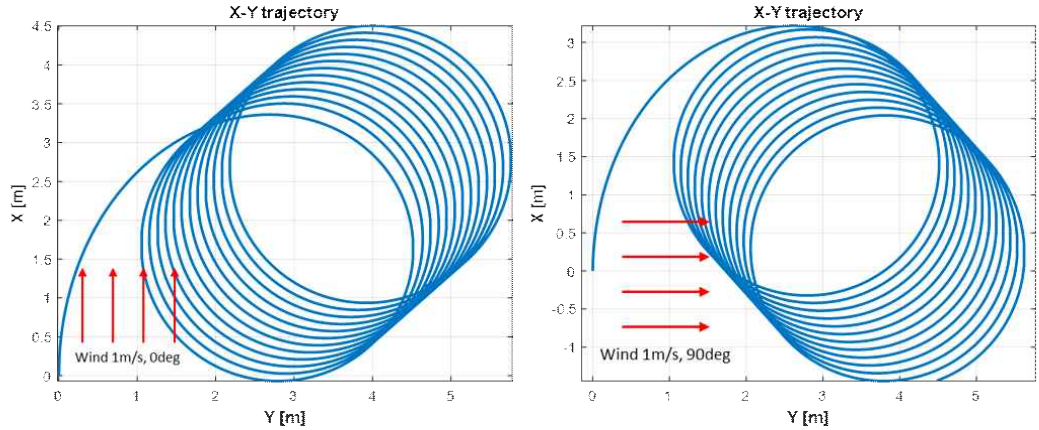

Fig. 2-9 Simulation results of turning motion of USV including wind load

Simulation No.4 Turning Motion with current

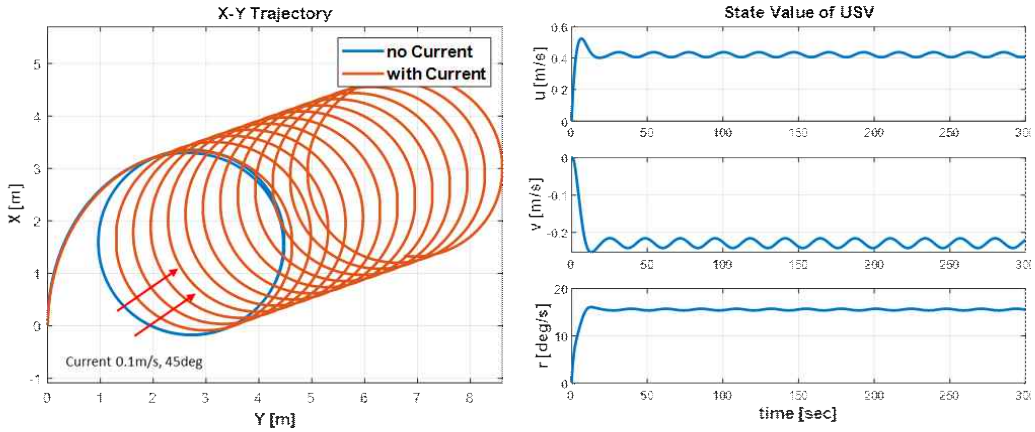

Fig. 2-10 Simulation results of turning motion of USV including current

Simulation 3 confirmed the validity of the induced wind load model through turning drift angle and drift distance caused by wind force of 1 m/s and wind direction of 0° and 90°, respectively. Simulated results of turning motion of the USV with 0.1 m/s and 45 deg current indicate that the USV drifted in the same direction as the direction of the current.

Simulations 1 and 2 showed motion of USV without disturbance. The thrust at the forward motion was input to each propeller with a thrust of 30 kgf. It was confirmed that the USV moved at a speed of about 0.8 m/s in the positive direction of the X-axis.

In simulation 2, 30 kgf and 15 kgf were input to the port and starboard thruster, respectively. It was confirmed that the USV had a turning radius of 1.75 m and an angular velocity of 16 deg/sec.

2.2 Dynamics Modeling of Unmanned Underwater Vehicle

2.2.1 Preliminary Modeling of the Unmanned Underwater Vehicle

In general, the dynamics model of an UUV can be expressed as a 6-DOF nonlinear equation of motion. Induced equations of motion include control forces (forces and moments) generated by control input devices such as thrust. In addition, various hydrodynamics forces issued according to the behavior of the UUV are included.

These hydrodynamic forces are related to the speed and acceleration of the unmanned underwater vehicle. They are also affected by the shape of the unmanned underwater vehicle and the attached equipment. Studies on dynamic modeling of UUV have been going on for a long time. Gertler and Hagen have summarized motion equations which are the standard for motion analysis of the UUV. Abkowitz [9] has proposed modified equations of motion that are more similar to actual ones. Fossen has developed a model equation for nonlinear control system design of submersible. Healley and Lienard [5] have presented 6-DOF nonlinear equations of motion and fluid dynamics of NPS AUV II.

In this paper, a kinetic model is developed based on Fossen's equation of motion. Hydrodynamic coefficients used in the dynamics model are based on hydrodynamic coefficients used in the Remus100 model for a similar unmanned underwater vehicle [10][11].

2.2.2 Dynamics of Unmanned Underwater Vehicle (UUV)

The UUV developed in this study has a torpedo type and two thrusts at the stern with one thrust at the head. Fig. 2-11 shows the shape of the UUV and Table 2-5 shows its length and weight.

Fig 2-11 Shape of Unmanned Underwater Vehicle

Table 2-5 Specification of UUV

Parameter	Value
Length (m)	1.79
Beam (m)	0.25
Weight in water (kg)	12
Weight in air (kg)	30

The coordinate system defined to derive equations of motion of the UUV is shown in Figure 2-12 below. The coordinate system defines the reference coordinate system, the earth-fixed coordinate system, and the body-fixed coordinate system. Generally, a UUV has a geometric symmetry plane. Its center of buoyancy is located on this geometric symmetry plane. Therefore, if

body-fixed coordinate system is attached to the center of buoyancy, 6-DOF nonlinear equations of motion can be further simplified by using symmetry. In the body-fixed coordinate system, the right-hand coordinate system is used in which the forward direction is the positive axis, the starboard direction is the positive axis, and the water depth direction is the positive axis.

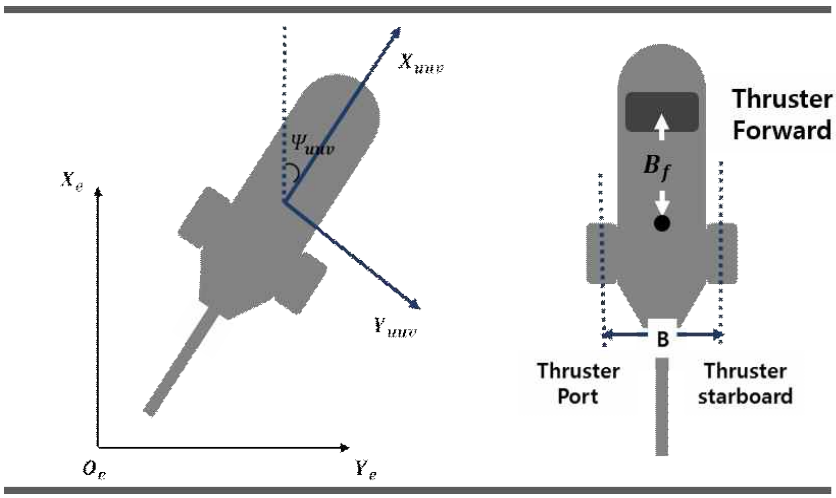

Fig. 2-12 Coordinate System of UUV

Kinematic equations of the UUV can be derived by describing relative motion of the body-fixed coordinate system to the reference coordinate system, the earth-fixed coordinate system. Also, each kinematic variable expressed in the body-fixed coordinate system and the earth-fixed coordinate system can be converted to each other through a rotation matrix.

Equation (2.13) shows transformation between kinematic variables expressed in the hull fixed coordinate system and kinematic variables expressed in the earth fixed coordinate system.

$$\dot{\eta} = R(\eta)\nu \quad ; \quad \begin{bmatrix} \dot{\eta}_1 \\ \dot{\eta}_2 \end{bmatrix} = \begin{bmatrix} R_1(\eta_2) & 0_{3\times 3} \\ 0_{3\times 3} & R_2(\eta_2) \end{bmatrix} \begin{bmatrix} \nu_1 \\ \nu_2 \end{bmatrix} \tag{2.13}$$

Where matrix $R(\eta)$ represents the transformation matrix between coordinate systems. Position vector and velocity vector of the unmanned submersible expressed in terms of the earth-fixed coordinate system and the body-fixed coordinate system can be wit as Eq. (2.14).

$$\eta_{f=[\eta_1}\ ,\ \eta_2]^T \quad ; \quad \eta_1 = [x_f,\, y_f,\, z_{f]}^T \quad , \quad \eta_2 = [\phi_f,\, \theta_f,\, \psi_{f]}^T \tag{2.14}$$

$$\nu_{f=[\nu_1}\ ,\ \nu_2]^T \quad ; \quad \nu_1 = [u_f,\, v_f,\, w_{f]}^T \quad , \quad \nu_2 = [p_f,\, q_f,\, r_{f]}^T$$

Where η_1 , η_2 are vectors representing the position and attitude of the UUV as expressed in the earth fixed coordinate system, and are linear velocity vector and angular velocity vector of the UUV expressed in the body-fixed coordinate system, respectively. The transformation matrix for transforming linear velocity expressed in the body-fixed coordinate system to the earth-fixed coordinate system can be expressed using Euler angles. The matrix is shown in Appendix A.

To describe the behavior of a UUV in water, both rigid-body dynamics and fluid dynamics should be considered. In particular, in terms of fluid dynamics, it is assumed that "force and moment due to a fluid acting on a rigid body can be linearly superimposed" can be applies to rigid body dynamics [5].

Thus, 6-DOF nonlinear equations of the UUV can be expressed as a vector expression as shown in Equation (2.15) below.

$$M_f \dot{\nu}_f + C_f(\nu_f)\nu_f + D_f(\nu_f)\nu_f + g(\eta_f) = \tau_f \tag{2.15}$$

Here, M_f , C_f represent the inertia matrix of the UUV including the effect of the added mass, and the Coriolis matrix of the UUV including the influence by the fluid, respectively. D_f means fluid damping force when an UUV moves at arbitrary speed in the water and g indicates hydrostatic or restoring force generated by gravity and buoyancy. Detailed references to each scheme are shown in Appendix A.

The right side of equation (2.15) represents force due to disturbance such as force, moment, and algae by the thruster. Equations of motion of the UUV are derived by substituting elements of the matrix attached in Appendix A. Finally, the following equation (2.16) can be obtained.

$$\begin{aligned}
&m_f[\dot{u}_f - v_f r_f + w_f q_f - x_{g_f}(q_f^2 + r_f^2) + y_{g_f}(p_f q_f - \dot{r}_f) + z_{g_f}(p_f r_f + \dot{q}_f) = \Sigma X_f \\
&m_f[\dot{v}_f - w_f p_f + u_f r_f - y_{g_f}(r_f^2 + p_f^2) + z_{g_f}(q_f r_f - \dot{p}_f) + x_{g_f}(p_f q_f + \dot{r}_f) = \Sigma Y_f \\
&m_f[\dot{r}_f - v_f r_f + v_f p_f - z_{g_f}(p_f^2 + q_f^2) + x_{g_f}(r_f p_f - \dot{q}_f) + y_{g_f}(r_f q_f + \dot{p}_f) = \Sigma Z_f \\
&I_{x_f}\dot{p} + (I_{z_f} - I_{y_f})q_f r_f + m_f[y_{g_f}(\dot{w}_f - u_f q_f + v_f p_f) - z_{g_f}(\dot{v} - w_f p_f + u_f r_f)] = \Sigma K_f \\
&I_{y_f}\dot{q} + (I_{x_f} - I_{z_f})r_f p_f + m_f[z_{g_f}(\dot{u}_f - v_f r_f + w_f q_f) - x_{g_f}(\dot{w} - u_f q_f + v_f p_f)] = \Sigma M_f \\
&I_{z_f}\dot{r} + (I_{y_f} - I_{x_f})p_f q_f + m_f[x_{g_f}(\dot{v}_f - w_f p_f + u_f r_f) - y_{g_f}(\dot{u} - v_f r_f + w_f p_f)] = \Sigma N_f
\end{aligned} \tag{2.16}$$

Where m_f is the mass of the UUV, $[I_{x_f}, I_{y_f}, I_{z_f}]^T$ is the mass secondary moment in the X, Y, Z axis direction, and $[x_{g_f}, y_{g_f}, z_{g_f}]^T$ is the center of gravity. The right side represents the sum of forces due to disturbance and propulsive force generated by the propeller.

Influence of marine environment on the UUV is less than that by disturbances such as waves and winds considering that UUV is operated in water. Therefore, in this study, it was assumed that the force and moment due to currents were the only disturbances. In this case, influence of the current was the same as the current considered in the disturbance of the USV described above.

2.2.2.1 Control force and moment by thrusters of UUV

The UUV developed in this study is equipped with two propellers to obtain the control force in the X-axis direction. A lateral propeller is mounted in the front to obtain the moment in the Z-axis direction. In this case, the moment in the X-axis direction generated by the propeller is not considered. Therefore, the control force and moment generated by the propeller can be expressed with the following equation (2.17).

$$\begin{bmatrix} X_{thrust} \\ 0 \\ 0 \\ 0 \\ 0 \\ N_{thrust} \end{bmatrix} = \begin{bmatrix} T_{port} + T_{stbd} \\ 0 \\ 0 \\ 0 \\ 0 \\ T_{\mathrm{forward}} B_f \end{bmatrix} \tag{2.17}$$

The propeller of the UUV was Model 300 of Tecnadyne Company. Equation (2.18) shows the relationship between thrust curves and the thrust for input voltage.

$$T_f = 0.002 \times V^5 + 0.03 \times V^4 + 0.356 \times V^3 + 0.47 \times V^2 + 0.782 \times V \quad (2.18)$$

2.3 Cable Dynamic Model

The combined unmanned ocean vehicle is connected to a USV and UUV by an underwater cable. Forces generated by the motion of the underwater cable can affect the motion of the combined unmanned ocean vehicle. However, since the size of the USV is relatively large compared to that of the UUV, the movement of the underwater cable and the UUV has little effect on the behavior of the USV. Therefore, it is necessary to study the effect of force generated by the underwater cable on the motion of the UUV.

2.3.1 Preliminary Modeling of the Underwater Cable

Underwater cable plays an important role in the communication and power supply of USV and UUV. However, resistance of the cable to the UUV also interferes with or restrains the movement. Therefore, it is necessary to design a controller to compensate for the effect of underwater cable on UUV.

Buckham has conducted extensive research on underwater vehicles including

cables of storage capacity [12][13]. Main researches related to the present study are as follows. When USV moves along with towed cable and towed vehicle, Grosenbaugh has shown movement of the cable in three dimensions when USV is turning. Huang has analyzed the motion of the cable by using multibody kinematic modeling when the cable length of the USV is changed [14][15]. In Choo and Cassarella's cable modeling studies, many methods have been used to analyze cable dynamics. These methods include continuous and discrete methods, finite element methods, linearization methods, and lumped-mass methods. In 1994, Kamman and Huston conducted a study on towed and tethered cable systems of marine vehicles [16][17]. In the present study, forces acting on the cable were derived by using the lumped-mass method while equation of motion was derived using Newton's second law [18][19][20][21][22].

2.3.2 Underwater Cable Model

The cables are considered small rigid segments instead of continuous non-rigid members. Each segment has a coordinate system and expresses the motion for each segment using an individual coordinate system as an equation and applies it to the whole system. The following assumptions are made to derive the equation of motion of the cable.

- The umbilical cable is incompressible
- The cable surface is relatively smooth, ignoring the attachments on the cable
- The bending stiffness of the cable is ignored. The umbilical cable can only resist the tension force, but not the bending moment and the compression

force.

- The torsional rigidity and the quality of cable point rotation effect, which do not consider the torque, are ignored.

First, to derive equation of motion of underwater cable, the inertia coordinate system determines the Y-axis by using the right-hand rule in the right direction, the right direction as X, the downward direction as Z, and the right-hand rule as shown in Fig. 2.9. The underwater cable can be divided into n segments, and a lumped mass method can be applied. At this time, the node has n+1. To derive the equation of motion of the underwater cable, the mass of the cable segment is centered on the segment center. It defines the local coordinate system(p_1, p_2, q) with mass as an origin. Each axis of the coordinate system means a normal vector, a bi-normal vector, and a tangent vector.

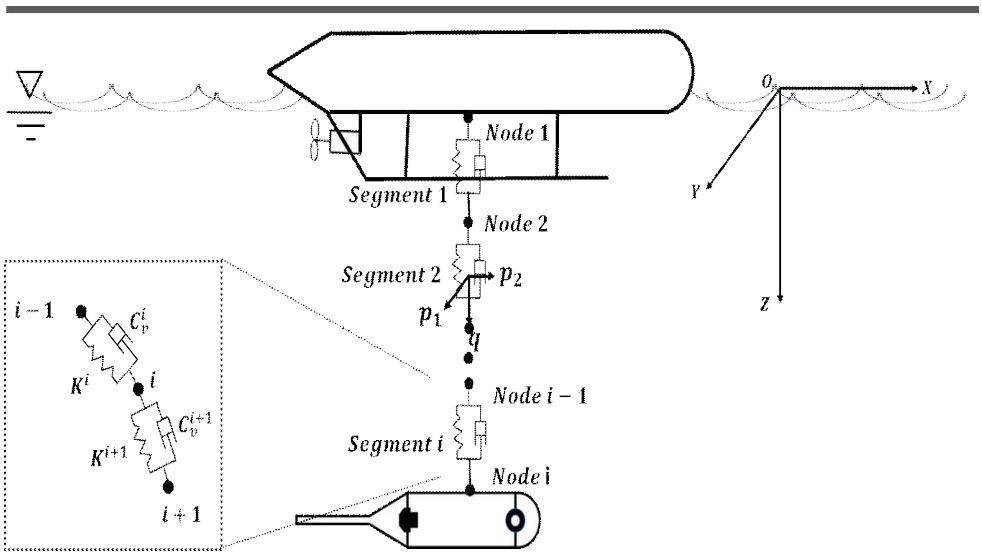

Fig. 2-9 Coordinate System of the underwater cable

We can calculate tension, damping, and hydrodynamic drag force based on the defined local coordinate system with these forces acting as constraints on the motion of adjacent nodes.

2.3.2.1 Kinematics of the underwater cable

The orientation of each segment can be expressed using a Euler angle. Since we do not consider torsion of the cable about the Z-axis, we can define the matrix q for converting from the local coordinate system to the inertial coordinate system considering only the rotation about X and Y axes as follows.

$$R_{IB}^{i} = \begin{bmatrix} \cos\theta^{i} & \sin\theta^{i}\sin\phi^{i} & \sin\theta^{i}\sin\phi^{i} \\ 0 & \cos\phi^{i} & -\sin\phi^{i} \\ -\sin\theta^{i} & \cos\theta^{i}\sin\phi^{i} & \cos\theta^{i}\cos\phi^{i} \end{bmatrix} \tag{2.19}$$

The Euler angle included in equation (2.19) can be calculated as follows, considering the position of the cable node.

$$\theta^{i} = atan2(r_{X}^{i} - r_{X}^{i-1}, r_{Z}^{i} - r_{Z}^{i-1}) \tag{2.20}$$

$$\text{if } \cos\theta^{i} > \sin\theta^{i}$$

$$\phi^{i} = \tan^{-1}(-(r_{Y}^{i} - r_{Y}^{i-1}), \frac{(r_{Z}^{i} - r_{Z}^{i-1})}{\cos\theta^{i}})$$

$$\text{if } \cos\theta^i < \sin\theta^i$$

$$\phi^i = \tan^{-1}(-(r_Y^i - r_Y^{i-1}), \frac{(r_X^i - r_X^{i-1})}{\sin\theta^i}) \tag{2.21}$$

2.2.3.2 Internal & External Force

According to the lumped mass method, the internal force generated in the underwater cable includes tension and damping while the external force includes gravity, buoyancy, and drag force. Each force acts on the center of the segment. It can be defined as described below.

The method of calculating and applying tensile force to the three axes that occur due to elastic movement of the cable among forces acting inside is shown in a previous study [14]. According to this method, the tension acting on the tangential element can be expressed as a linear function as follows (2.22).

$$T^i = EA\epsilon^i \quad , \quad \epsilon^i = \frac{l^i - l_0^i}{l_0^i} \tag{2.22}$$

Where l_0^i is the undeformed $i\,th$ segment, A is the cross-sectional area of the cable, and E is the modulus of elasticity. The axial force generated by the damping between tangential strain and damping force can be defined with the following equation (2.23).

$$P^i = C_v(V_q^i - V_q^{i-1}) \tag{2.23}$$

In equation (2.23), V_q^i represents the speed in the tangential direction of the $i\ th$ node and damping coefficient.

The external force acting on the underwater cable includes hydrodynamic force, weight, and buoyancy, and fluid resistance acting on the underwater cable that originates from the movement of water or cable. Assuming that the radius and length of the underwater cable and the exposed cable outside the water are almost free, forces due to waves can be ignored[23][24].

Therefore, waves are not modeled. Only a constant current is assumed. Thus, water surrounding the cable is not accelerated. This means that there is no dynamic pressure gradient around the water. The Froude-Krilov force is zero. The force generated by the relative velocity of the fluid can be expressed with Equation (2.24) below.

$$D_{p1}^i = -\frac{1}{2}\rho_w C_d d_c l_0^i f_p |V^i|^2 \frac{V_{p1}^i}{\sqrt{(V_{p1}^i)^2 + (V_{p2}^i)^2}} \tag{2.24}$$

$$D_{p2}^i = -\frac{1}{2}\rho_w C_d d_c l_0^i f_p |V^i|^2 \frac{V_{p2}^i}{\sqrt{(V_{p1}^i)^2 + (V_{p2}^i)^2}}$$

$$D_q^i = -sgn(v_q^i)\frac{1}{2}\rho_w C_d d_c l_0^i f_q |V^i|^2$$

Where D_{p1}^{i} , D_{p2}^{i} , D_{q}^{i} represent kinematic force for each axis expressed in the local coordinate system. ρ_w, C_D, d_c, V^i denote density of water, resistance coefficient, cable diameter, and relative velocity of the cable and the fluid, respectively. Also, f_p , f_q denote the loading function for determining the drag coefficient. They are expressed by the following equation (2.25) [25].

$$f_p = 0.5 - 0.1\cos(\eta) + 0.1\sin(\eta) - 0.4\cos(2\eta) - 0.11\sin(2\eta)$$

$$f_q = 0.01(2.008 - 0.3858\eta + 1.9159\eta^2 - 4.1615\eta^3 + 3.5064\eta^4 - 1.1873\eta^5$$

(2.25)

The hydrodynamic force acting on each node shares hydrodynamic force acting on adjacent segments. It has a value of half.

Mass and buoyancy can be obtained with the following equation (2.26).

$$m_c^i = \rho_c g V_c^i \qquad (2.26)$$

$$B^i = \rho_w g V_c^i$$

Where, ρ_c , g , V_c^i denote cable density, gravitational acceleration, and volume of the segment.

An object moving in water is subjected to an additional mass by the fluid.

For the tangential direction, the added mass is not considered. The mass matrix of each segment is as follows.

$$M_B^i = \begin{bmatrix} m_c^i + m_a^i & 0 & 0 \\ 0 & m_c^i + m_a^i & 0 \\ 0 & 0 & m_c^i \end{bmatrix} \tag{2.27}$$

The mass matrix can be expressed in the inertial coordinate system using the transformation matrix defined above. It can be expressed by the following equation.

$$M_I^i = \frac{1}{2} R_{IB}^i M_B^i R_{IB}^{iT} + \frac{1}{2} R_{IB}^{i+1} M_B^{i+1} R_{IB}^{i+1T} \tag{2.28}$$

Using the force acting on each segment and the second law of Newton, we can derive the equation of motion of underwater cable as follows.

$$M_I^i \ddot{r}^i = (T^{i+1} + P^{i+1}) - (T^i + P^i) + \frac{1}{2}(D^i + D^{i+1} + m_c^i + m_c^{i+1}) - \frac{1}{2}(B^i + B^{i+1}) \tag{2.29}$$

2.2.3.3 Open-Loop Simulation VS. Experiments

In order to verify the validity of dynamics modeling of the underwater cable, simulations were carried out under the assumption there presence of algae. Also, one end of the underwater cable was fixed, and the other side considered weight and inertia matrix of the unmanned submersible.

Simulation results in comparison with results of experiments performed in the water tank confirmed the validity of dynamics modeling of the underwater cable. The characteristics of the underwater cable used in the simulation are shown in Table 2-6 below.

Table 2-6 Specification of Underwater Cable

Parameter	Value
Cable diameter	0.025m
Cable density	3121
Cable drag coefficient	2.5
Cable damping coefficient	100
Effective modulus of elasticity	7.5×10^{6}
Total cable length	3
Cable nodes	20

Simulation was performed by changing current from 0m/s to 1m/s. Results are shown in Fig. 2-10. As speed of current increased, cables were pushed backward. Tension acting on the cable at the initial position acted most and converged with time, reaching an equilibrium state by the elastic modulus included in the cable motion equation.

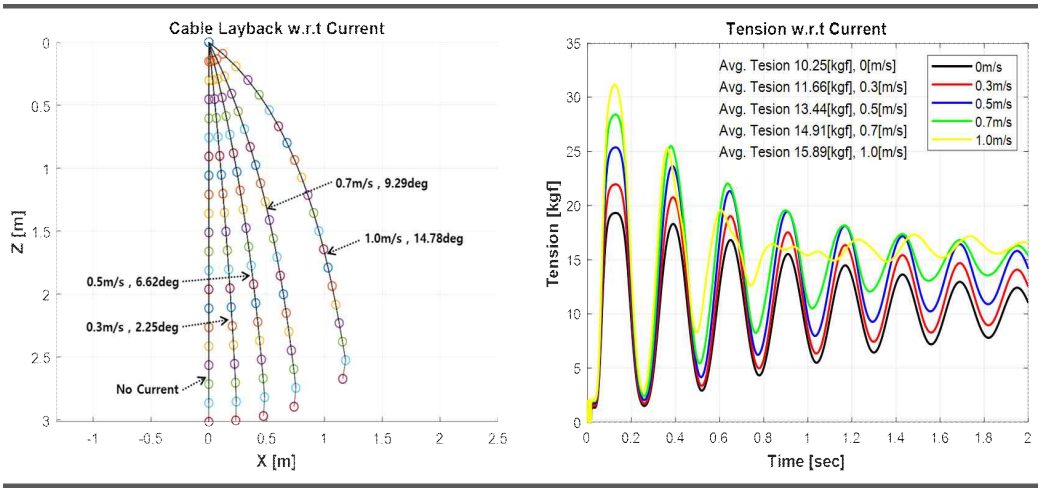

Fig. 2-10 Simulation Result of Cable Motion with Current

Figure 2-11 below shows an example of the experiment performed to measure tension acting on the cable and the angle of the cable.

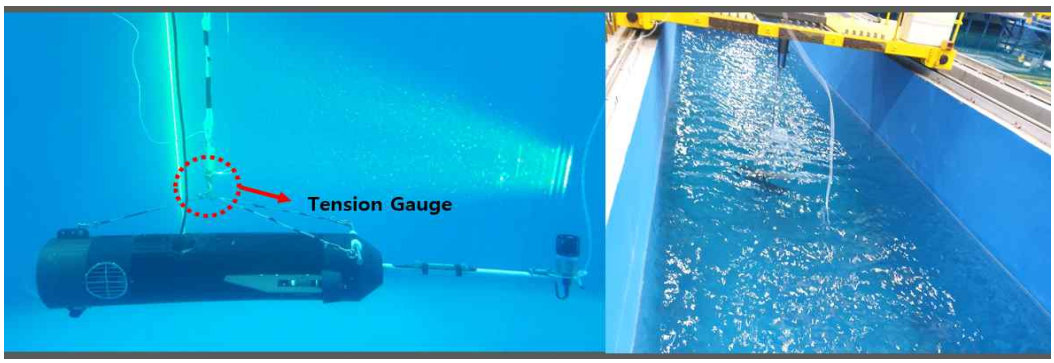

Fig. 2-11 Water tank test for measuring tension force

Figure 2-12 below shows cable angle according to current. Compared to simulation results shown in Fig. 2-10, the cable angle varied from 0.23 ° to 1.3 °. In addition, as shown in Fig. 2-13, the tension of the cable was more than

3kgf, higher than the simulation value.

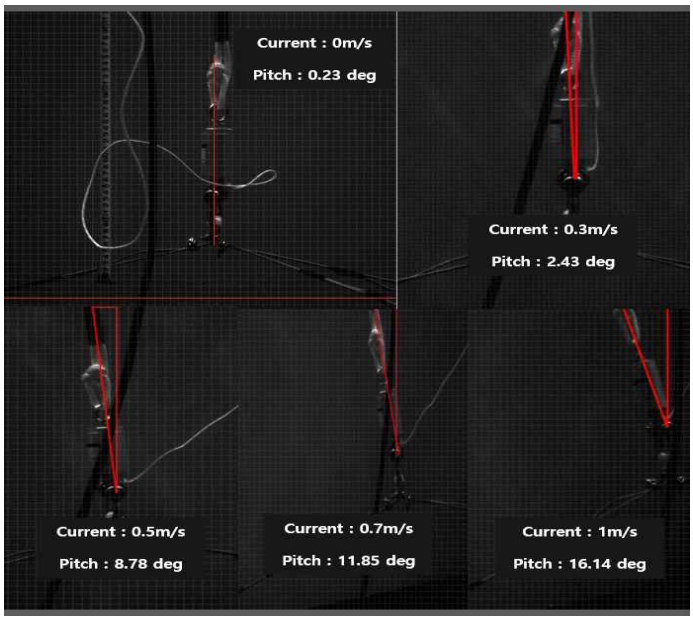

Fig. 2-12 Cable Angle with currents

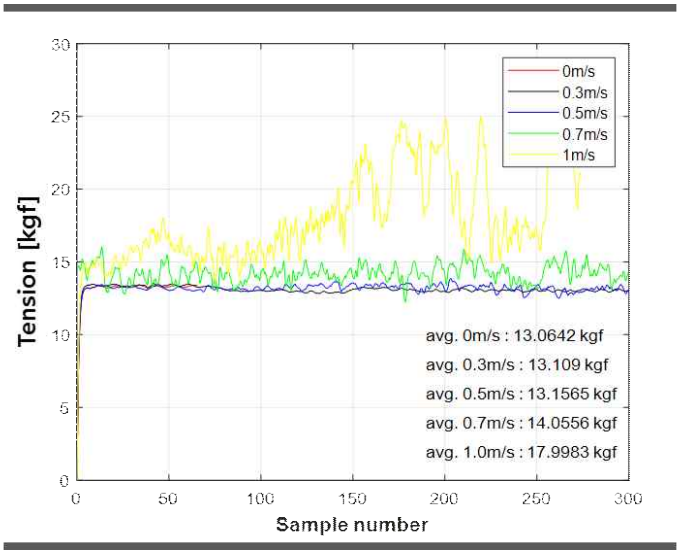

Fig. 2-13 Tension on the cable

Cable angles and tensile strengths obtained from actual experiments were not exactly the same as those in simulations. However differences in these values were not large. Their trends were similar. Therefore, it can be concluded that the equation of motion of the underwater cable derived above is valid.

2.4 Combine with Underwater Cable and UUV

Finally, we need a motion model that integrates UUV and underwater cable. To this end, we added one node to each end of the UUV cable to change cable shape and internal tension according to the position and velocity of UUV. These added nodes and segments depend on the position, velocity, and inertia matrix of the USV and UUV. In this study, the influence of cable on the external force was considered to be small in the case of USV with relatively large mass and size of underwater cable and UUV. Only the force by cable acting on unmanned submersible was considered.

As described above, movement of UUV will change the position and speed of the end of the cable, resulting in changes in cable shape and internal tension. Change in cable tension can be said to be a recurrent process that affects movement of the UUV. Therefore, interaction between the UUV and the underwater cable can be expressed with the following equations (2.30) to (2.31).

$$u_{i+1} = J_1(v_1 + v_2 \times r_c) \tag{2.30}$$

$$r_{i+1} = r_f + J_1 r_c \tag{2.31}$$

Where J_1 denotes the transformation matrix from the body-fixed coordinate system to the earth-fixed coordinate system, and r_c denotes the position vector of the point where the cable is connected in the hull fixed coordinate system of the unmanned submersible.

Position, velocity, and force of the cable are expressed with reference to the fixed coordinate system of the cable as defined above. Therefore, it is necessary to express the force acting on the UUV by the fixed coordinate system. The relation for this can be expressed with the following equation (2.32).

$$F_{bcable} = -J_1^{-1} T_{n+1} \tag{2.32}$$

$$M_{bcable} = r_c \times (-J_1^{-1} T_{n+1})$$

Considering force and moment of the cable in the equation of motion of the UUV as described above, it can be expressed as follows.

$$M_f \dot{\nu}_f + C_f(\nu_f)\nu_f + D_f(\nu_f)\nu_f + g(\eta_f) = \tau_f + \tau_{cable} \tag{2.33}$$

where, $\tau_{cable} = [F_{bcable}\ ,\ M_{bcable}]^T$

3. Guidance and Control for Combined Unmanned Ocean Vehicle

Fig. 3-1 below shows a block diagram of leader-follower control. As shown in Fig. 3-1, each platform includes guidance and control.

In order to perform work more efficiently by enabling cooperative work of the same kind or different kind of robot, a certain interval and angle that the robot keeps with respect to the target or another robot are called a formation. The method for controlling it is called formation control. These formation control schemes can be roughly classified into three types: behavior-based approach, leader-follower approach, and virtual structure approach [26][27][28][29][30][31].

In this study, a leader-follower control method was applied to follow the way-point of the combined unmanned ocean vehicle. GPS-based USV which enables precise position measurement plays the role as leader while UUV that uses USBL information acts as a follower to follow the path of the USV. The leader-follower approach is primarily aimed at maintaining formation of the USV. In the case of the leader, control is performed for the purpose of way-point tracking or obstacle avoidance. The follower controls the formation of the leader.

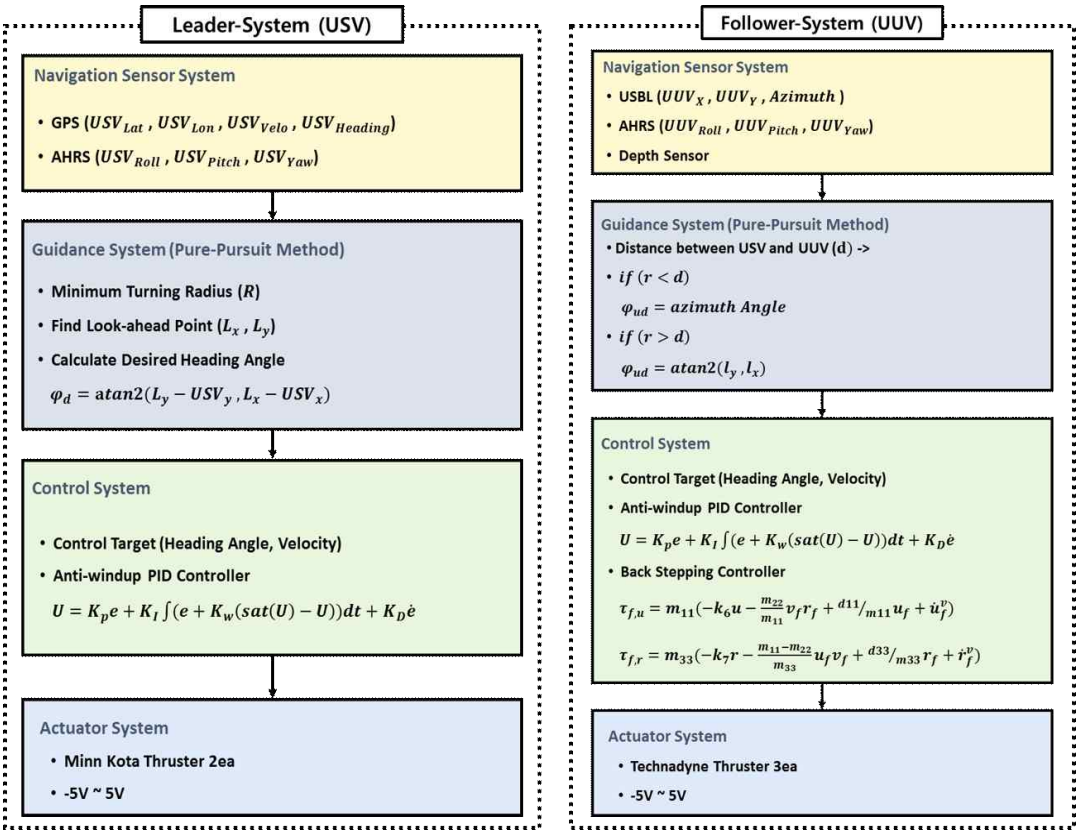

Fig 3-1 Block diagram of leader-follower of combined unmanned ocean vehicle

3.1 Guidance Method for USV

The general path tracking method defines the difference between the distance of the USV of the reference path and the heading angle of the USV, respectively. Then, it is controlled to reduce the error of the defined distance and direction angle for tracking the path. It is necessary to guarantee the stability of the path-following controller since what kind of movement that control variables will directly drive the USV is not predictable. On the other

hand, the geometric path tracking method uses the predicted distance as a control variable of the path follower so that the path following controller can directly generate target motion of mobile robot. In this study, we used Pure Pursuit method among geometric path tracking methods to obtain turning radius to follow the path and select necessary point to follow the path [32][33][34].

Fig. 3-2 below shows how USV returns to the reference path by using Pursuit path tracking method.

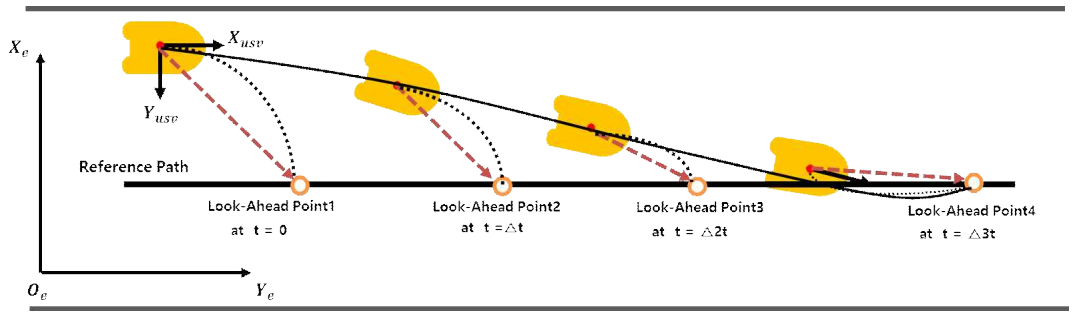

Fig. 3-2 Pure Pursuit Method

In general, the path can be divided into a continuous path and a set of discontinuous way-points. However, in the case of continuous path, since the path is defined as a function on a two-dimensional plane, it causes an unnecessary calculation amount when applied to actual hardware. Therefore, in this paper, we defined the path to follow a set of way-points.

If geometric relationship is defined in order to obtain the turning radius for the USV to follow a given path as shown in the following Figure (3-3), then the following equations (3.1) - (3.3) can be obtained from the defined geometric relationship.

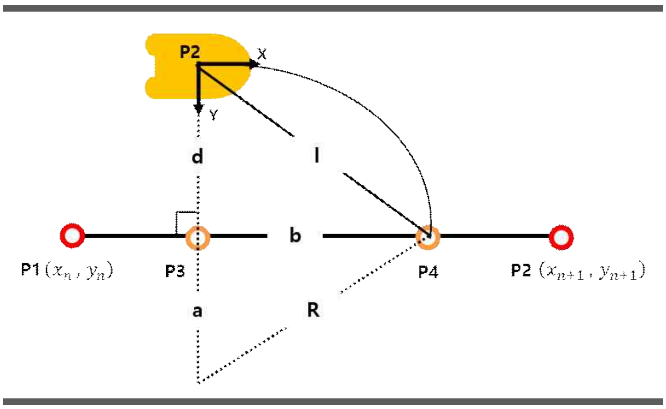

Fig. 3-3 Geometry of pure pursuit

$$d^2 + b^2 = l^2 \tag{3.1}$$

$$a^2 + b^2 = R^2 \tag{3.2}$$

$$a = R - d \tag{3.3}$$

Substituting Eq. (3.3) into Eq. (3.2)

$$(R-d)^2 + b^2 = R$$

$$d^2 + b^2 = 2Rd \tag{3.4}$$

By substituting Eq. (3.1) into Eq. (3.4), the turning radius in Fig. 3-3 (that is, the turning radius to follow the path) can be obtained as follows.

$$R = \frac{l^2}{2d} \tag{3.5}$$

The performance of the path-following controller using the geometric path-following method depends on the prediction distance. The foresight distance may be determined by the operator at an arbitrary value. However, in this case, the path following performance is deteriorated or the USV is abruptly moved. Therefore, we need to select the look-ahead point considering motion of the USV. The performance of the path-following controller is more influenced by the rotational motion than by the linear motion of the USV. In this study, we used the relationship between the minimum turning radius and the predicted distance of the USV to determine the look-ahead point. Fig. 3-4 shows the relationship between the minimum turning radius and the predicted distance of the USV.

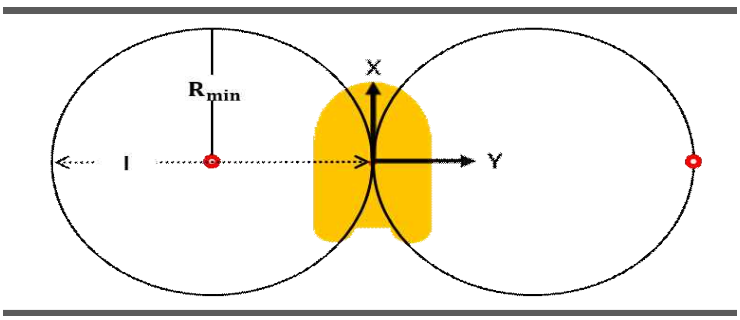

Fig. 3-4 Look-ahead Point and Minimum Turning Radius

As can be seen in Fig. 3-4, the turning radius is minimized when the position of the foresight is on the Y-axis of the coordinate system. Therefore, the minimum turn radius and the predicted distance have a relationship, as shown in the following equation (3.6).

$$l = 2R_{\min} \tag{3.6}$$

When the USV is operating independently, the minimum turn radius of the USV should be considered. However, in the case of combined unmanned ocean vehicle developed in this study, motion performance of the UUV should also be considered. Therefore, a large turning radius of the minimum turning radius of each platform obtained through simulation was used to obtain the predicted distance.

If the predicted distance is determined, the look-ahead point on the reference path should be determined using the geometric relationship described above. The following steps are necessary to determine the predictor using Fig. 3-3.

Table 3-1 Calculate a desired heading angle

Step 1. Obtain current position of the USV from GPS
Step 2. Find straight line using Way-Point
Step 3. Find shortest point on the reference path
Step 4. Calculate the look-ahead point d , l
Step 5. Calculate the target heading angle

3.2 Guidance Method for UUV

The advantage of the combined unmanned ocean vehicle developed in this study is that the UUV can acquire relative position of the UUV and USV using the USBL sensor and the exact location of undersea feature that is being explored. However, the USBL sensor has an error in measured value depending on the relative depth of the transceiver and ponder. Therefore, the UUV must move within a certain area based on the ponder of USBL according to the depth of water. For this purpose, the guiding method of the unmanned submersible was designed so that positions of the unmanned submersible line and the unmanned submersible could be expressed geometrically as shown in Fig 3-4.

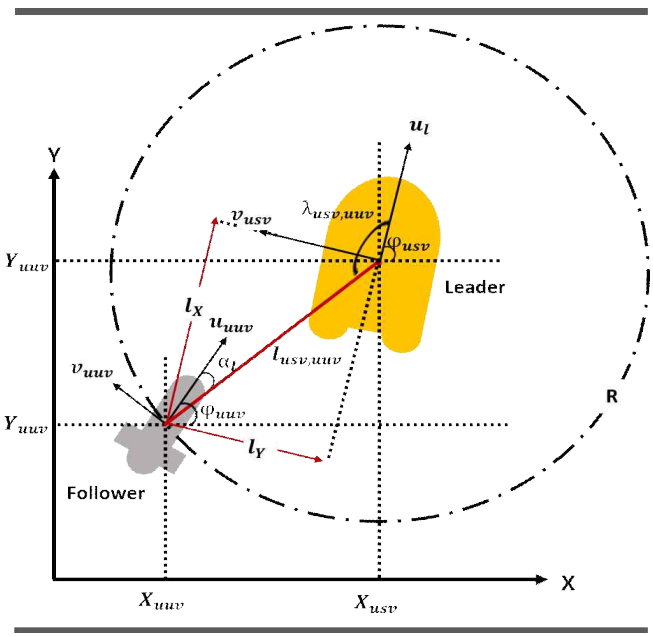

Fig. 3-4 Define geometry between UUV and USV

The meaning of the notation in Figure 3-4 is summarized in Table 3-2 below. The relative position($l_{usv,uuv}$) and the relative direction angle($\lambda_{usv,uuv}$) can be defined as $R \geq l_{usv,uuv} \in \mathbb{R} \geq 0,\ \lambda_{lf} \in (\pi/2, 3\pi/2)$

If the target relative position and the relative azimuth angle are $\mathbb{P}^{d}_{usv,uuv} = [l^{d}_{usv,uuv} \ \ \lambda^{d}_{usv,uuv}]$ while positions $(X_{usv}, Y_{usv}, \varphi_{usv})$ and $\mathbb{P}^{d}_{usv,uuv} = [l^{d}_{usv,uuv} \ \ \lambda^{d}_{usv,uuv}]$ of the unmanned water line are known or can be set, so then the position of the unmanned submersible can be uniquely determined.

Table 3-2 Notation in Fig. 3-4

R	Maximum distance between leader and follower
$(X_{usv}, Y_{usv}, \varphi_{usv})$	Position, Heading Angle of USV
$(X_{uuv}, Y_{uuv}, \varphi_{uuv})$	Position, Heading Angle of UUV
$(l_{usv,uuv}, \alpha_{usv})$	LOS range and bearing
$\lambda_{usv,uuv}$	Relative angel w.r.t USV

When the relative distance $l_{usv,uuv}$ between the USV and the UUV is projected on X and Y axes, the following equation (3.7) is obtained. Target distance for X and Y can be expressed as (3.8).

$$l_x = -(X_{usv} - X_{uuv})\cos\psi_{usv} - (Y_{usv} - Y_{uuv})\sin\psi_{usv} \tag{3.7}$$

$$l_y = (X_{usv} - X_{uuv})\sin\psi_{usv} - (Y_{usv} - Y_{uuv})\cos\psi_{usv}$$

$$l_x^d = l_{usv,uuv}^d \sin(\lambda_{usv,uuv}^d + \varphi_{usv} - \frac{\pi}{2}) \tag{3.8}$$
$$l_y^d = l_{usv,uuv}^d \cos(\lambda_{usv,uuv}^d + \varphi_{usv} - \frac{\pi}{2})$$

Finally, the guiding principle for the UUV to move along the USV is to make zero error for the relative distance $(l_x\ ,\ l_y)$, the target distance $(l_x^d\ ,\ l_y^d)$, and the target relative angle $\lambda_{usv,uuv}^d = \varphi_{usv} - \varphi_{uuv}$ over time. This can be expressed as (3.9) as shown below.

$$\lim_{t\to\infty}(l_x^d - l_x) = 0 \tag{3.9}$$

$$\lim_{t\to\infty}(l_y^d - l_y) = 0$$

$$\lim_{t\to\infty}\lambda_{usv,uuv}^d = 0$$

3.3 Designing Controller of the Combined Unmanned Ocean Vehicle

There have been many kinds of design of the controller for follow-up and mission execution of the USV and UUV. It is difficult to control the attitude and the position of the UUV because of nonlinear factors and disturbances in unpredictable environments. In this study, we designed and applied an anti-windup PID controller. It has classical but powerful control capability for leader-follower control of the combined unmanned ocean vehicle. In addition, for the control of disturbance such as force generated by the cable and current, the controller was designed using the backstepping technique based on the Lyapunov function. The controller's performance was then verified through simulation.

3.3.1 Anti-windup PID controller

In general, anti-windup processing must be done when using I controller of PID or PI controller. Anti-windup refers to the subtraction of integral component according to the difference when the output is at its limit. This can prevent divergence of integral error, thus ensuring stability of the compensator in the feedback loop. Anti-windup has various methods such as conditional integration technique, tracking half-windup technique, and limited-time technique [35][36][37]. In the present study, the most generally used anti-windup method was used to design the PID controller. Block diagram of the controller is shown in Fig. 3-5 below.

In the block diagram shown in Fig. 3-5. if the output value of the controller

does not reach the limit, the signal input to K_w is 0. It operates as a general PID controller. On the contrary, when the limit is exceeded, the value obtained by multiplying K_w is subtracted from the integral component. Here, K_w is a control gain for eliminating cumulative integration error. $K_p \cdot K_D$, K_I denote proportional, differential, and integral gains, respectively. Each gain can be obtained through trial-and-error method. For K_w, it is empirically set to $1/K_p$.

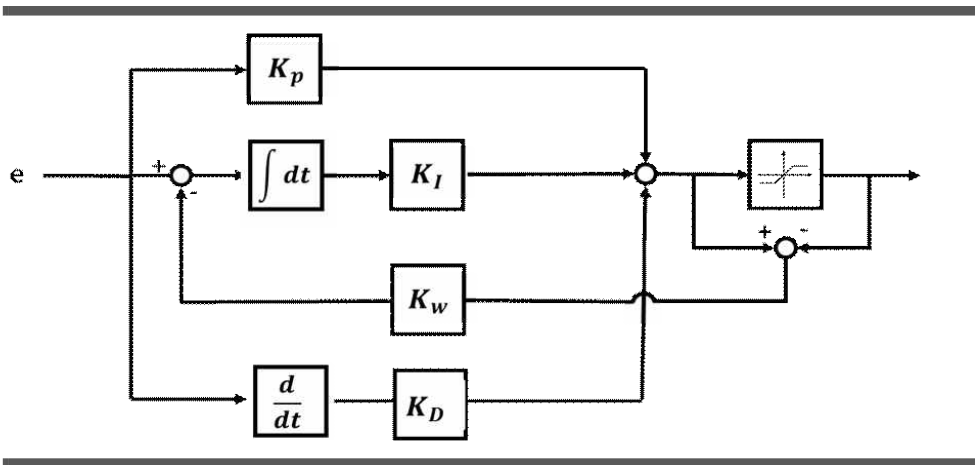

Fig. 3-5 Block diagram of Anti-windup PID controller

In this study, the speed, direction angle, relative distance, and relative direction angle of each platform are defined as the control target of the USV and UUV. The control input is set as input value of the propulsion unit installed on each platform. The control input obtained for tracking the target value of each platform is given by equations (3.10) and (3.12). The expression shows difference between the current state value and the target value of the platform.

$$U_{l,i} = K_{p,i}e_i + K_{I,i}\int (e_i + K_{w,i}(sat(U_{l,i}) - U_{l,i}))dt + K_{D,i}\dot{e}_i \tag{3.10}$$

$$i = [1,2] = [\,Velocity_{usv}\ ,\ HeadingAngle_{usv}]$$

The USV must follow the target speed and desired heading angle using two propellers. Therefore, finally, the input of the propeller is determined by using difference in thrust between the two propellers.

$$U_{l_{port}} = U_{l,1} + U_{l,2} \quad , \quad U_{l_{strboard}} = U_{l,1} - U_{l,2} \tag{3.11}$$

In the UUV, the control target position and direction angle can be controlled by using two thrusts in the forward direction and one thrust in the lateral direction. The two thrusts in the forward direction are used to follow the relative distance and generate thrust force in the forward direction. A lateral thrust is used to generate a thrust force to follow the relative directional angle.

In this study, as described above, the UUV should be positioned below the USV using USBL. Therefore, when the radius deviates from the set radius, it is necessary to find and follow the target direction angle using the relative position. However, since it is difficult to follow the relative direction angle and the target direction angle at the same time by using one thrust, it is necessary to control the relative direction angle when the radius does not deviate. It is also important to control the trade-off to follow the target direction angle when it deviates.

$$U_{f,n} = K_{p,n}e_n + K_{I,n}\int (e_n + K_{w,n}(sat(U_{l,n}) - U_{l,n}))dt + K_{D,n}\dot{e}_n$$

$$n = [1,2,3] = [Position_{uuv}\ ,\ RelativeAngle\ ,\ HeadingAngle_{uuv}]$$

(3.12)

$$U_{f_{port}} = U_{f_{strboard}} = U_{f,1} \tag{3.13}$$

$$\text{if } Position < R\ ,\ \ U_{forward} = U_{f,2}$$

$$\text{if } Position > R\ ,\ \ U_{forward} = U_{f,3}$$

3.3.2 Back-Stepping Controller

Compared with UUV, the USV is easy to control, although it affects motion disturbances in the water surface. However, it is difficult to control USV due to disturbance in uncertain environments and forces generated by underwater cables. Therefore, it is necessary to design and apply a robust controller capable of canceling the disturbance. In this study, we designed and applied a backstepping controller, a robust controller based on a Lyapunov function among nonlinear controllers.

The backstepping technique was introduced by Kokotovic in 1990. The controller design based on the Lyapunov function can be more systematic. It is a nonlinear controller that ensures safety for the entire feedback system by ensuring safety through feedback control at each stage by dividing the whole system into sub-systems. First of all, a simple backstepping control technique will be described as follows [38][39][40].

$$\begin{cases} \dot{X} = f(X) + g(X)\xi \\ \dot{\xi} = u \end{cases} \tag{3.14}$$

We assume that there exists a continuously differentiable feedback control rule $u = \alpha(X)$, $\alpha(0) = 0$ with $\xi \in R$ as input. Equation (3.14) satisfies the following condition.

$$\frac{\partial V}{\partial X}(X) = [f(X) + g(X)\alpha(X)] \leq - W(x) \leq 0 \quad , \quad \forall X \leq R^n \tag{3.15}$$

Where $V : R^n \rightarrow R$ is a positive definite, and smoothly non-radially distributed smooth function, and $W : R^n \rightarrow R$ is a positive definite or positive semi-definitive function. If $W(X)$ is a positive definite function, then the function given by Eq. (3.16) is the control Lyapunov function for the whole system. Based on this, there exists a feedback controller $u = \alpha_a(X, \xi)$ that stabilizes the equilibrium point $X = 0$, $\xi = 0$ asymptotically.

$$V_a(X, \xi) = V(X) + \frac{1}{2}(\xi - \alpha(X))^2 \tag{3.16}$$

An example of such a stabilized feedback controller can be shown in the following equation (3.17).

$$u = - c(\xi - \alpha(X)) + \frac{\partial \alpha}{\partial X}[f(X) + g(x)\xi] - \frac{\partial V}{\partial X}(X)g(X) \tag{3.17}$$

At this time, it has a value of $c > 0$

If $W(X)$ is a positive semi-definite function, there is a feedback control input $u = \alpha_a(X, \xi)$ that satisfies $\dot{V}_a \leq -W(X, \xi) \leq 0$ or $W(X, \xi) > 0$ when $\xi \neq \alpha(X)$. In addition, the state variable $[X(t)^T, \xi(X)^T]^T$ of the overall feedback control system converges to the largest invariant set contained in the set as shown in (3.18).

$$E_a = \{[X^T, \xi]^T \in R^{n+1} \mid W(X) = 0\} \tag{3.18}$$

If error variable $z = \xi - \alpha(X)$ is introduced to verify this, the state equation of the control system can be expressed with the following equation (3.20).

$$\begin{cases} \dot{X} = f(X) + g(X)[\alpha(X) + z] \\ \dot{z} = u - \dfrac{\partial \alpha}{\partial X}[f(X) + g(X)(\alpha(X) + z)] \end{cases} \tag{3.19}$$

Since equation (3.20) satisfies the assumption given by Eq. (3.15), the time derivative of the Lyapunov function $V_a(X, \xi)$ along state trajectory of the system can be obtained as shown in the following equation (3.21).

$$\dot{V}_a = \frac{\partial V}{\partial X}(f + g[\alpha + z]) + z[u - \frac{\partial \alpha}{\partial X}(f + g[\alpha + z])] \tag{3.20}$$
$$\leq W(X) + z[\frac{\partial V}{\partial X}g + u - \frac{\partial \alpha}{\partial X}(f + g[\alpha + z])]$$

Therefore, if the control input u is chosen to be $\dot{V}_a \leq -W_a(X, \xi) \leq -W(X)$, then X and z, ξ are globally dependent by the quantity-limiting nature of W_a and Lasalle-Yoshizawa's theorem while $W(X(t))$ and $z(t)$ converge to zero according to time $t \to \infty$ [39]. According to LaSalle's theorem, $[X(t)^T, \xi(t)]^T$ guarantees convergence to the largest invariant set contained in equation. (3.19). In order to satisfy this property, $\dot{V}_a$ must be a definite negative function for z. Applying the control input u given by Eq. (3.17), Eq. (3.21) is obtained as shown in the following.

$$\dot{V}_a \leq -W(X) - cz^2 = -W_a(X, \xi) \leq 0 \tag{3.21}$$

Here, if $W(X)$ is a definite quantitative function, equilibrium points $X = 0$ and $z = 0$ are asymptotically stable by LaSalle-Yoshizawa's theorem. Therefore, it can be seen that $X = 0, \xi = 0$ from $z = \xi - \alpha(X)$ and $\alpha(0) = 0$ is asymptotically stable.

The following equation (3.22) represents a general nonlinear system, The feedback controller can be designed by applying the backstepping technique even when the nonlinear system is expressed in a more general form [41][42].

$$
\begin{aligned}
\dot{X} &= f(X) + g(X)\xi_1 \\
\dot{\xi}_1 &= f_1(X, \xi_1) + g_1(X, \xi_1)\xi_2 \\
\dot{\xi}_2 &= f_2(X, \xi_1, \xi_2) \\
&\vdots \\
\dot{\xi}_k &= f_k(X, \xi_1, \dots, \xi_k) + g_k(X, \xi_1, \dots, \xi_k)u
\end{aligned}
\tag{3.22}
$$

As a result, the control input to stabilize the system asymptotically using the Lyapunov function can be derived with the following equation (3.23).

$$
u = \frac{1}{g_k}\left\{ -c_k[\xi_k - \alpha_{k-1}] - \frac{\partial V_{k-1}}{\partial \xi_{k-1}} g_{k-1} - f_k + \frac{\partial \alpha_{k-1}}{\partial X_{k-1}}[F_{k-1} + G_{k-1}\xi_k] \right\} \tag{3.23}
$$

where, if $c_k > 0$, satisfies $W_k = W_{k-1} + c_k(\xi_k - \alpha_{k-1})^2 \geq 0$

The controller given by Eq. (3.23) can feedback stabilize the whole system expressed by Eq. (3.22). As described above, the controller design using the backstepping technique is designed to show the nonlinear system as a subsystem and design the controller satisfying stability of the feedback system. The stability is then compared with the method using the Lyapunov direct method It is possible to design a controller that secures stability of the entire system more systematically.

A two-step process is required to design the controller of the target platform using backstepping technique. First, virtual controls should be designed using the errors of position and orientation angles. These virtual controls should be

designed with actual control inputs using dynamics.

3.3.2.1 Virtual Controls

The position and direction angular error of the UUV as described above is expressed by equation (3.9) and can be rewritten as equation (3.24) below. If it is differentiated, it can be expressed as equation (3.25).

$$e = \begin{bmatrix} e_1 \\ e_2 \\ e_3 \end{bmatrix} = \begin{bmatrix} l_x - l_x^d \\ l_y - l_y^d \\ \psi_l - \psi_f \end{bmatrix} \tag{3.24}$$

$$\dot{e} = \begin{bmatrix} \dot{e}_1 \\ \dot{e}_2 \\ \dot{e}_3 \end{bmatrix} = \begin{bmatrix} \dot{l}_x - \dot{l}_x^d \\ \dot{l}_y - \dot{l}_y^d \\ \dot{\psi}_l - \dot{\psi}_f \end{bmatrix} \tag{3.25}$$

$$= \begin{bmatrix} -u_f \cos e_\psi - v_f \sin e_\psi + e_y \dot{\psi}_l + u_l + l_y^d \dot{\psi}_l - \dot{l}_x^d \\ u_f \sin e_\psi - v_f \cos e_\psi - e_x \dot{\psi}_l + v_l - l_x^d \dot{\psi}_l - \dot{l}_y^d \\ r_l - r_f \end{bmatrix}$$

Since the error of the position and direction expressed in equation (3.24) is the position of the UUV, it is necessary to perform a coordinate transformation to the coordinate system of the UUV using the relative direction angle of the

USV and the UUV.

$$\begin{bmatrix}\epsilon_1\\ \epsilon_1\end{bmatrix}=\begin{bmatrix}\cos e_\psi & -\sin e_\psi\\ \sin e_\psi & \cos e_\psi\end{bmatrix}e \tag{3.26}$$

By differentiating equation (3.26), equation (3.27) can be obtained.

$$\begin{bmatrix}\dot{\epsilon}_1\\ \dot{\epsilon}_1\end{bmatrix}=\begin{bmatrix}u_f+\zeta_1\cos e_\psi-\zeta_2\sin e_\psi+\epsilon_2 r_f\\ v_f+\zeta_1\sin e_\psi+\zeta_2\cos e_\psi-\epsilon_1 r_f\end{bmatrix} \tag{3.27}$$

where, $\zeta_1=-u_l+l_y^d\dot{\psi}_l-\dot{l}_x^d$, $\zeta_2=-v_l-l_x^d\dot{\psi}_l-\dot{l}_y^d$

In order to obtain control input for speed control, the Lyapunov function is defined as follows (3.28).

$$V_1=\frac{1}{2}\epsilon_1^2+\frac{1}{2}\epsilon_2^2 \tag{3.28}$$

If we differentiate equation (3.28)

$$\begin{aligned}\dot{V}_1&=\epsilon_1\dot{\epsilon}_1+\epsilon_2\dot{\epsilon}_2 \qquad (3.29)\\ &=\epsilon_1(u_f+\zeta_1\cos e_\psi-\zeta_2\sin e_\psi)+\epsilon_2(V_f+\zeta_1\sin e_\psi+\zeta_2\cos e_\psi)\end{aligned}$$

Through equation (3.29), the control input can be determined as follows.

$$u_f^v = -k_1\epsilon_1 - \zeta_1 \cos e_\psi + \zeta_2 \sin e_\psi \tag{3.30}$$

$$v_f^v = -k_2\epsilon_2 - \zeta_1 \sin e_\psi - \zeta_2 \cos e_\psi$$

Here, if $k_1, k_2 > 0 \in \mathbb{R}$ is set, it can be seen that differential of the Lyapunov function has a negative value as shown in equation (3.31). This indicates that the velocity error converges to zero asymptotically.

$$\dot{V}_1 = -k_1\epsilon_1^2 - k_2\epsilon_2^2 \leq 0 \tag{3.31}$$

The v_f^v derived from the above equation (3.30) can not be directly controlled by considering arrangement of the propeller in the Sway direction of the unmanned submersible. Instead of using equation (3.30), we can satisfy the control objective by obtaining virtual control of the directional angle, which is related to velocity in the Sway direction.

In this study, the UUV is supposed to exercise only 6-DOF in the water, but only 3-DOF (Surge, Sway, Yaw) in terms of control. As mentioned in a previous study [5], if the equation is simplified by ignoring heave, roll, and pitch movements, the equation of 3-DOF of the UUV can be expressed with equation (3.32) as follows.

$$
\begin{aligned}
&m_{11}\dot{u}_f - m_{22}v_f r_f + d_{11}u_f = \tau_{f,u} \\
&m_{22}\dot{v}_f + m_{11}u_f r_f + d_{22}u_f = 0 \\
&m_{33}\dot{r}_f + (m_{22} - m_{11})u_f v_f + d_{33}r_l = \tau_{f,r}
\end{aligned}
\tag{3.32}
$$

Here, each term is included in the equation

$$
m_{11} = m - X_{\dot{u}}\ ,\ m_{22} = m - Y_{\dot{v}}\ ,\ m_{33} = I_z - N_{\dot{r}}
$$

$$
d_{11} = -X_u - X_{u|u|}|u|\ ,\ d_{22} = -Y_v - Y_{v|v|}|v|\ ,\ d_{33} = -N_r - N_{r|r|}|r|
$$

The error of v_f^v in equation (3.30) is $v_e = v_f - v_f^v$. After differentiating it, substituting equation (3.32) yields the following equation.

$$
\begin{aligned}
\dot{v}_e &= \dot{v}_f - \dot{v}_f^v \\
&= -\frac{d_{22}}{m_{22}}v_f - \frac{m_{11}}{m_{22}}k_1\epsilon_1 r_f + \frac{m_{11}}{m_{22}}\zeta_1 \cos e_\psi r_f \\
&= -\frac{m_{11}}{m_{22}}\zeta_2 \sin e_\psi r_f + k_2 v_f - k_2\zeta_1 \sin e_\psi \\
&= -k_2\zeta_2 \cos e_\psi - k_2\epsilon_1 r_f - \dot{\zeta}_1 sine_\psi - \dot{\zeta}_2 cose_\psi \\
&= -\zeta_1 \cos e_\psi \dot{e}_\psi + \zeta_2 \sin e_\psi \dot{e}_\psi
\end{aligned}
\tag{3.33}
$$

If the constant is $k_1 = d_{22}/m_{11}$, $k_2 = d_{22}/m_{22}$ equation (3.33) can be

summarized as follows.

$$\dot{v_e} = \left(\frac{m_{11}}{m_{22}} - 1 \right) (\zeta_2 \sin e_\psi - \zeta_1 \cos e_\psi) r_f \tag{3.34}$$

$$- \frac{d_{22}}{m_{22}} (\zeta_1 \sin e_\psi + \zeta_2 \cos e_\psi)$$

$$+ (\zeta_2 \sin e_\psi - \zeta_1 \cos e_\psi) r_l - \dot{\zeta}_1 sine_\psi - \dot{\zeta}_2 cose_\psi$$

To obtain virtual control, we can define the Lyapunov function as follows.

$$V_2 = \frac{1}{2} v_e^2 + 2k_3 \sin^2 \left(\frac{e_\psi}{2} \right), \; k_3 > 0 \in \mathbb{R} \tag{3.35}$$

Then, we can obtain virtual control that has derivative value less than 0 after differentiating it as shown in equation (3.36).

$$r_f^v = r_l + k_4 \sin e_\psi - k_5 \left(\frac{m_{11}}{m_{22}} - 1 \right) v_e \lambda + \Theta \tag{3.36}$$

where, $\lambda = \zeta_2 \sin e_\psi - \zeta_1 \cos e_\psi$, $\kappa = \zeta_1 \sin e_\psi + \zeta_2 \cos e_\psi$

$$\Theta = - sgn(v_e) \frac{[(k_4 + k_3 k_5) \parallel m_{11}/m_{22} - 1 \parallel + d_{22}/m_{22}] \parallel \kappa \parallel}{\parallel m_{11}/m_{22} - 1 \parallel \parallel \kappa \parallel + k_3}$$

3.3.2.2 Dynamics Controls

In an unmanned submersible, the actual control input is the thrust of the thruster. Therefore, virtual control q and w derived above should be designed by using kinematic and dynamic models of the UUV. First, velocity error in the surge direction is defined. Then the Lyapunov function is defined as shown in equation (3.36) It is then differentiated as follows.

$$V_3 = \frac{1}{2}u_e^2 \tag{3.37}$$

$$\dot{V}_3 = u_e\left(\left(\frac{m_{22}}{m_{11}}v_f r_f - \frac{d_{11}}{m_{11}}u_f + \left(\frac{1}{m_{11}}\right)\tau_{f,u} - \dot{u}_f^v\right)\right.$$

Therefore, the value of q having a negative value given by equation (3.38) is a control input for speed control in the surge direction.

$$\tau_{f,u} = m_{11}\left(-k_6 u_e - \frac{m_{22}}{m_{11}}v_f r_f + \frac{d_{11}}{m_{11}}u_f + \dot{u}_f^v\right)\ ,\ \ k_6 > 0 \in \mathbb{R} \tag{3.38}$$

In order to control error $r_e = r_f - r_f^v$ of the angular velocity, the Lyapunov function $V_4 = (1/2)r_e^2$ is defined. When the derivative value of the function is smaller than 0, the control input for controlling the angular velocity finally is as shown in the following equation (3.39).

$$\tau_{f,r} = m_{33}\left(-k_7 r_e - \frac{m_{11} - m_{22}}{m_{33}}u_f v_f + \frac{d_{33}}{m_{33}}r_f + \dot{r}_f^v\right) \tag{3.39}$$

4. Dynamic Simulation of Combined Unmanned Ocean Vehicle

In order to accomplish desired work of a combined unmanned ocean vehicle, it is necessary to adopt the induction rule to follow a preset trajectory or way-point. Also, it is necessary to design the controller to achieve target performance of the platform in an environment where there is model uncertainty or disturbance. Therefore, in the previous chapter, we designed guidance law and controller of a combined unmanned ocean vehicle.

In order to confirm the designed guidance law and the performance of the controller before field test, we tried to confirm it through dynamics simulation. The simulator was developed using Matlab & Simulink and numerical analysis was performed using the Runge-Kutta method. Fig. 4-1 shows a simulation flow diagram of a combined unmanned ocean vehicle. First, the speed and position obtained from the dynamics model of the USV and the UUV are set to initial values of the first and last nodes of the cable. The cable uses the given initial values to calculate the force acting on each node of the cable. Finally the force generated at the last node connected to the UUV is calculated. The calculated force is used as disturbance value of the UUV. During way-point tracking, the calculation as described above is repeatedly performed.

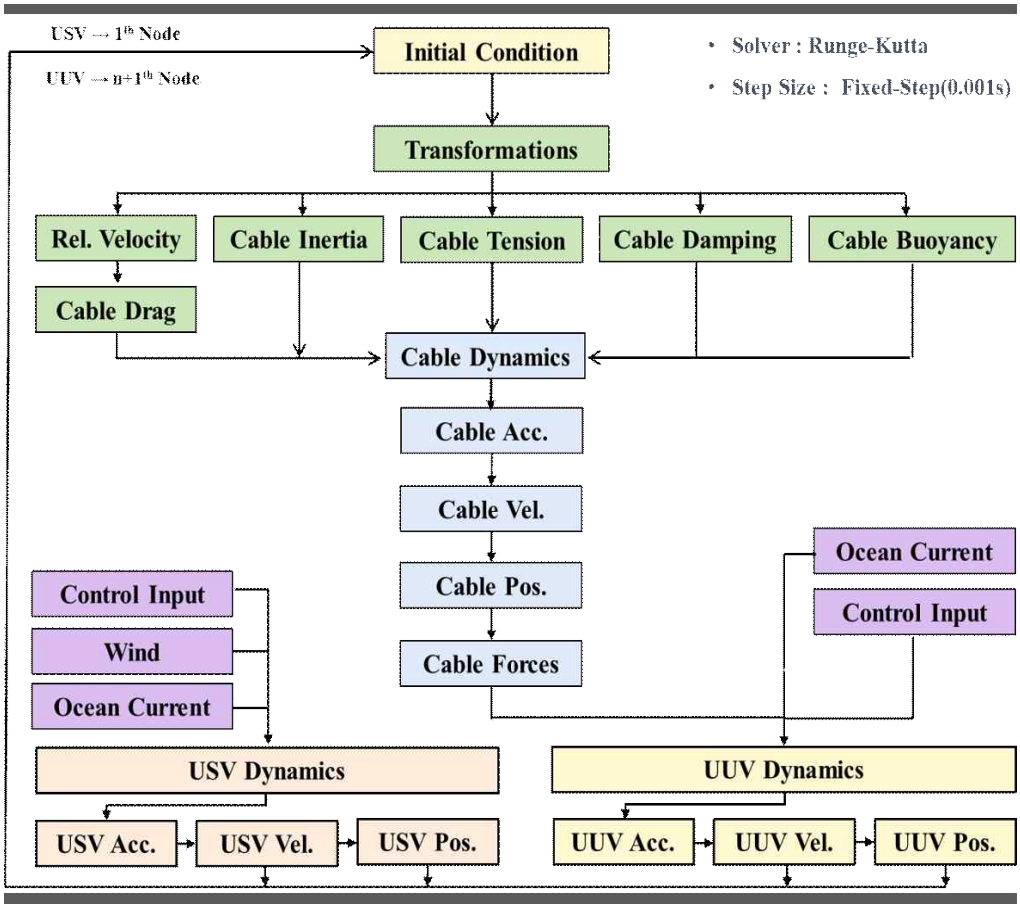

Fig. 4-1 Flow chart of Dynamics Simulation

The first simulation was performed to confirm the depth direction movement of the UUV during straight running of the combined unmanned ocean vehicle. A UUV without a thruster for controlling the depth direction should maintain water depth using negative buoyancy. Therefore, in this study, it was assumed that the movement in the depth direction of the UUV would be unstable when there was speed difference between the USV and the UUV. Simulations were conducted to determine if this assumption was valid. In the simulation, the initial UUV was located 3 m below the waterline. The cable was divided into

20 segments to calculate the force.

As shown in Fig. 4-2, and Fig. 4-3 below, when the speed of the USV was faster than that of the UUV, the UUV moved in the form of being pulled as shown in Fig. 4-3. Fig. 4-4 shows simulation results for the case where the UUV and the USV travelled at similar speeds. Unlike the previous simulation, it was seen that the variation of the depth was small. It then decreased again.

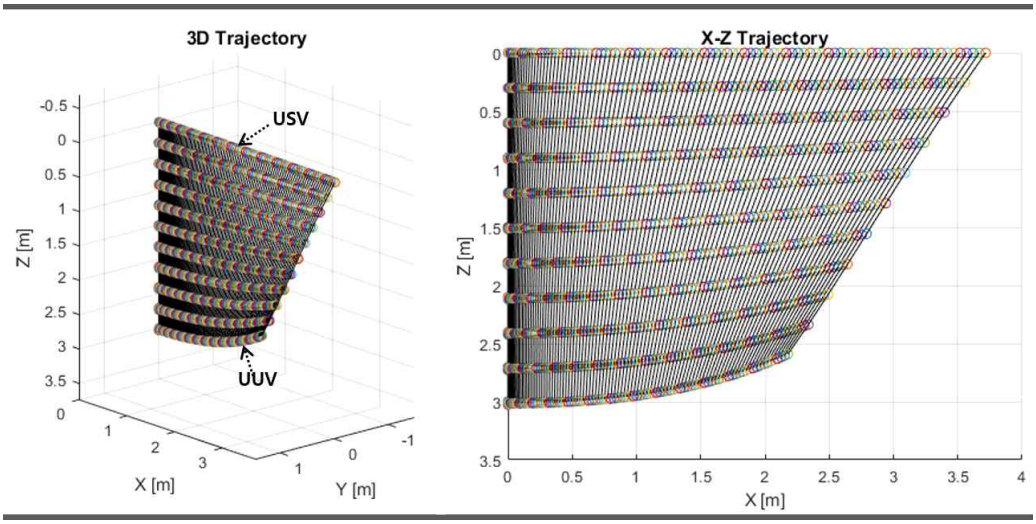

Fig. 4-2 Straight Motion of the combined unmanned ocean vehicle (USV : 0.5m/s, UUV : 0.27m/s)

According to simulation results, in order to maintain depth of the UUV during operation of the combined unmanned ocean vehicle, speed difference between the USV and the UUV should not be large. In addition, it was confirmed that motion of the UUV would be unstable due to speed difference between the USV and the UUV.

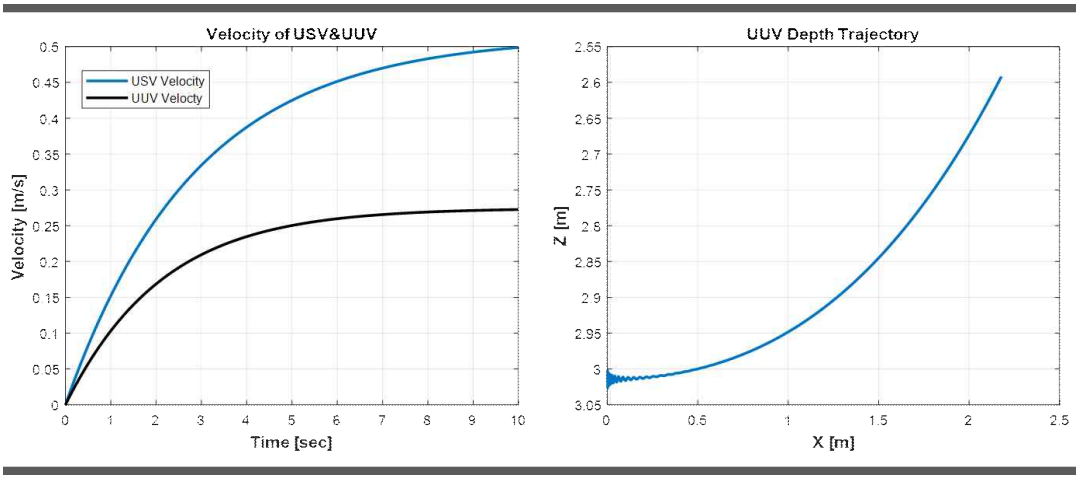

Fig. 4-3 Velocity of the USV&UUV and Depth Value of the UUV (1)

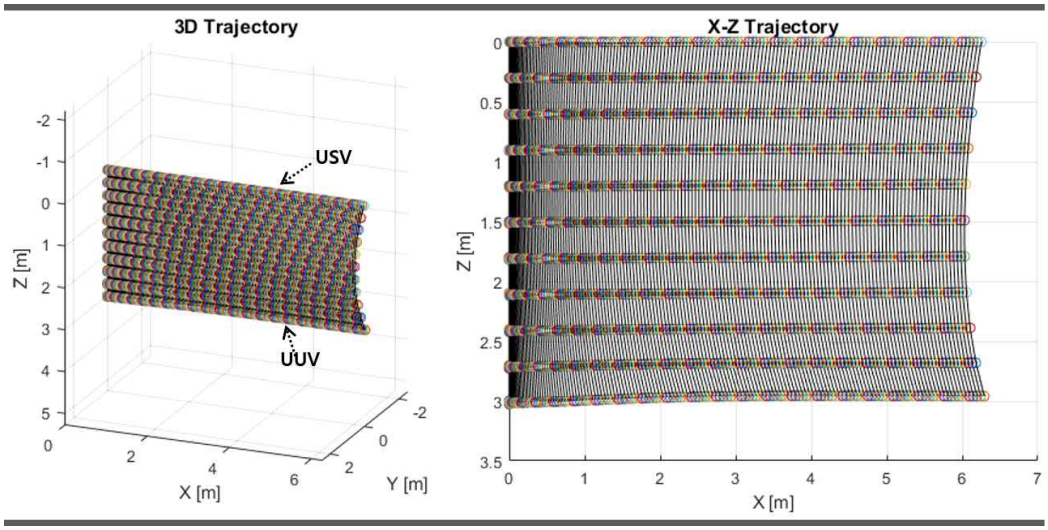

Fig. 4-4 Straight Motion of the combined unmanned ocean vehicle (USV : 0.5m/s, UUV : 0.48m/s)

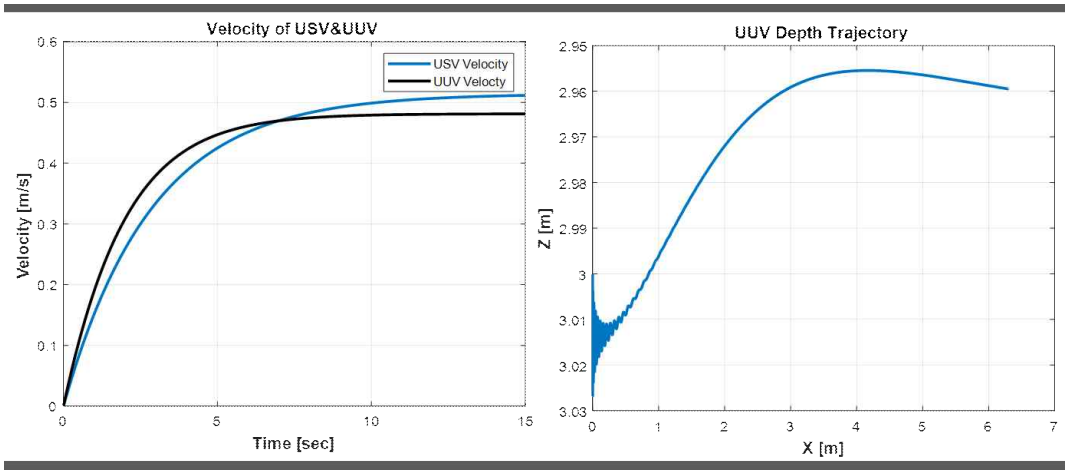

Fig. 4-5 Velocity of the USV&UUV and Depth Value of the UUV (2)

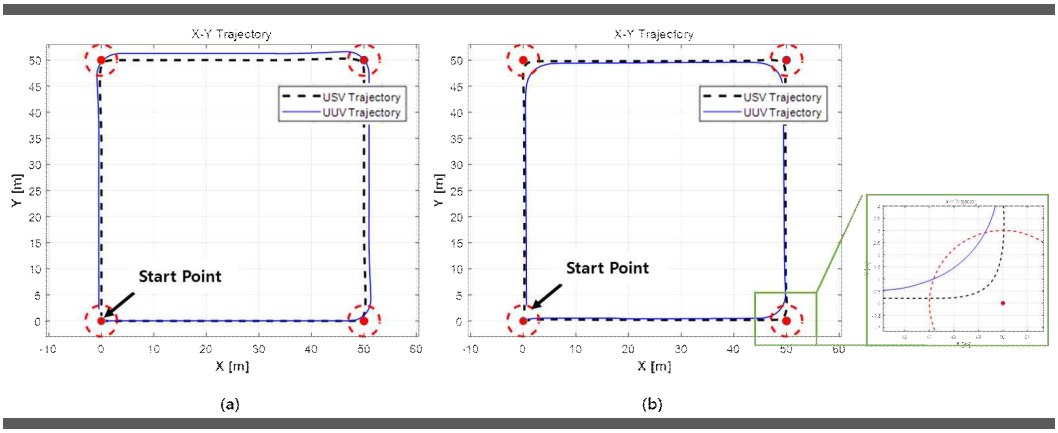

Fig. 4-6 Way-Point Tracking Simulation No.1

Figure 4-6 shows simulation results to confirm validity of the guidance law for path following USV. The way-point was (0,0), (50,0), (50, 50), and (0, 50) so that the route follow-up performance could be confirmed for straight and turning motions. As a result, we could follow the given way-point according to the designed guidance law. In Figure 4-6 (a), the UUV should follow the only relative angle of the USV. As can be seen from the graph, the USV and the

UUV moved at a constant distance. In the case of an actual platform, the movement of the UUV was restrained according to the length of the underwater cable. Force on the cable can be large. Therefore, as shown in Fig. 4-6 (b), it was confirmed that the target direction angle for moving to the center of the USV simultaneously with the relative direction angle was controlled to reduce error of the relative distance to follow the path.

Finally, simulations were carried out with the combined unmanned ocean vehicle. To verify performance of the controller, we applied an anti-windup PID controller and a back-stepping controller. Fig. 4-7 shows three-dimensional path of a combined unmanned ocean vehicle moving through a given way-point. The figure between the USV and the UUV represents elements of the cable. The length of the cable was set to be 3 m based on the depth of the yacht moorings in front of the Korea Maritime and Ocean University where the actual experiment was performed. Passing points were set as (0,0), (10,10), and (20,5).

Fig. 4-8 shows a two-dimensional trajectory of a combined unmanned ocean vehicle. In Fig. 4-8 (b), the UUV seems to follow the path of the USV in straight-ahead driving. However, when comparing the turning or the finally reached distance, the backstepping controller was more stable. In the case of backstepping, since it is robust against disturbance, it ignores the influence of disturbance generated in underwater cable. It can follow the relative direction angle well. On the other hand, the PID controller was unable to control the UUV. This was because both the relative angle and desired angle for moving to the center of the UUV were performed at the same time. In other words, it is possible to control two control objects using one thrust, although it is difficult to achieve perfect performance.

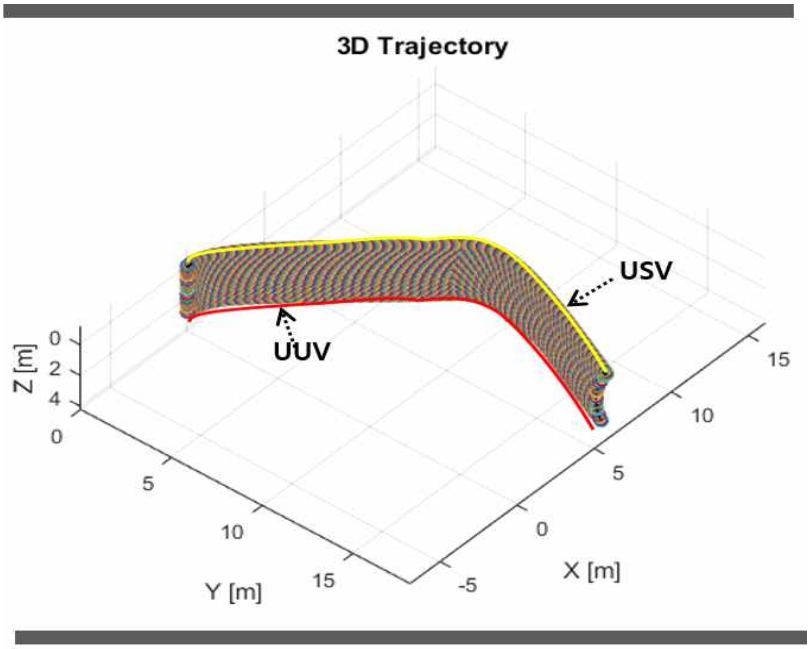

Fig. 4-7 3D Trajectory of combined unmanned ocean vehicle

Fig. 4-9 shows translational and rotational speeds for X, Y, and Z axes of the combined unmanned ocean vehicle. The forward target speed in the X-axis direction was 0.6m/s, and the vehicle followed this well. It was confirmed that the PID controller converged to a value slightly smaller than 0.6 m/s although there was not much different depending on the controller.

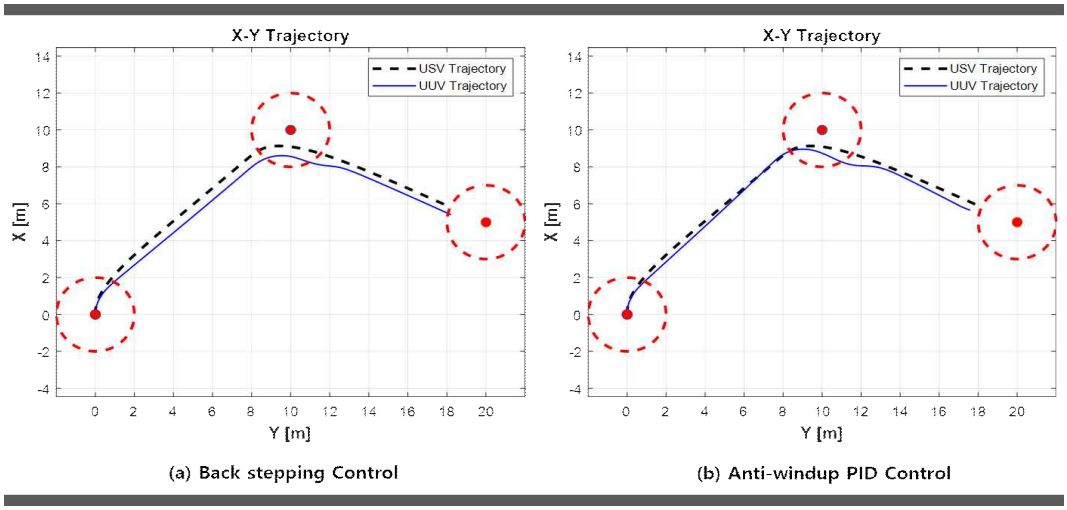

Fig. 4-8 2D Trajectory of combined unmanned ocean vehicle

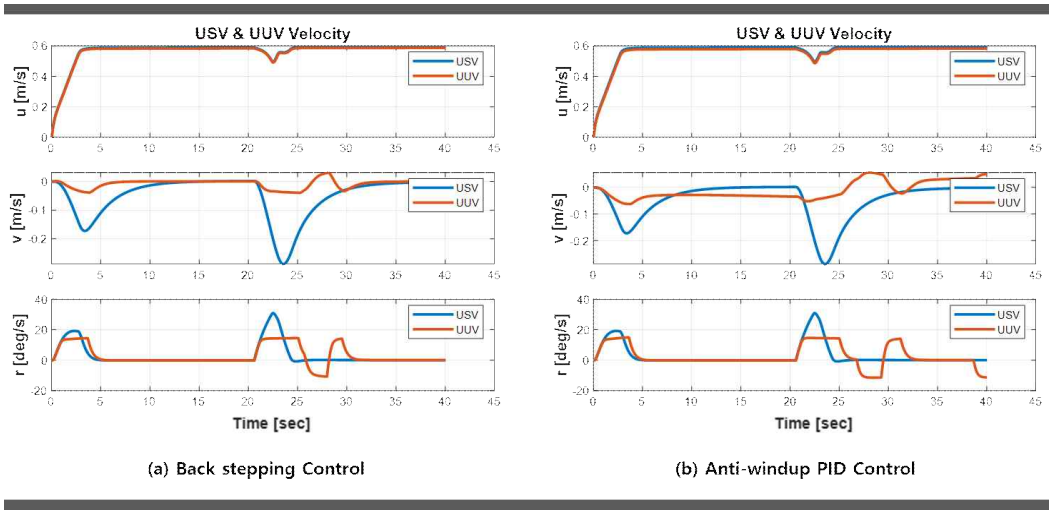

Fig. 4-9 Velocity of each axes of the combined unmanned ocean vehicle.

Figs. 4-10 and 4-11 show thrust forces of the USV and the UUV. Subscripts L and R represent left and right propellers, respectively. F represents a front propulsion unit mounted on a UUV.

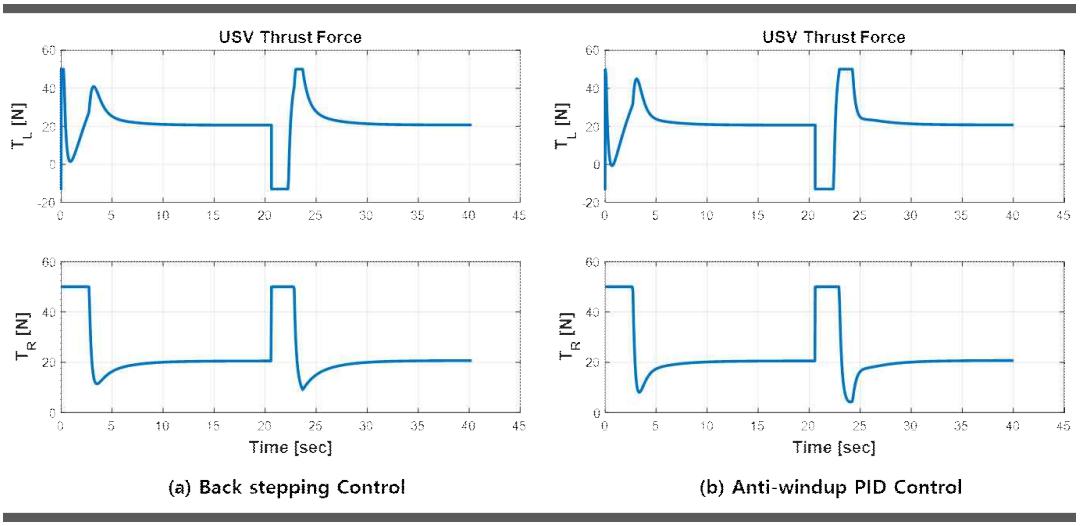

Fig. 4-10 Thrust forces of the USV

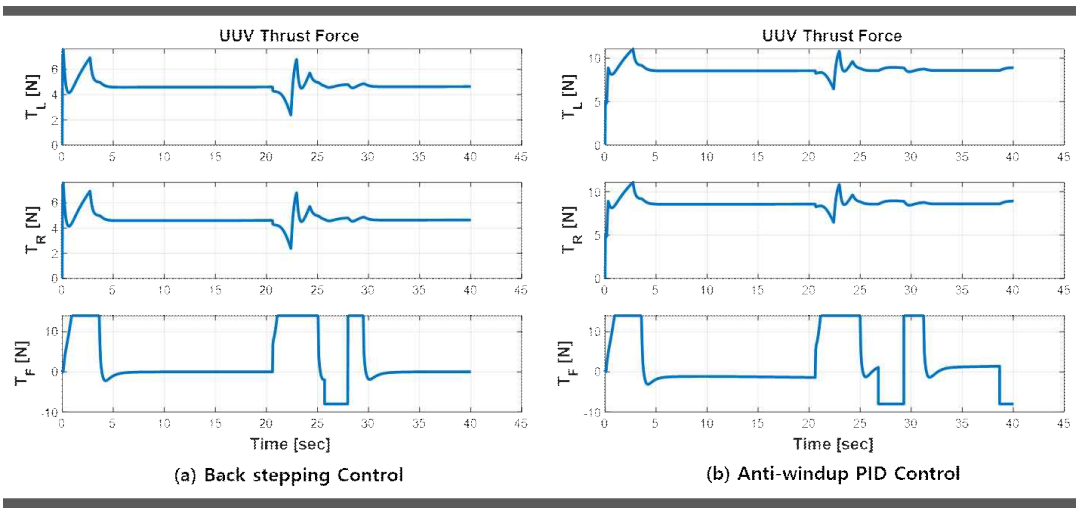

Fig. 4-11 Thrust forces of the UUV

Figs. 4-12 and 4-13 show heading angles of the USV and the UUV. The red dotted line in the graph represents target heading angle calculated through the path-following algorithm and the target heading angle of the UUV that follows the USV. In the case of the PID controller, slight overshoot occurred. However, it followed the back-stepping controller which followed the target value well.

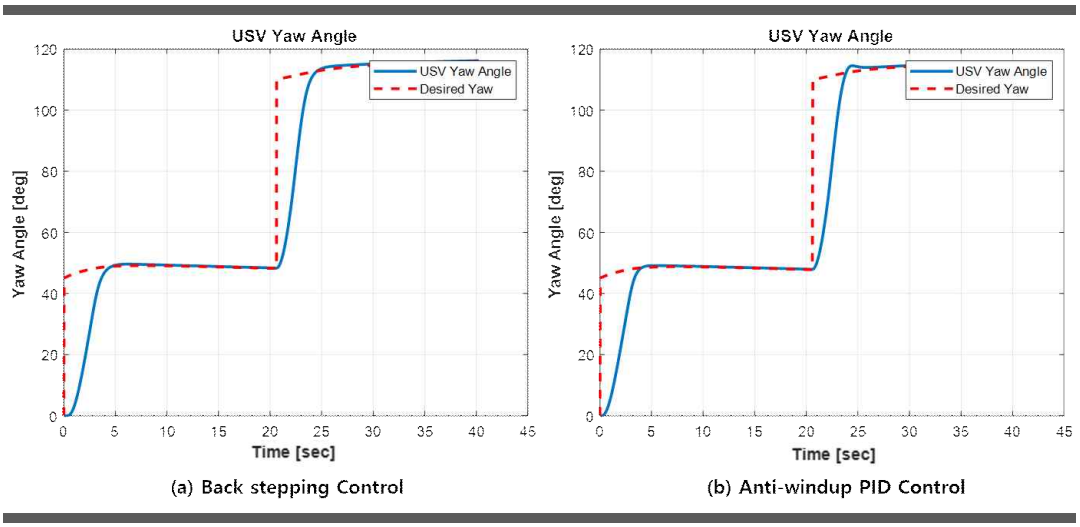

Fig. 4-12 Heading Angle of the USV

Fig. 4-13 shows heading angle of the UUV. At about 25 seconds, the desired heading angle changed and moved to the center of the USV. The backstepping controller also followed the changed target heading angle relatively faster than the PID controller.

Figure 4-14 shows depth of the UUV. The PID controller could not accurately follow the speed of the USV. Thus, the depth direction changed more than the backstepping controller. In addition, the UUV with backstepping after 30 seconds converged to about 2.77 m, although the PID controller changed in the depth direction.

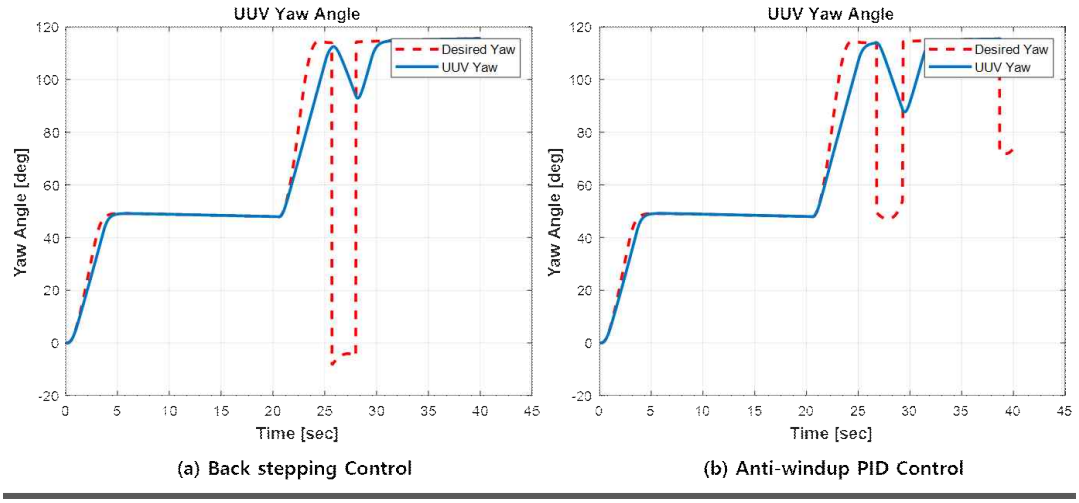

Fig. 4-13 Heading Angle of the UUV

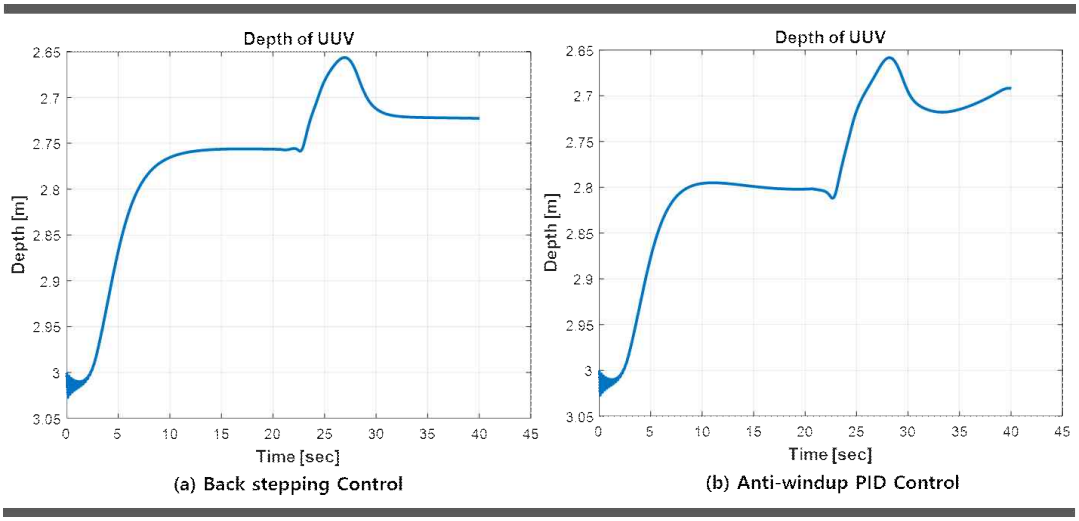

Fig. 4-14 Depth of the UUV

Fig. 4-15 shows relative distance between the USV and the UUV. When backstepping controller was applied, the relative distance increased while turning (about 25 ~ 30 seconds). It then moved while maintaining a distance of about

0.4 m. In the case of the PID controller, the change in the relative distance was large. It could not be stabilized.

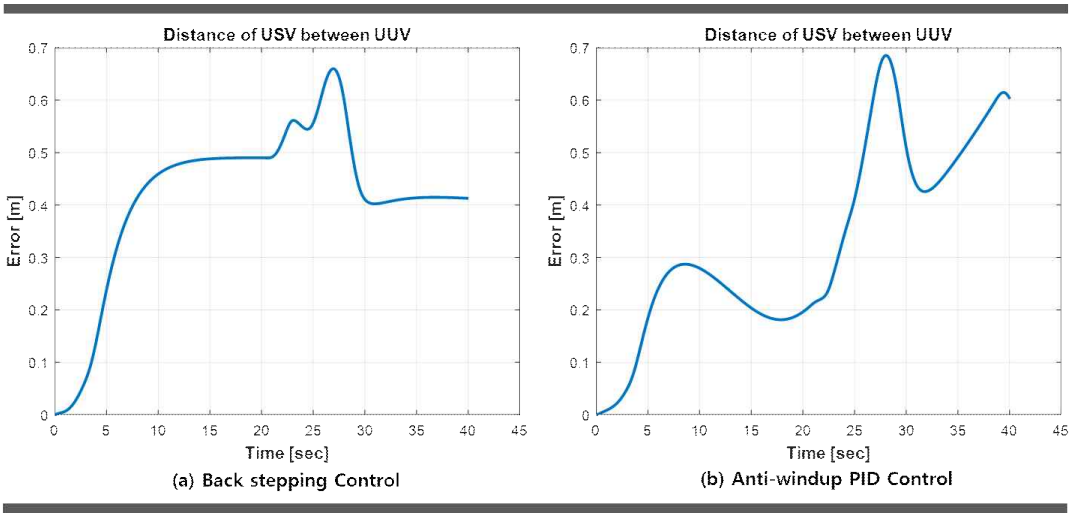

Fig. 4-15 Relative distance of USV and UUV

5. Hardware System Configuration

This chapter introduces hardware configuration of the vehicle that is developed to verify the performance of the Guidance and Control of the combined unmanned ocean vehicle introduced in Chapter 3. The developed vehicle is divided into a USV and a UUV. This chapter describes specifications, configuration, mounting equipment, control system, and communication method of each platform. Detailed information on sensors mounted on each platform is shown in Appendix B.

5.1 Hardware Configuration of USV

The USV developed in this study is shown in Fig. 5-1 below. As can be seen in the figure, the hull was designed using commercial rubber boats and the upper part was equipped with equipment necessary for platform operation such as a winch system and a control system. In addition, two thrusters were installed on the stern of the USV for position and heading angle control. A guide was installed at the bottom to prevent collision of the UUV and to stabilize docking. Table 5-1 below shows specifications of the USV and the mounting equipment.

Fig. 5-1 Shape of the USV

Table 5-1 Specification of the USV

Size (L × W × H)	3.00×1.62×0.47 (m)
Battery	Li-Po / 24V 400A
Thruster	Minn Kota (2ea)
GPS	Hemisphere H200
AHRS	Xsens MTi-30
AP Bridge	GT-Wave
Controller	CY8CKIT-059 PSoC (2ea)

The USV should be equipped with a launch and recovery system for docking and controlling the depth of the UUV. The Gantry, Overhead, A-frame, Knuckle, and Moonpool handing unit are applied as shown in Figure 5-2 below. Each system is designed considering the shape and size of the towed vehicle, the connecting position of the tow cable, and the operating environment. For example, the Gantry type is mainly used to connect a towed cable to the front

of the towed vehicle. It is often used for a small USV with a small space restriction. However, the towed vehicle is usually limited to a small torpedo type.

Fig. 5-2 Launch & Recovery System

In this study, the system was designed and manufactured to enable USV of limited size to be installed and recovered from under the hull as shown in Figure 5-3.

Fig. 5-3 Winch System of combined unmanned ocean vehicle

Components of the installed launch and recovery system are shown in Figure 5-4 below. Specifications are shown in Table 5-2. The diameter of the drum of the winch was designed considering the radius of curvature of the underwater cable. The motor was selected considering the weight of the UUV. The slip-ring was attached to the side of the winch drum to prevent twisting of the underwater cable.

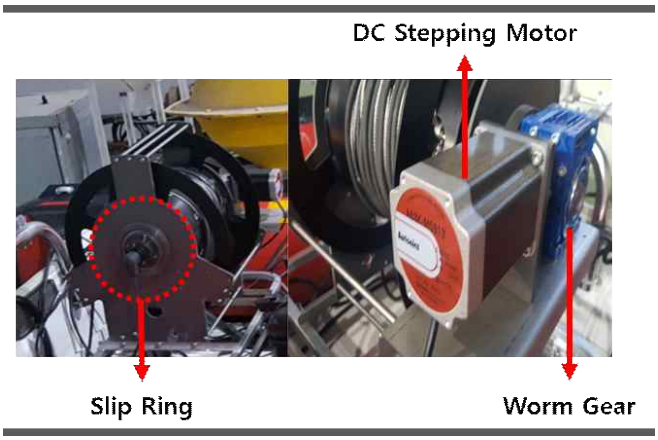

Fig. 5-4 Configuration of the winch system

Table 5-2 Specification of winch system

Stepping Motor	A63K-M5913
Max. Torque	6.3Nm
Current	1.4A/Phase
Motor Drive	MD5-ND14
Power	20~35VDC
Current consumption	Max. 3A
Setp Angle	0.72°/step

The electric system of the USV was divided into a power supply unit and a control unit. The power supply unit distributes the necessary voltage to the sensor and the UUV, a. An LC filter was designed in the input and output part of the power supply to supply stable power.

The controller was designed to acquire data from each sensor using two MCUs (PSoC). It could perform data processing and platform control. Figure 5-3 shows the electric system of the USV designed and constructed.

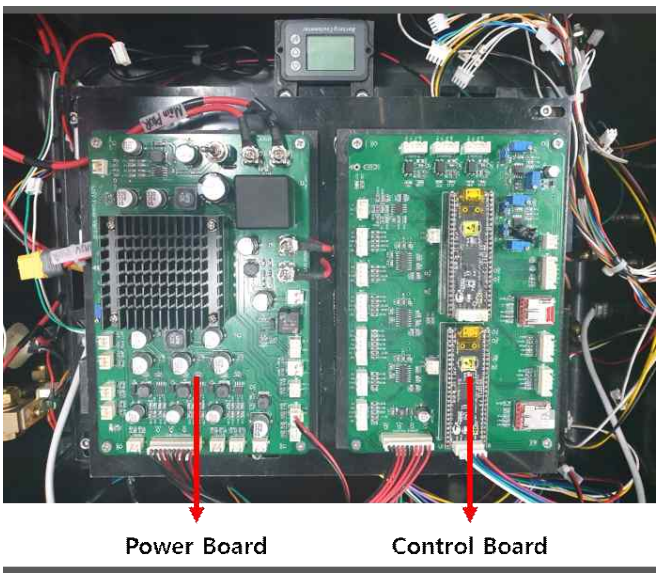

Fig. 5-3 Electric system of the USV

The combined unmanned ocean vehicle developed in this study needs to receive mission orders from the operator and then transmit data obtained from sensors of USV and UUV in real-time to operators on land. For this purpose, GOT's GT-Wave AP bridge was installed so that data could be transmitted and received. This equipment is a high-speed wireless bridge with a fast transmission speed of 876 Mbps in the wireless network area that can realize a data

transmission rate of 360 Mbps. Table 5-3 below shows specifications of GT-Wave860, the wireless communication equipment.

Table 5-3 Specification of the wireless communication equipment

Frequency	2.4~2.485GHz
Speed	Max. 867Mbps (80MHz)
Bandwidth	20/40/80 MHz
Power	DC 24V
Size	270 × 270 × 80(mm)

5.2 Hardware Configuration of the UUV

The UUV plays a role in terrain surveillance using multi-beam sonar and underwater object recognition using a camera. The UUV developed in this study is shown in Figure 5-4 below. Its specifications are shown in Table 5-4 below.

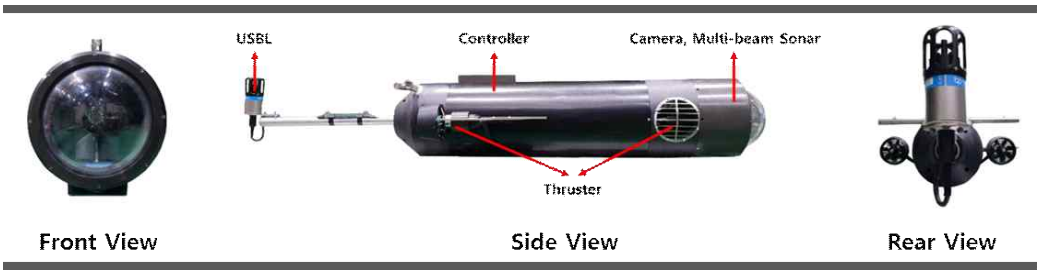

Fig. 5-4 Shape of the UUV

Table 5-4 Specification of the UUV

Size (L × W × H)	1.79 × 0.25 × 0.25 (m)
Weight (in air / in water)	36kgf / 15kgf
Multi-beam sonar	Oculus M750
Analog Camera	SK-2102N
Depth Sensor	Sensys PSC
AHRS	Xsens MTi-30
Thruster	Technadyne Model 300
Controller	CY8CKIT-059 PSoC (2ea)

The hull of the UUV has a torpedo shape. A multi-beam sonar and a camera are installed in front of the hull to detect a submarine topography or a target object in water. The stern is equipped with a USBL sensor which is designed to measure USV and relative positions. The pressure container is waterproofed by O-ring. The outside of the container and various brackets are corroded through anodizing. The electric system of the UUV is designed to be stackable due to space limitations of the pressure container as shown in Fig. 5-5 below.

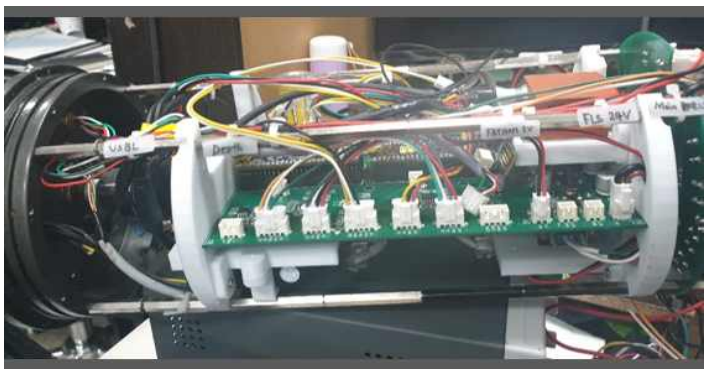

Fig. 5-5 Electric system of the UUV

The UUV has negative buoyancy in water. It is possible to control the depth together with the winch system. The motion on the horizontal plane (X-Y plane) is designed to be controllable using two propellers mounted on the stern and a propeller mounted on the front of the hull. Fig. 5-6 shows how to connect a UUV with an underwater cable. The steel wire was used to connect three points before and after the hull. This method minimizes roll and pitch movements of the UUV. It also minimizes tension on the underwater cable.

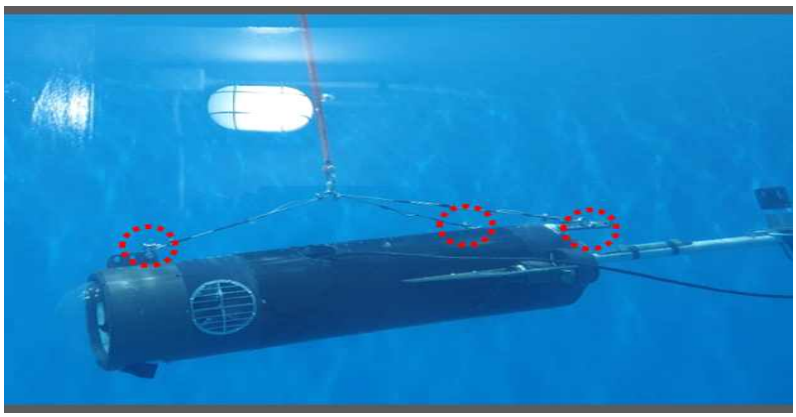

Fig. 5-6 UUV and Underwater Cable connection method

5.3 Configuration of the Control System

The control system of the combined unmanned ocean vehicle is classified into a system that can exchange information necessary for control through communication between the control system and the platform of USV and UUV. Fig. 5-7 below shows control system's configuration of the combined unmanned ocean vehicle. Characteristics of each sensor and equipment mounted on the platform are shown in Appendix B.

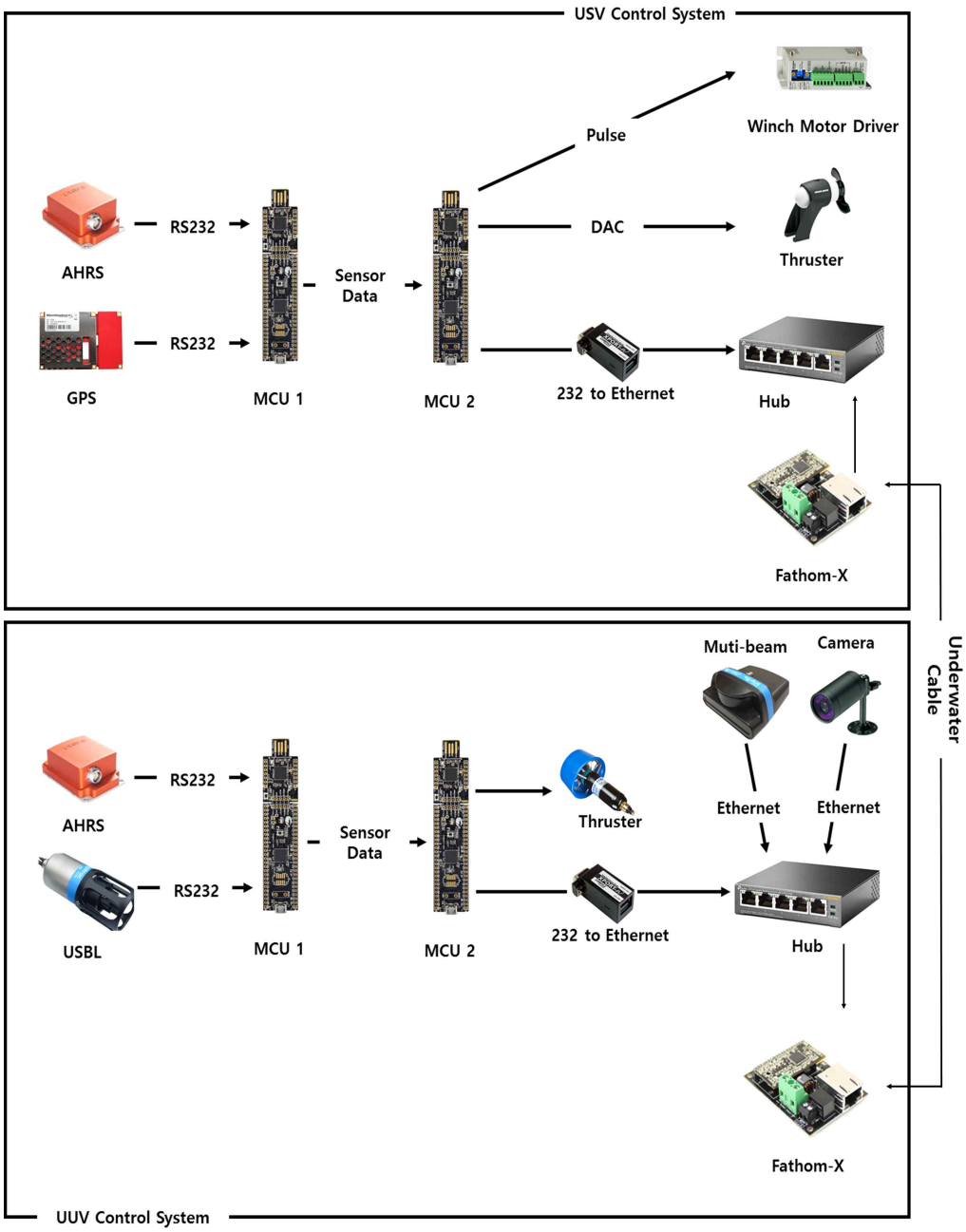

Fig. 5-7 Control System configuration diagram

In the case of MCU 1, it acquires sensor data followed by filtering. MCU 2 receives data from the MCU 1 and takes charge of calculation and driving unit output necessary for control. MCU2 is also designed to communicate data between USV and UUV using underwater cable. Communication using the underwater cable was made by using Fathom-X equipment to reduce 4-wire Ethernet to 2 lines.

Fig. 5-8 shows data exchanged between an onshore operator and the combined unmanned ocean vehicle. The operator can set remote control mode and autonomous mode. The operator can also transmit control gain adjustment and emergency stop command. The USV transmits information about the command received from the operator to the UUV. The UUV provides depth information for winch control. Each platform is also configured a communication system to transmit attitude and location information to the operator.

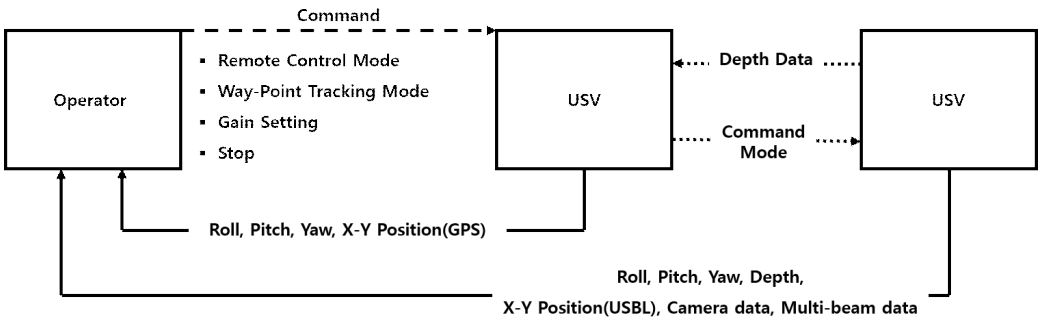

Fig. 5-8 Communication System configuration diagram

5.4 Operate System

For operation of the combined unmanned ocean vehicle, an operation console was designed and manufactured. The operation system as designed using Labview. Figures 5-9 and 5-10 below show front panel of the operator console and control program produced.

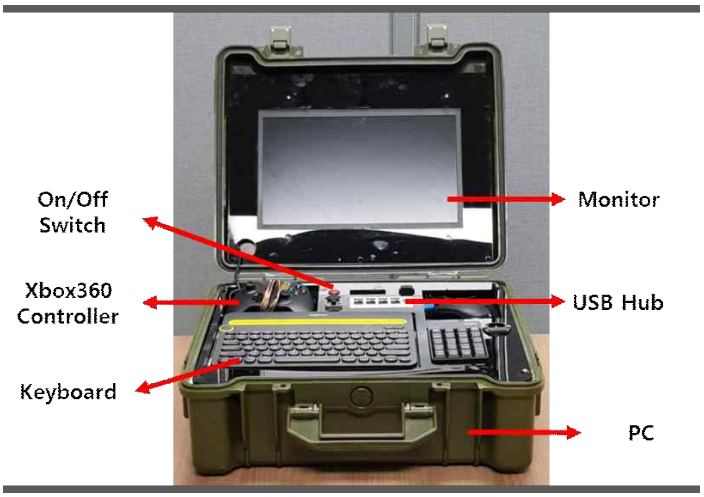

Fig. 5-9 Operation Console

The operating console is equipped with a commercial PC, a radio control unit, a monitor, and a keyboard for operating the platform. In addition, a plastic box is used for easy movement during operation and an inner bracket is made lightly using acrylic.

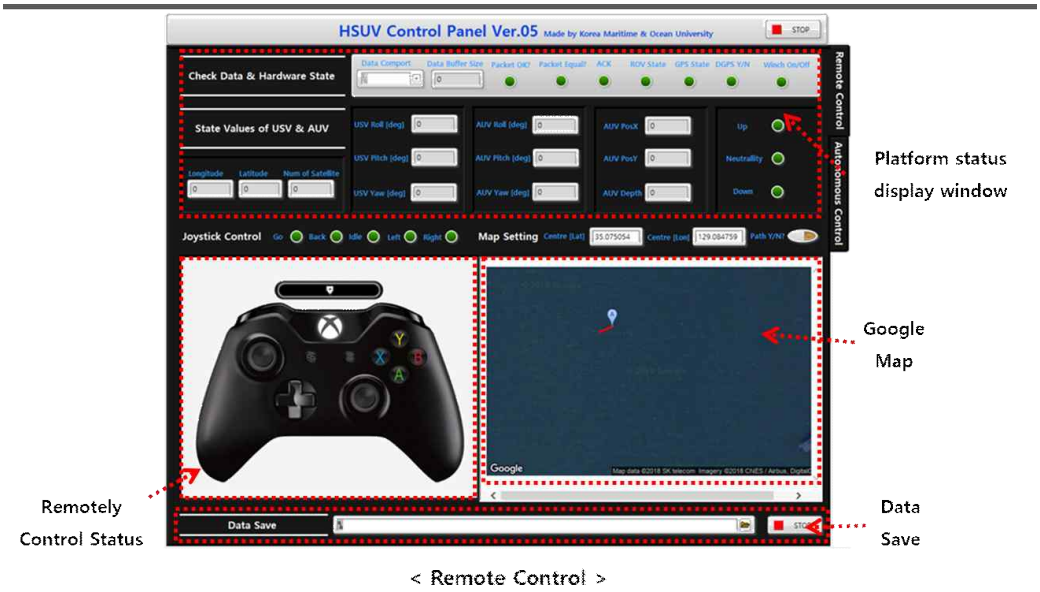

< Remote Control >

Fig. 5-10 Control Program for Remotely control

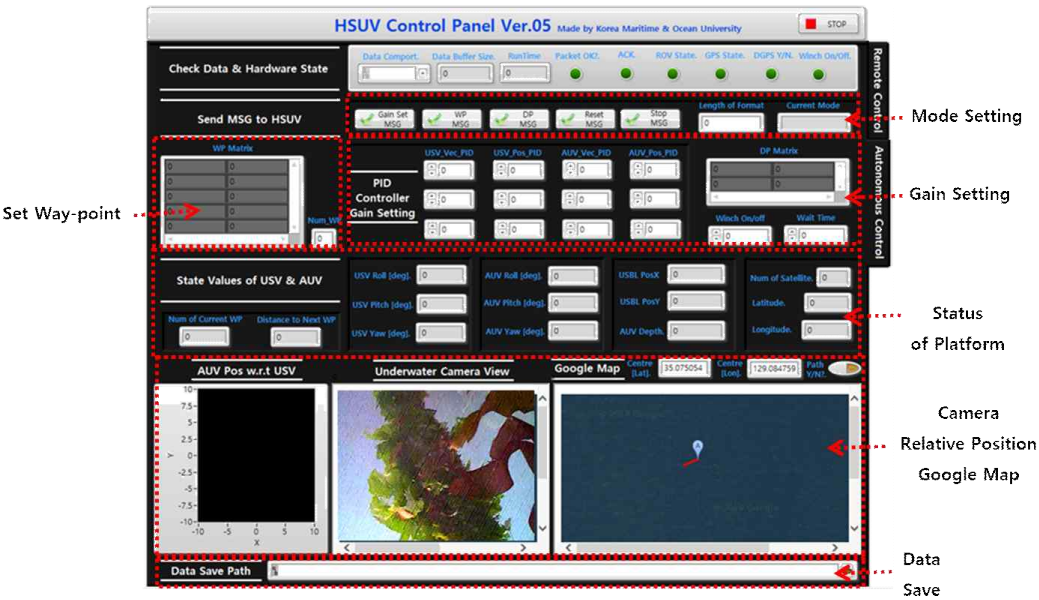

< Autonomous Control >

Fig. 5-11 Control Program for Autonomous control

The operation program is divided into remote control mode and autonomous control mode. It displays attitude information and position information of the combined unmanned ocean vehicle. The position information is expressed in Google Map using latitude/longitude. It also shows the status of data communication between the platform and the operation console. Failure of sensor can also be determined.

6. Sensor performance and Field test of combined unmanned ocean vehicle

6.1 Sensor Test

As can be seen from hardware configuration shown in Chapter 5, the combined unmanned ocean vehicle is equipped with sensors for measuring the position and direction. The performance of the sensor was tested to determine the meaning of information output from the sensor. Experiments of each sensor were carried out on a land or water tank. Table 6-1 below shows output value and coordinate system of each sensor. It can be seen that the output coordinate system of GPS, Attitude Heading Reference System(AHRS), and USBL is the same as the North-East-Down(NED) coordinate system. Therefore, it is unnecessary to work on the coordinate system of the sensor for separate rotation. Only the offset is applied to the position where each sensor is mounted.

6.1.1 GPS & AHRS

H200 model of Hemisphere was used for GPS and XSens MTi-30 was used

for AHRS. The experiment was carried out within Korea Maritime and Ocean University. Measured GPS data did not have any filter or correction. AHRS used peripheral magnetic field correction filter provided by the AHRS sensor itself.

Table 6-1 Data Values & Output Coordinate from Navigation Sensor

Sensor	Output Values	Coordinate
GPS	Latitude, Longitude, Velocity, Heading Angle	NED
AHRS	Heading Angle, Roll Angle, Pitch Angle	NED
USBL	Relative distance, Relative angle, Relative depth	NED
Depth Sensor	Depth	Z axis

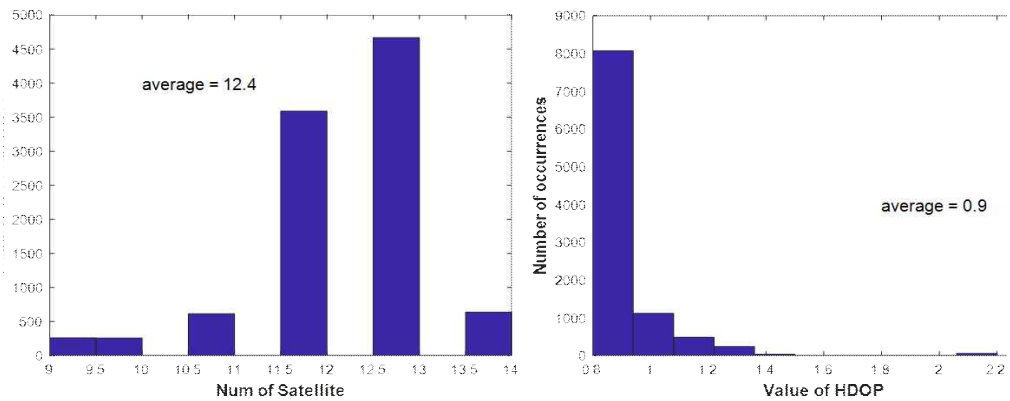

Fig. 6-1 Number of Satellite & HDOP from GPS sensor

Figure 6-1 shows the number of satellites and HDOP (horizontal dilution of precision) value as indicators of the accuracy of GPS sensor measured value. DOP (dilution of precision) is a dimensionless number that represents error of relative geometry of satellites in positioning. Generally, if HDOP value is less than 2, it can be said that the precision is very good. During the experiment, the average HDOP was 0.9 and the number of satellites was 12, showing a good reception ratio and a small measurement error.

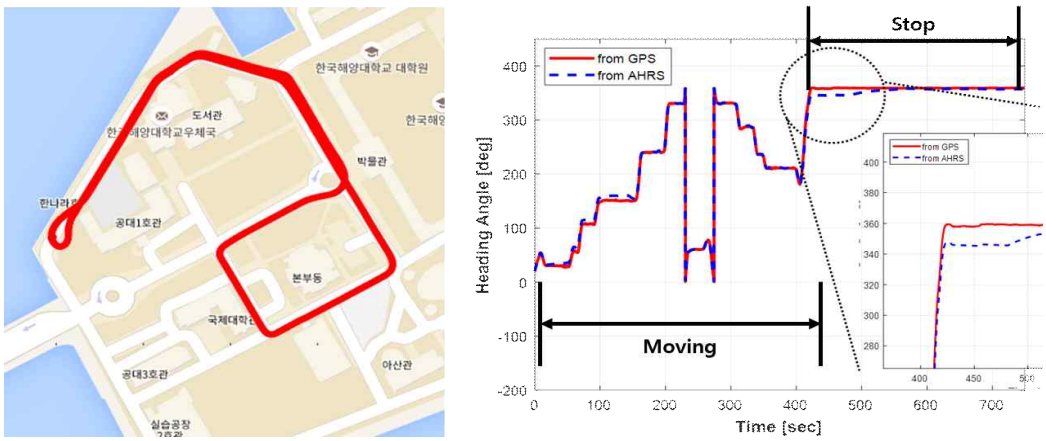

Fig. 6-2 Trajectory & Heading Angle

The left side of Figure 6-2 shows the actual traveled route using the GPS value and the right side of the figure shows directional angle measured by GPS and AHRS while moving. When the heading angle of the GPS with relatively high accuracy was regarded as a reference value, the AHRS value showed a tendency to change, although it had a slight deviation. It was confirmed that the directional follow-up was slow. The reason for this was that in the case of

AHRS, the average value of the surrounding magnetic field was calculated and operation of the filter was compensated in case of a change. It could be seen that GPS value became almost the same over time in the stop section. While moving, difference between the two sensors showed an average of 3.53 degrees and a standard deviation of 3.88 degrees.

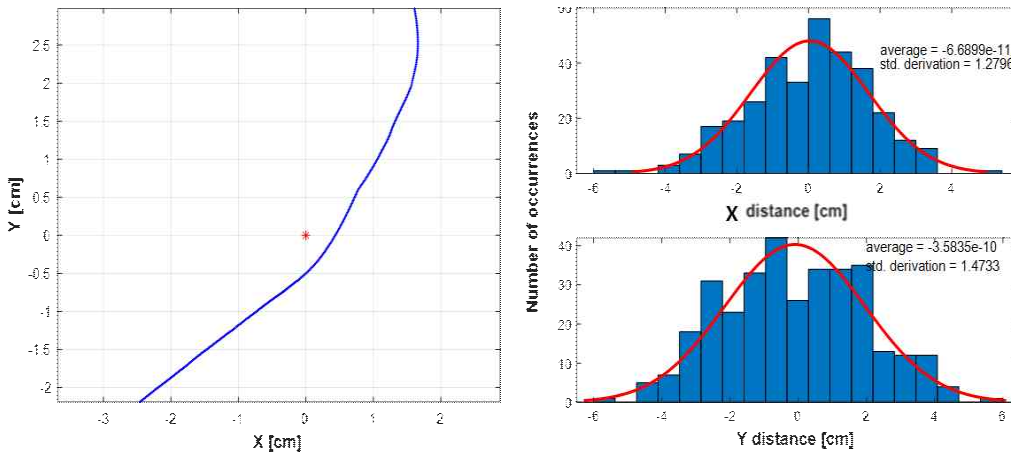

Fig. 6-3 Stationary position error & Histogram

Fig. 6-3 shows position error of the GPS when it is in the stop state in the right graph of Fig. 6-2. As shown in the graph, the position is very accurate in cm.

Fig. 6-4 shows heading angle error during movement. The maximum difference of error was 15 °. This was the value of the AHRS sensor was unstable while analyzing and reflecting the influence of the surrounding magnetic field.

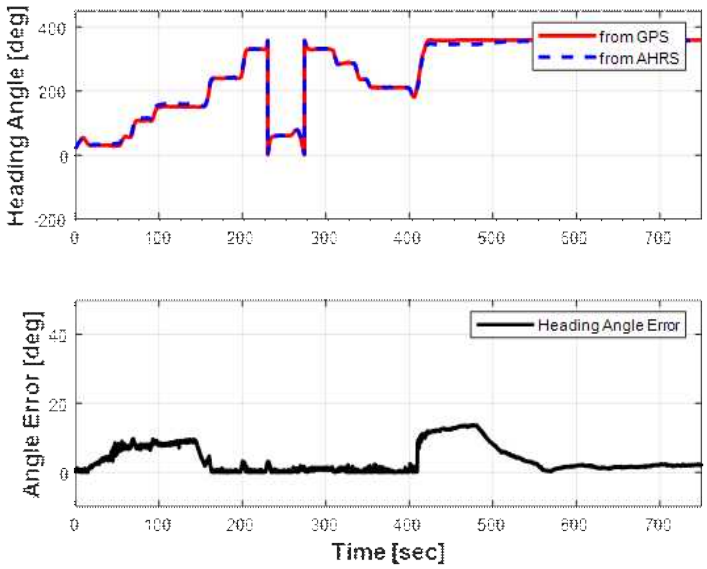

Fig. 6-4 Heading Angle Error while moving trajectory

6.1.2 USBL Sensor

The USBL sensor uses SeaTrac's X150 (Tranceiver) and X010 (Ponder) to measure relative positions of the USV and UUV. The USBL is used in the form so that the Ponder responds when the Tranceiver emits a signal. The distance value of the USBL sensor was confirmed to be output based on the NED coordinate system. The experiment was performed in an engineering tank to measure the sensor's accuracy. Figure 6-5 below shows the actual experiment performed.

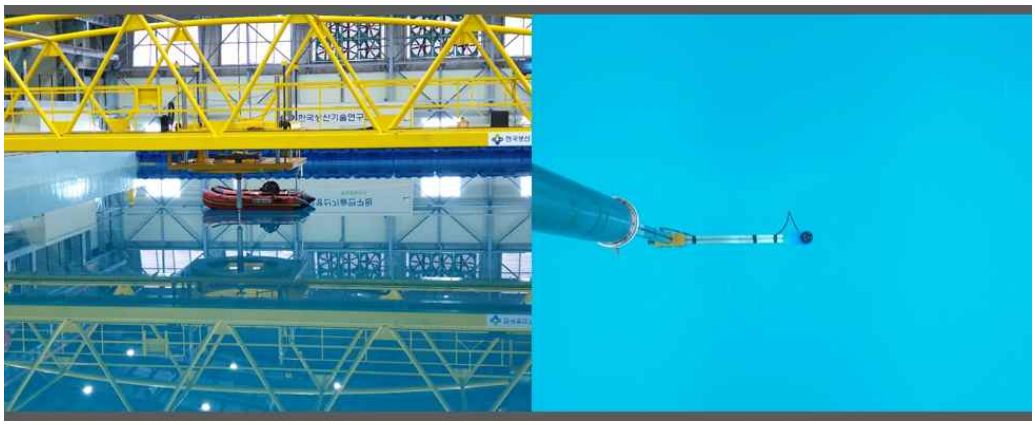

Fig. 6-5 USBL Sensor Test in water tank

The Ponder was installed at the initial reference position $(X, Y) = (2.4, 0.5)$ The position of Ponder was measured while moving the tranceiver along the axis. At this time, the relative depth of the Tranceiver and Ponder was measured to be constant at 0.8 m. Some results of the experiment are shown in Figures 6-7 to 6-10 below.

Experiment 1 and Experiment 2 showed output distance value of the USBL sensor in a static state. The average output value of the sensor was compared with that of the reference position. In Experiment 1, the error was 0.88 cm for the X axis and 2.12 cm for the Y axis. {Editor's Note: Please double check the highlighted area and make sure it reflects your intended meaning. The original one was unclear.} In Experiment 2, these errors were 10 cm and 16.50 cm, respectively. Such results suggest that the sound signal is not received well due to a short relative distance between the Tranceiver and the Ponder. {Editor's Note: Please double check the highlighted area and make sure it reflects your intended meaning. The original one was unclear.} In Experiment 3, results are plotted when the position of the Ponder is fixed while the Tranceiver is circling around.

In the graph, it can be confirmed that the data reception is not smooth when the distance is more than 4m on the X-axis.

As shown in the graph, data reception is not smooth when the distance is more than 4 m on the X-axis. This might result in data loss due to the relative water depth as described above. It was found that when the relative water depth was 0.8 m, it was unreliable, especially when the distance was more than 4 m from the reference position. However, considering the actual operation as shown in Figure 6-6, the relative depth was equal to the length of the cable. Even if the UUV performs pendulum movement, the unmanned submersible moves within 0.8 m. Therefore, valid information can be obtained from the USBL.

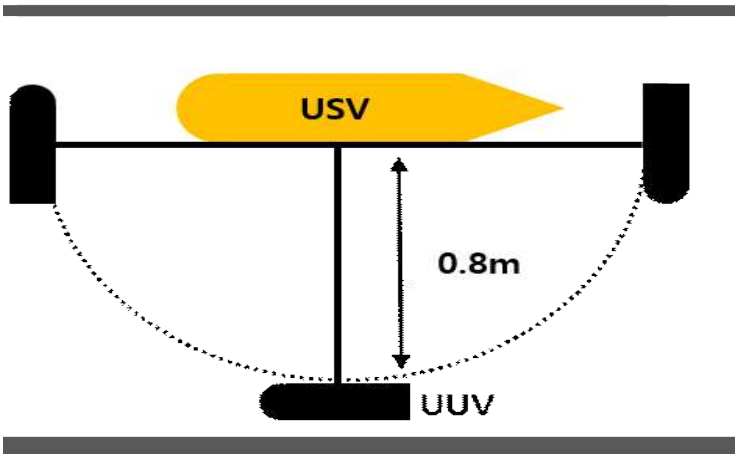

Fig. 6-6 Radius of the UUV according to underwater cable's length

Test No.1 – Reference Position (2.4, 0.5)

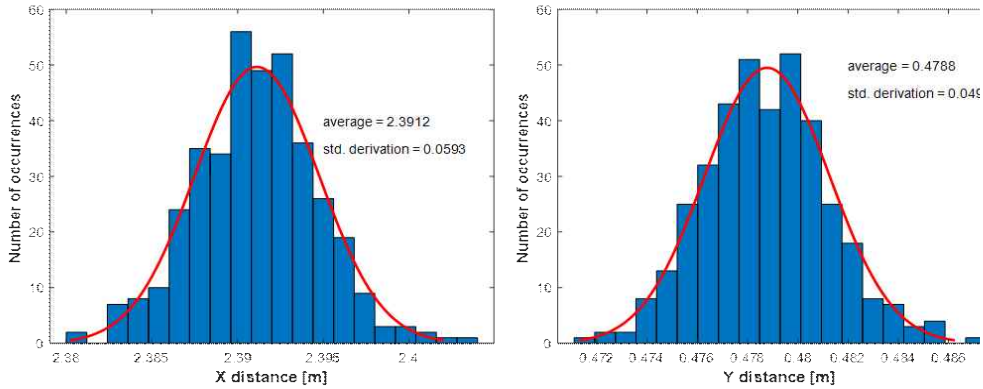

Fig. 6-7 Histogram of distance result from stationary test no.1

Test No.2 – Reference Position (4.4, 0.5)

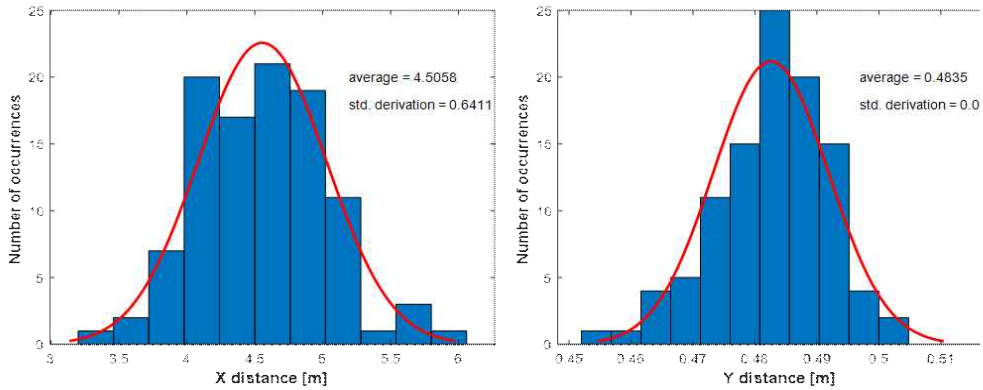

Fig. 6-8 Histogram of distance result from stationary test no.2

Test No.3 – Turning motion (2.4, 2.5)

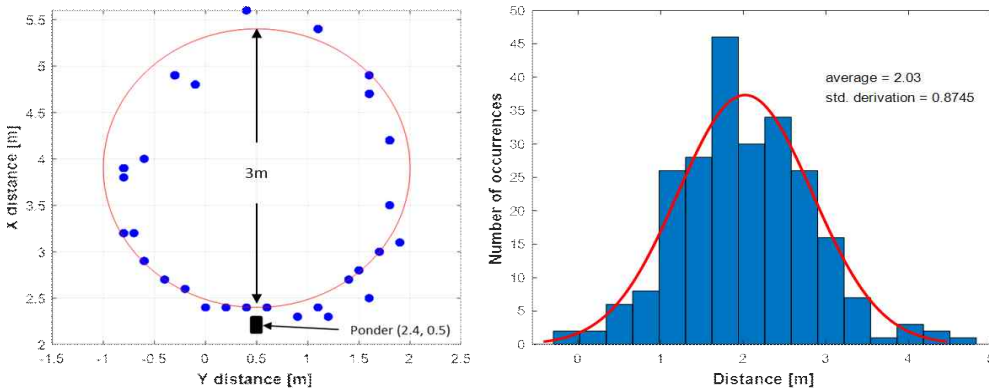

Fig. 6-9 Histogram of distance results from moving test

6.1.3 Depth Sensor

Depth sensor is a device that is mounted on the UUV to measure current depth information based on change in pressure. For the depth sensor used in this study, the voltage value is output. Therefore, it is possible to obtain depth information by measuring voltage value according to the depth of water and making it into the form of the first-order polynomial. The voltage was measured while varying water depth from 0.66 m to 2.46 m. The graph of the voltage value according to water depth using average value is shown in the right graph of Fig. 6-10. The graph on the left shows voltage value obtained at water depth of 0.66 m. As can be seen from the graph, the value obtained from the depth sensor shows a lot of oscillations. Therefore, it is necessary to design and use a low-pass filter. The following equation (6.1) shows the first-order polynomial for the voltage by water depth.

Depth Sensor Test

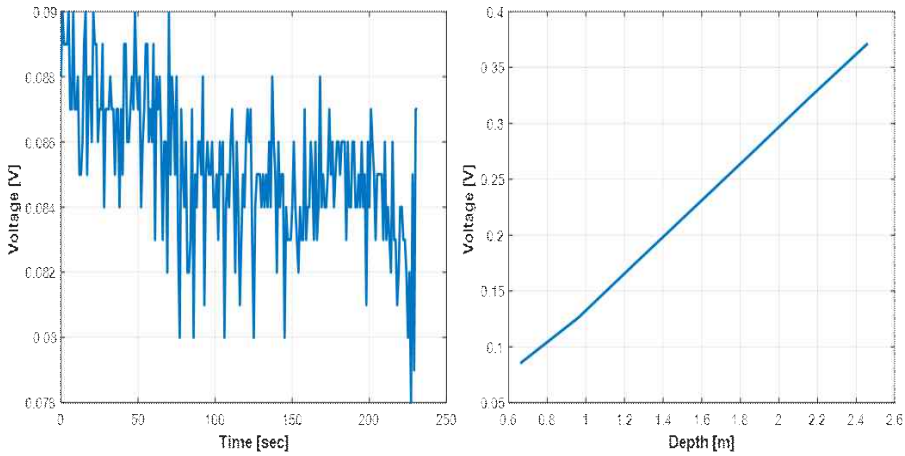

Fig. 6-10 Voltage measured at 0.66m (left)
Voltage value according to depth(right)

6.1.4 Communication Test

Field tests on the combined unmanned ocean vehicle were carried out at the yacht harbor of Korea Maritime and Ocean University. Experiments were conducted to confirm the maximum communication distance in the experimental environment before filed test to confirm the motion and control performance of the platform. Fig. 6-11 below shows the location of the sea area test (field test). It is possible to perform experiment with in the area bounded by the dotted line. At this time, the maximum communication distance was measured to be about 890 m. Results confirmed that the sensor information mounted on the platform could be smoothly transmitted and received.

Fig. 6-11 Site of Field Test

6.2 Field Test

Figure 6-12 shows a real sea area test scene of a combined unmanned ocean vehicle. We conducted a leader-follower control experiment of the platform. Experiments were carried out using a PID controller. Control gain used in the controller was determined by trial and error method.

Experiments were performed to follow the given way-points (50,0), (50, -50), (0, -50), and (0,0). The target speed of the USV was 1.3 m / s and the desired heading angle was obtained from the Pure-pursuit method. Figures 6-13 to 6-19 below show graphs of experimental results. Fig. 6-13 shows X-Y path of a combined unmanned ocean vehicle. The path shown in blue represents the path of the USV from GPS and the black color * represents the location of the

UUV from USBL data. It can be seen that the unmanned offshore platform is moving through a given waypoint and returning to the origin (0,0).

Fig. 6-12 Field Test Scenes

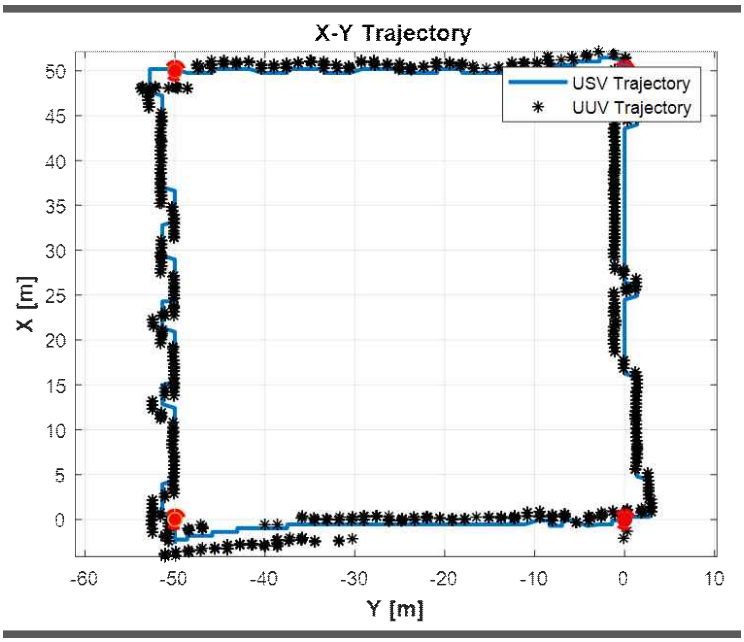

Fig. 6-13 2D Trajectory of the platform

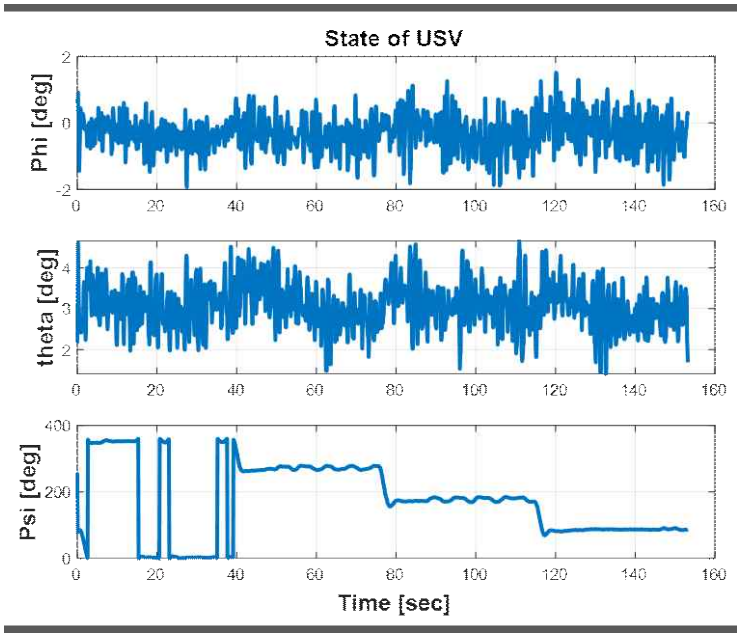

Fig. 6-14 Attitude Values of the USV

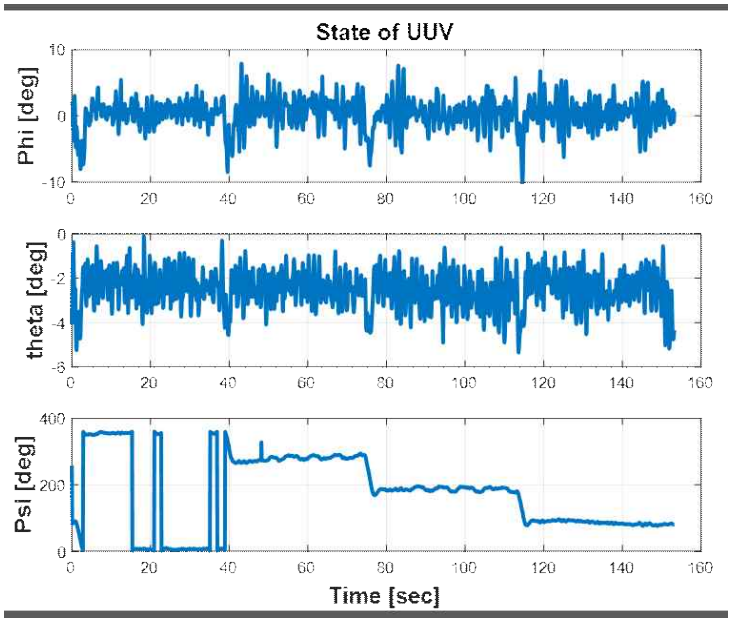

Fig. 6-15 Attitude Values of the UUV

In the case of the roll angle of the UUV, it was confirmed that it changed instantaneously at about 40 seconds, 78 seconds, and 117 seconds in the section where the way-point changed. It was confirmed that it was about 0 degree in the straight motion. The pitch was about -2 ° ~ -4 ° during way-point tracking and the front of the hull moved downward. The heading angle of the UUV was set to follow the heading angle of the USV. Results confirmed that the heading angle of the UUV was well followed by the heading angle of the USV.

Figs. 6-14 and 6-15 show attitude values of the USV and the UUV during way-point tracking. It can be seen that the roll angle of the unattended water line shows a value between about + 2 ° and -2 ° and the pitch has a movement of 2 ° to 3 °. In the case of heading angle, it can be seen that 0 °, 270 °, 180 °, and 90 ° should be followed by the given way-point. These graphs revealed that the USV could follow the target heading angle well.

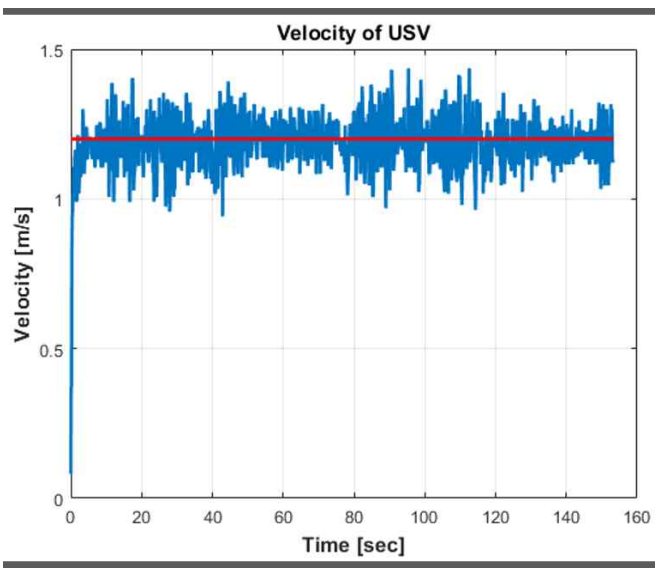

Fig 6-16 Velocity of the USV

Fig. 6-16 shows the speed of the USV, which is moving at a target speed of 1.3m / s, but with average target speed.

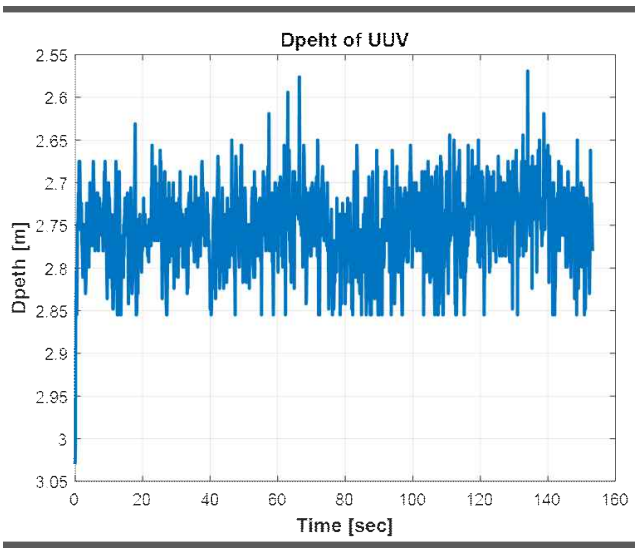

Fig. 6-17 Depth Value of the UUV

Fig. 6-17 shows depth of the UUV. Initially, the UUV was located at a depth of 3 m. It can be seen that the platform moves about 0.25 m at the moment of movement. The UUV moved a depth of about 2.75 m. This might be caused by the speed difference between the USV and the UUV. In the early stage, where the speed difference was large, the movement was the most in the depth direction. It can be seen that way-point tracking is performed well while maintaining water depth.

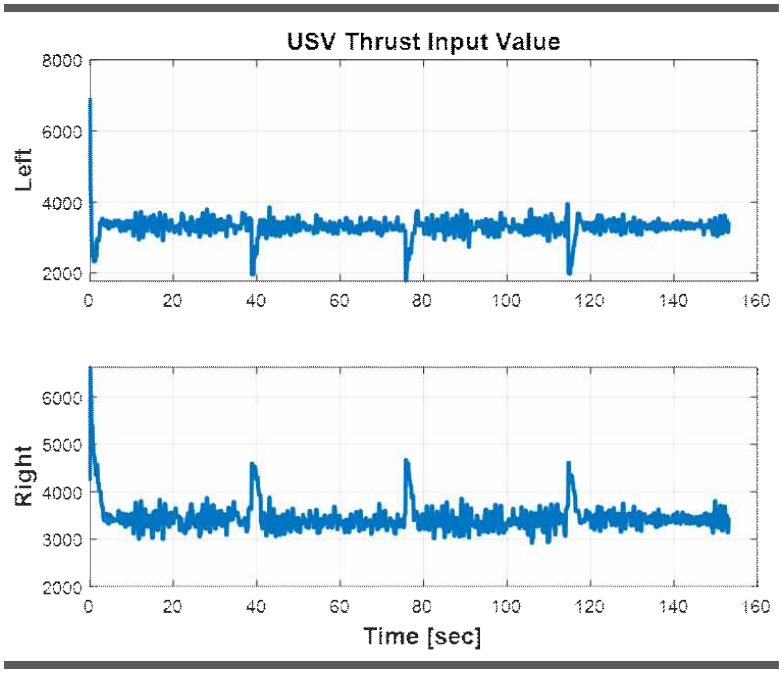

Fig. 6-18 Thrust Input Value of the USV

Figs. 6-18 and 6-19 show input values of the USV and the propeller of the UUV during way-point tracking. The input value represents the value obtained from the controller. It is presented as a digital value. The value input to the actual thruster is an analog value between -5V and 5V. Compared with the X-Y path and the directional graph, the thrust direction showed correct values.

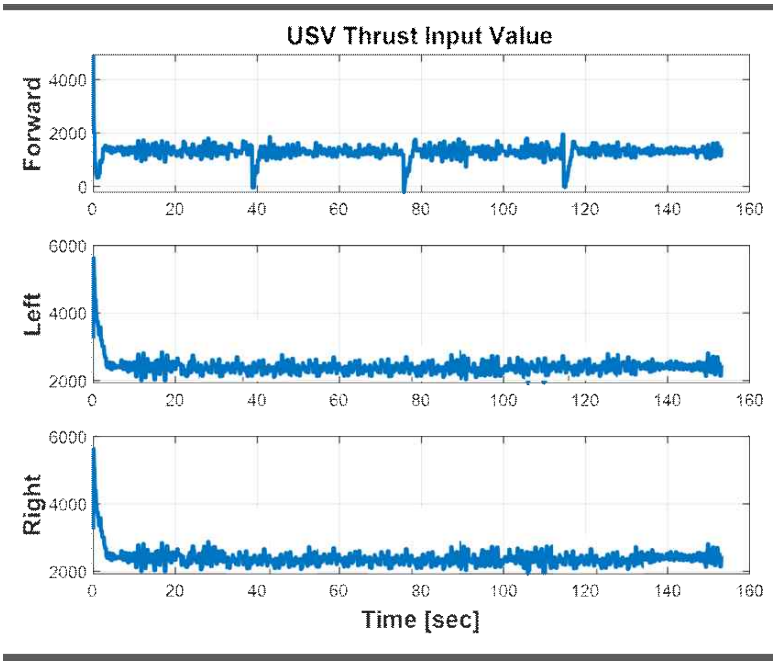

Fig. 6-19 Thrust Input Value of the UUV

7. Conclusion

In this study, an autonomous navigation system for the development and platform operation of USV and UUV combined with underwater cable was studied. The combined unmanned ocean vehicle plays a role in exploring submarine topography by moving a given waypoint. This study also proposes a leader-follower control method. Such unmanned submarines have a geometric path-following method to follow a given waypoint using GPS and a control method to follow unmanned waterline using relative position and relative angle measured in USBL.

Dynamic modeling of the combined unmanned ocean vehicle was performed before performing experiment using the actual system. The effect of the underwater cable on UUV motion was analyzed. Equations of motion of underwater cable were verified through experiments performed in an actual water tank. Simulation of guidance and control law for autonomous navigation was performed using equation of motion of the developed combined unmanned ocean vehicle and validity of the proposed algorithm was verified.

In order to apply the proven guidance and control laws through simulation, we constructed hardware of the USV and UUV and developed a communication and control system between each platform. USV was constructed using commercial rubber boats and torpedoes were developed for UUV.

In the actual system configuration, the reliability of the measured value from the sensor was determined through an individual test on the mounted sensor. Finally, we constructed a system of a combined unmanned ocean vehicle to control way-point tracking. Through experiments, we confirmed the performance of the proposed algorithm.

In this study, it is necessary to change the control hardware to control the depth and pitch of the UUV. It is also necessary to study the algorithm to minimize the influence of underwater cable. Further research is needed on USV to avoid obstacles of UUV and operate a stable platform.

Appendix A

A-1. Transformation Matrix using Euler Angles

■ Linear Velocity Transformation Matrix

$$R_1(\eta_2) = \begin{bmatrix} \cos\theta\cos\psi - \cos\phi\sin\psi + \sin\phi\sin\theta\cos\psi & \sin\phi\sin\psi + \cos\phi\sin\theta\cos\psi \\ \cos\theta\sin\psi \quad \cos\phi\cos\psi + \sin\phi\sin\theta\sin\psi & -\sin\phi\cos\psi + \cos\phi\sin\theta\sin\psi \\ -\sin\theta \quad \sin\phi\cos\phi & \cos\phi\cos\theta \end{bmatrix} \tag{A-1}$$

■ Angular Velocity Transformation Matrix

$$R_2(\eta_2) = \begin{bmatrix} 1 & \sin\phi\tan\theta & \cos\phi\tan\theta \\ 0 & \cos\phi & -\sin\phi \\ 0 & \sin\phi/\cos\theta & \cos\phi/\cos\theta \end{bmatrix} \tag{A-2}$$

A-2. System Matrix Characteristics of Equation of Motion

■ Property 1.

For a rigid-body the inertia matrix is strictly positive if and only if $M_A > 0$, that is :

$$M = M_{RB} + M_A > 0 \tag{A-3}$$

■ Property 2.

For a rigid-body moving through an ideal fluid the Coriolis and centripetal

matrix $C(\nu)$ can always be parameterized such that $C(\nu)$ is skew-symmetrical, that is :

$$C(\nu) = -C^T(\nu) \quad \forall \quad \nu \in \mathbb{R}^6 \tag{A-4}$$

■ Property 3.

For a rigid-body moving through an ideal fluid the hydrodynamic damping matrix will be real, non-symmetrical and strictly positive, that is :

$$D(\nu) > 0 \quad \forall \quad \nu \in \mathbb{R}^6 \tag{A-5}$$

■ Property 4.

As in the body-fixed vector representation it is straight forward to show that

$$\begin{aligned} &(1)\ M_\eta(\eta) = M_\eta^T > 0 \ \forall\ \eta \in \mathbb{R}^6 \\ &(2)\ S^T[\dot{M}_\eta(\eta) - 2C_\eta(\nu,\eta)]S = 0 \ \forall\ s \in \mathbb{R}^6, \nu \in \mathbb{R}^6, \eta \in \mathbb{R}^6 \\ &(3)\ D_\eta(\nu,\eta) > 0 \ \forall\ \nu \in \mathbb{R}^6, \eta \in \mathbb{R}^6 \end{aligned} \tag{A-6}$$

A-3 System Matrix of nonlinear dynamic equation of motion

■ Inertia and Coriolis Matrix w.r.t rigid body

$$\boldsymbol{M}_{RB} = \begin{bmatrix} m\boldsymbol{I}_{3\times 3} & -m\boldsymbol{S}(\boldsymbol{r}_g^b) \\ m\boldsymbol{S}(\boldsymbol{r}_g^b) & \boldsymbol{I}_b \end{bmatrix} = \begin{bmatrix} m & 0 & 0 & 0 & mz_g & -my_g \\ 0 & m & 0 & -mz_g & 0 & mx_g \\ 0 & 0 & m & my_g & -mx_g & 0 \\ 0 & -mz_g & my_g & I_x & -I_{xy} & -I_{xz} \\ mz_g & 0 & -mx_g & -I_{yx} & I_y & -I_{yz} \\ -my_g & mx_g & 0 & -I_{zx} & -I_{zy} & I_z \end{bmatrix} \quad \text{(A-7)}$$

$$\boldsymbol{C}_{RB} = \begin{bmatrix} 0 & 0 & 0 & m(y_g q + z_g r) & -m(x_g q - w) & -m(x_g r + v) \\ 0 & 0 & 0 & -m(y_g p + w) & m(z_g r + x_g p) & -m(y_g r - u) \\ 0 & 0 & 0 & -m(z_g p - v) & -m(z_g q + u) & m(x_g p + y_g q) \\ -m(y_g q + z_g r) & m(y_g p + w) & m(z_g p - v) & 0 & -I_{yz}q - I_{xz}p + I_z r & I_{yz}r + I_{xy}p - I_y q \\ m(x_g q - w) & -m(z_g r + x_g p) & m(z_g q + u) & I_{yz}q + I_{xz}p - I_z r & 0 & -I_{xz}r - I_{xy}q + I_x p \\ m(x_g r + v) & m(y_g r - u) & -m(x_g p + y_g q) & -I_{yz}r - I_{xy}p + I_y q & I_{xz}r + I_{xy}q - I_x p & 0 \end{bmatrix} \quad \text{(A-8)}$$

■ Inertia Matrix (Added mass)

$$M_A = \begin{bmatrix} -X_{\dot{u}} & 0 & 0 & 0 & 0 & 0 \\ 0 & -Y_{\dot{v}} & 0 & 0 & 0 & -Y_{\dot{r}} \\ 0 & 0 & -Z_{\dot{w}} & 0 & -Z_{\dot{q}} & 0 \\ 0 & 0 & 0 & -K_{\dot{p}} & 0 & 0 \\ 0 & 0 & -M_{\dot{w}} & 0 & -M_{\dot{q}} & 0 \\ 0 & -N_{\dot{v}} & 0 & 0 & 0 & -N_{\dot{r}} \end{bmatrix} \quad \text{(A-9)}$$

■ Hydrodynamic Coriolis Matrix (Added mass)

$$C_A(\nu) = \begin{bmatrix} 0 & 0 & 0 & 0 & -Z_{\dot{w}}w & Y_{\dot{v}}v \\ 0 & 0 & 0 & Z_{\dot{w}}w & 0 & -X_{\dot{u}}u \\ 0 & 0 & 0 & -Y_{\dot{v}}v & X_{\dot{u}}u & 0 \\ 0 & -Z_{\dot{w}}w & Y_{\dot{v}}v & 0 & -N_{\dot{r}}r & M_{\dot{q}}q \\ Z_{\dot{w}}w & 0 & -X_{\dot{u}}u & N_{\dot{r}}r & 0 & -K_{\dot{p}}p \\ -Y_{\dot{v}}v & X_{\dot{u}}u & 0 & -M_{\dot{q}}q & K_{\dot{p}}p & 0 \end{bmatrix} \quad \text{(A-10)}$$

■ Hydrodynamic Damping Matrix (linear & non-linear)

$$D_l = \begin{bmatrix} -X_u & 0 & 0 & 0 & 0 & 0 \\ 0 & -Y_v & 0 & 0 & 0 & 0 \\ 0 & 0 & -Z_w & 0 & 0 & 0 \\ 0 & 0 & 0 & -K_p & 0 & 0 \\ 0 & 0 & 0 & 0 & -M_q & 0 \\ 0 & 0 & 0 & 0 & 0 & -N_r \end{bmatrix} \quad \text{(A-11)}$$

$$D_{nl} = \begin{bmatrix} -X_{u|u|}|u| & 0 & 0 & 0 & 0 & 0 \\ 0 & -Y_{v|v|}|v| & 0 & 0 & 0 & 0 \\ 0 & 0 & -Z_{w|w|}|w| & 0 & 0 & 0 \\ 0 & 0 & 0 & -K_{p|p|}|p| & 0 & 0 \\ 0 & 0 & 0 & 0 & -M_{q|q|}|q| & 0 \\ 0 & 0 & 0 & 0 & 0 & -N_{r|r|}|r| \end{bmatrix} \quad \text{(A-12)}$$

■ Restoring forces and moments

$$\boldsymbol{g}(\boldsymbol{\eta}) = \begin{bmatrix} (W-B)\sin\theta \\ -(W-B)\cos\theta\sin\phi \\ -(W-B)\cos\theta\cos\phi \\ -(y_g W - y_b B)\cos\theta\cos\phi + (z_g W - z_b B)\cos\theta\sin\phi \\ (z_g W - z_b B)\sin\theta + (x_g W - x_b B)\cos\theta\cos\phi \\ -(x_g W - x_b B)\cos\theta\sin\phi - (y_g W - y_b B)\sin\theta \end{bmatrix} \quad \text{(A-13)}$$

Appendix B

■ GPS : Hemisphere – Vector H200

Table C-1 Specification of the GPS

Parameter	Value		
Communications	NMEA 0183, UART		
Positioning Accuracy		Horizontal	Vertical
	SBAS	0.3m	0.6m
	DGPS	0.3m	0.6m
	RTK	10mm+1ppm	20mm+2ppm
Heading Accuracy	0.15° rms @ 1.0m antenna separation		
Input Voltage	3.3 VDC		
Power Consumption	< 2.1W nomial GPS		

■ AHRS : XSENS – MTi 30

Table C-2 Specification of the AHRS

Parameter	Value	
Orientation	Roll / Pitch	0.5° ~ 2.0° (Dynamic)
	Yaw	1.0°
Gyroscope specification	Initial bias error	0.2 deg/s
	g-sensitivity	0.006 deg/s
Accelerometer	Initial bias error	0.05 m/s^2
Magnetometer	Total RMS noise	0.5 mGauss
Power consumption	550 mW @ 5.1V	
Operating voltage	4.5 ~ 34V	

■ USBL : SeaTrac – X150(USBL Beacon), X010(Transponder)

Table C-3 Specification of the USBL

Parameter	Value
Acoustic Range	1km radius horizontal, 1km vertical
Velocity-of-Sound Range	1300ms-1 to 1700ms-1
Power Consumption	Less than 10W
Supply Voltage	9V to 28V DC
Range Resolution	±50mm
Angular Resolution	±1°

■ Depth Sensor : Sensys – PSC

Table C-4 Specification of the Depth Sensor

Parameter	Value
Range	0 ~ 10bar
Accuracy	± 0.25%FS(RSS)
Output	0~5VDC
Supply Voltage	11~28VDC
Compensated Temperature Range	-10 ~ 70°C

■ Multibeam Sonar : Blueprint Subsea – M750d

Table C-5 Specification of the Multibeam Sonar

Parameter	Value
Communications	4-wire 100-baseT Ethernet
Supply Voltage	18V to 32V
Power Consumption	10W to 35W
Range	120m (750kHz) / 40m (1.2MHz)
Range Resolution	4mm (750kHz) / 2.5mm (1.2MHz)
Update Rate	40Hz

■ Micro Controller Unit : Cypress – CY8C58LP

Table C-6 Specification of the MCU

Parameter	Value
Performance	32-bit Arm Cortex-M3 CPU
	24-channel direct memory access controller
	24-bi 64-tap fixed-point digital filter processor
Memories	Up to 256KB program flash
	Up to 32 KB additional flash
	Up to 64 KB RAM
Operating Voltage	1.71 to 5.5 VDC

■ Communication Antenna : GT-Wave – GT-WAVE860/N2

Table C-7 Specification of the Antenna

Parameter	Value
Speed	Max 867Mbps / real Throughput : 360Mbps
Modulation	DSSS, TDMA, OFDM, QPSK
Bandwidth	20/40/80 MHz
Supply Power	PoE 48 VDC
Wireless Access	IEEE802.11 2.4~2.485GHz(802.11ng)

■ Thruster of the USV : MINN KOTA – RT-80/EM

Table C-8 Specification of the Thruster

Parameter	Value
Supply Power	24 VDC
Power Consumption	58A
Max. Thrust Force	36.2kgf

■ Thruster of the UUV : Technadyne – Model300

Table C-9 Specification of the Thruster

Parameter	Value
Supply Power	24 VDC
Power Consumption	20A
Max. Thrust Force	7.7kgf (forward) / 3.2kgf (reverse)

■ Stepping Motor : Autonics – A63K-G5913

Table C-10 Specification of the Motor

Parameter	Value
Supply Power	24 VDC
Power Consumption	2.8A/Phase
Max. Torque	6.3Nm
Step Angle	0.72° / 0.36°
Rotor Inertia	4000 $g \cdot cm^2$

■ Tether Interface Boards : BlueRobotics – Fathom-X

Table C-11 Specification of the Tether Interface Boards

Parameter	Value
Supply Power	7 ~ 28 VDC
Max. Practical Bandwidth	80 Mbps
Max. Tether Length	300m
Operating Temperature	-20 to 85°C

REFERENCES

[1] Ha, J.H., Ko, H.K, Cho, H.S., Chung, W.K., Ahn, D. and Shin, S.R., 2013,“A proposal of marine geophysical exploration techniques for offshore plant installation”,J of the Korean Society of Marine Engineering, Vol. 37, No. 2, pp.242-251

[2] Marsset, T., et al. "High and very high resolution deep-towed seismic system: Performance and examples from deep water Geohazard studies." Deep Sea Research Part I: Oceanographic Research Papers 57.4 (2010): 628-637.

[3] Gerstmayr, Johannes, Hiroyuki Sugiyama, and Aki Mikkola. "Review on the absolute nodal coordinate formulation for large deformation analysis of multibody systems." Journal of Computational and Nonlinear Dynamics 8.3 (2013): 031016.

[4] Grosenbaugh, Mark A. "Transient behavior of towed cable systems during ship turning maneuvers." Ocean engineering 34.11-12 (2007): 1532-1542.

[5] T. I. Fossen, “Guidance and Control of Ocean Vehicles”, John Wiley & Sons, England, 1994.

[6] Muske, Kenneth R., et al. "Identification of a control oriented nonlinear dynamic USV model." 2008 American Control Conference. IEEE, 2008.

[7] Sonnenburg, Christian R., and Craig A. Woolsey. "Modeling, identification, and control of an unmanned surface vehicle." Journal of Field Robotics 30.3 (2013): 371-398.

[8] Reyhanoglu, Mahmut. "Control and stabilization of an underactuated surface vessel." Proceedings of 35th IEEE Conference on Decision and Control. Vol. 3. IEEE, 1996.

[9] Morton Gertler and Grant R. Hagen, 1967, Standard Equation of Motion for Submarine Simulation, Naval Ship Research and Development Center, Report No. 2510

[10] G. Roberts and R. Sutton, “Advances in Unmanned Marine Vehicles”, IET, 2006.

[11] Prestero, Timothy Timothy Jason. Verification of a six-degree of freedom simulation model for the REMUS autonomous underwater vehicle. Diss. Massachusetts institute of technology, 2001.

[12] B. Buckham, M. Nahon, M. Seto, X. Zhao, and C. Lambert, “Dynamics and control of a towed underwater vehicle system , part I : model development,” vol. 30, pp. 453–470, 2003.

[13] B. Buckham, F. R. Driscoll, and M. Nahon, “Development of a Finite Element Cable Model for Use in Low-Tension Dynamics,” vol. 71, pp. 476–485, 2004.

[14] Huang, S. (1994). “Dynamics analysis of three–dimensional marine cables.” J. Waterway, Port, Coastal, and Ocean Engineering, 21(6).

[15] Gobat, J., Grosenbaugh, M.: Time-domain numerical simulation of ocean cable structures. Ocean Eng. 33(10), 1373–1400(2006)

[16] Y. Choo and M. J. Casarella, “A Survey of Analytical Methods for Dynamic Simulation of Cable-Body Systems.,” J. Hydronautics, vol. 7, no. 4, pp. 137–144, 1973.

[17] Kamman, J. and Huston, R. (1999). “Modeling of variable length towed and tethered cable systems.” J. Guidance, Control, and Dynamics, 22(4).

[18] Masciola, Marco, Jason Jonkman, and Amy Robertson. "Extending the capabilities of the mooring analysis program: A survey of dynamic mooring line theories for integration into FAST." ASME 2014 33rd International

Conference on Ocean, Offshore and Arctic Engineering. American Society of Mechanical Engineers, 2014.

[19] Masciola, Marco D., Meyer Nahon, and Frederick R. Driscoll. "Static analysis of the lumped mass cable model using a shooting algorithm." Journal of Waterway, Port, Coastal, and Ocean Engineering 138.2 (2011): 164-171.

[20] Eidsvik, Ole Alexander Nørve, and Ingrid Schjølberg. "Finite element cable-model for Remotely Operated Vehicles (ROVs) by application of beam theory." Ocean Engineering 163 (2018): 322-336.

[21] Driscoll, F. R., R. G. Lueck, and M. Nahon. "Development and validation of a lumped-mass dynamics model of a deep-sea ROV system." Applied Ocean Research 22.3 (2000): 169-182.

[22] Buckham, Bradley Jason. Dynamics modelling of low-tension tethers for submerged remotely operated vehicles. Diss. 2003.

[23] Merchant, H. C. and Kelf, M. A., “Non-Linear Analysis of Submerged Ocean Buoy Systems,” Proceedings of MTS/IEEE OCEANS ’73, Vol. 1, 1973, pp. 390-395.

[24] Kelf, M. A. and Merchant, H. C., “Analysis of a Multiple Buoy InstrumentPlatform; A Non-Linear Model,” Proceedings of MTS/IEEE OCEANS ’74 , Vol. 1, 1974, pp. 44-48.

[25] Thomson, W. T. and Dahleh, M. D., Theory of Vibrations with Applications, Prentice Hall: Upper Saddle River, NJ, 1998, pp. 16-89.

[26] Wang, ZhiDong, Eiji Nakano, and Takayuki Takahashi. "Solving function distribution and behavior design problem for cooperative object handling by multiple mobile robots." IEEE Transactions on Systems, Man, and Cybernetics-Part A: Systems and Humans 33.5 (2003): 537-549.

[27] Takahashi, Hiromasa, Hiroaki Nishi, and Kouhei Ohnishi. "Autonomous

decentralized control for formation of multiple mobile robots considering ability of robot." IEEE Transactions on Industrial Electronics 51.6 (2004): 1272-1279.

[28] Lewis, M. Anthony, and Kar-Han Tan. "High precision formation control of mobile robots using virtual structures." Autonomous robots 4.4 (1997): 387-403.

[29] Das, Aveek K., et al. "A vision-based formation control framework." IEEE transactions on robotics and automation 18.5 (2002): 813-825.

[30] Edwards, D. B., et al. "A leader-follower algorithm for multiple AUV formations." 2004 IEEE/OES Autonomous Underwater Vehicles (IEEE Cat. No. 04CH37578). IEEE, 2004.

[31] Liang, Xinwu, et al. "Leader-following formation tracking control of mobile robots without direct position measurements." IEEE Transactions on Automatic Control 61.12 (2016): 4131-4137.

[32] Borhaug, Even, Alexey Pavlov, and Kristin Y. Pettersen. "Integral LOS control for path following of underactuated marine surface vessels in the presence of constant ocean currents." 2008 47th IEEE Conference on Decision and Control. IEEE, 2008.

[33] Yoon, S., et al. "A Simulation Study for Performance Analysis of Path Tracking Method of Follow the Carrot and Pure Pursuit." The Korean Association of Ocean Science and Technology Societies 2012 Joint Conference. 2012.

[34] Kim, Dong-Hyung, Chang-Jun Kim, and Chang-Soo Han. "Geometric path tracking and obstacle avoidance methods for an autonomous navigation of nonholonomic mobile robot." Journal of Institute of Control, Robotics and Systems 16.8 (2010): 771-779.

[35] Zheng, Alex, Mayuresh V. Kothare, and Manfred Morari. "Anti-windup design for internal model control." International Journal of Control 60.5 (1994): 1015-1024.

[36] Kim, Minsung, et al. "Variable-structure PID controller with anti-windup for autonomous underwater vehicle." 2013 OCEANS-San Diego. IEEE, 2013.

[37] Choi, Youngjin, and Wan Kyun Chung. PID trajectory tracking control for mechanical systems. Vol. 298. Springer Science & Business Media, 2004.

[38] Polycarpou, Marios M., and Petros A. Ioannou. "A robust adaptive nonlinear control design." 1993 American Control Conference. IEEE, 1993.

[39] Zhang, Xian-Ku, et al. "Linear reduction of backstepping algorithm based on nonlinear decoration for ship course-keeping control system." Ocean Engineering 147 (2018): 1-8.

[40] Liao, Yonglong, and Fucheng Liao. "Design of a backstepping tracking controller for a class of linear systems with actuator delay." Mathematical Problems in Engineering 2015 (2015).

[41] H.K.Khalil, Nonlinear System(Prentice Hall, New York, 2002)

[42] M. Krstic, I. Kanellakopoulos, P.V. Kokotovic, Nonlinear and Adaptive Control Design(Wiley-Interscience, New York, 1995)

Acknowledgement

‘Chase down your passion like it’s the last bus of the night’

‘You have to have confidence in your ability,

and then be tough enough to follow through’

대학 3학년에 시작된 무인해양로봇에 대한 궁금증과 무지함으로부터 벗어나기 위해 달려 온지 8년이 지났습니다. 여전히 부족함을 느끼고 더욱더 최선을 다하지 못했음을 후회하기도 합니다. 이 페이지를 끝으로 학생으로서 마지막 논문을 마무리 하려고하니 수많은 추억들과 포기하지 않도록 옆에서 도와준 많은 사람들이 머릿속을 지나칩니다. 부족하지만 이 짧은 글을 통해 조금이나마 감사의 말을 전하려고 합니다.

우선 대학교 생활에 가장 큰 변화를 주신 지도교수님이신 김준영 교수님께 감사의 말을 전합니다. 그리고 지도교수님처럼 항상 도와주시고 많은 가르침을 주신 서주노 교수님, 최형식 교수님, 조용성 교수님, 이성욱 교수님께 감사의 인사 전하고 싶습니다. 그리고 제가 필요할 때마다 흔쾌히 실험을 할 수 있도록 지원해주신 생산기술연구소 해양로봇 센터 연구원님들께도 감사한 마음을 전합니다.

8년이라는 생활을 한 선박의장설계 실험실....동희형, 승우형, 춘우형, 성협형 부족한 동생을 이끌어 준다고 고생 많으셨습니다. 항상 응원해주셔서 감사합니다. 그리고 건석, 흔택, 동호, 영진, 현석, 성구, 지학, 승규 잘 도와 줘서 고맙고 좋은 추억 만들어 줘서 감사합니다. 실험실 식구와 마찬가지로 지능로봇 실험실 상기형, 대형, 현준, 서강, 지형, 한솔, 명준 혼자 있는 나를 항상 외롭

지 않게 잘 챙겨줘서 고맙고 창고에서 지낸 수많은 밤을 항상 기억할게. 끝으로 학위를 받기까지 항상 믿어주시고 응원해주신 그리고 기다려준 우리 가족들 너무 감사하고 사랑합니다.

글로 다 표현하지 못할 만큼 너무나 많은 사람들에게 도움을 받았습니다. 미처 언급하지 못한 분들께 죄송하다는 말씀드립니다.

이제 사회에 나가 새로운 도전을 하고자 합니다. 항상 즐겁고 재미있는 일을 하자는 초심을 잃지 않고, 앞서 언급한 많은 분들에게 감사한 마음을 간직하고 남들에게 베풀며 살겠습니다.